An X-Ray Study of the Pulsar Wind Nebulae Discovered in the Very High Energy Gamma-Ray Band

Takayasu Anada

Department of Physics, School of Science, University of Tokyo
&
The Institute of Space and Astronautical Science

December 17, 2008

Abstract

Recent development of the very-high-energy (VHE) γ-ray telescopes has opened the last electro-magnetic window to observe the universe. The VHE γ-ray observations have been long waited in the expectation that they may reveal the acceleration sites and mechanism of cosmic rays, whose origin is still unknown since the discovery in 1912. The Galactic plane survey by the H.E.S.S. Cherenkov telescopes revealed the presence of about 40 VHE γ-ray sources in the TeV band (10^{12-13} eV). Surprisingly, most of them have no known counterpart in other wavelengths. However, pulsar wind nebulae (PWNe) are often found in their neighborhood, and are suspected to be associated.

We made systematic analysis of the X-ray data of all of the known 16 PWNe whose association to the VHE γ-ray source is suspected, and studied the nature and evolution of the PWNe. In this study, archive data from various X-ray satellites were used, but detailed analysis was made with the newly obtained Suzaku data for two of them, HESS J1837–069 and HESS J1809–193. We studied the statistical nature of them, in comparison with the PWNe no association is known. It is focused on the physical parameters characterizing the PWNe, i.e. spin-down luminosity of the pulsar and the spectral slope in the X-ray band (2–10 keV). No statistically significant difference is found between the two groups, i.e. the PWNe associated and not associated with the VHE γ-ray sources. We also compared the correlation between the characteristic age of the pulsar and the X-ray luminosity, which are known to be well correlated in the PWNe. No statistically significant difference is again found between the two groups. In addition, we also studied the spatial offset between the center of the VHE γ-ray emission and the pulsar. The offset can be explained by the kick velocity of the pulsar at its birth. Although there are differences by a factor of two or three, the estimated kick velocities were consistent with those measured in the radio band. All these results indicate that the PWNe detected in VHE γ-ray band have no significant differences in their current properties with those not detected.

In order to study the nature of the PWNe and their evolution, we paid attention to the spatial extent of the X-ray and VHE γ-ray emission regions. The size of the γ-ray emission region becomes larger with the characteristic age of the pulsar. This is consistent with the diffusion of the relic electrons, whose energy loss is small compared to the age of the PWNe. On the other hand, no systematic studies were done so far for the X-ray emission region. We made systematic analysis of the X-ray data, and discovered for the first time that the size of the non-thermal X-ray emission region also keeps increasing with the age of the PWNe up to 100 kyrs. Because the synchrotron energy loss timescale of electrons is significantly shorter than the age of

the PWNe, this means the presence of some mechanisms that makes electrons much easier to extend when the PWNe become old. We examined the implication of this finding and considered two possibilities, i.e. time evolution of the magnetic turbulence in the termination shock and that of the advection speed after the shock. This is the first observational result to show the spatial evolutions of the PWNe.

Contents

List of Figures

List of Tables

Chapter 1

Introduction

Cosmic rays are high energy particles originating from space. Since the discovery of the cosmic rays with the balloon experiments by Hess (1912), their origin and the acceleration mechanism have been one of the main targets of the space physics. The most plausible candidate of the cosmic ray accelerators in our Galaxy is the supernova remnants (SNRs). It is suspected that the cosmic rays below the knee energy ($\sim 10^{15.5}$ eV), may be explained by the particle acceleration in the strong shocks of the SNR. However, this is still unclear especially from the observational point of view. In order to investigate the acceleration sites of the cosmic rays, it is effective to use the very-high-energy (VHE) γ-ray band (> 100 GeV). Protons accelerated to the relativistic energies produce neutral pions through the collisions with the interstellar matter, which decay to γ-rays spontaneously. On the other hand, relativistic electrons generate γ-rays via the inverse Compton scattering of cosmic microwave background. From these reasons, observations in the VHE γ-ray band are long-waited, and have rapidly developed recently.

Since 2004, H.E.S.S. Cherenkov telescopes in Namibia have performed a Galactic plane survey in the VHE γ-ray band (Aharonian et al., 2005a, 2006a). As a result, about 40 γ-ray sources were found along the Galactic plane. Surprisingly, most of them have no known counterpart in other wave bands, thus called unidentified VHE sources, and vigorous search has been performed especially in the X-ray band. It soon became clear that pulsars or pulsar wind nebulae (PWNe) are preferentially located in the vicinity of the VHE γ-ray sources and possible association is suspected. Therefore, PWNe gathered wide attention from all over the world as candidate particle accelerators. If the VHE γ-ray emission results from the inverse Compton scattering of the cosmic microwave background by the accelerated electrons, they should also radiate synchrotron emission from radio through hard X-ray bands under the appropriate strength of magnetic field. This means that X-rays are suited to study the unidentified VHE γ-ray sources. In fact, a lot of follow-up observations were made using various X-ray satellites such as Suzaku, Chandra and XMM-Newton.

A PWN is powered by the rotational energy of the pulsar, a rapidly spinning, highly magnetized neutron star. It is a very young system, typically less than 10^5 yr, similar to the SNR produced by the same supernova explosion. A pulsar is a very simple system, just a rapidly rotating, magnetized star in a vacuum, but its nature is poorly understood yet. A rapid rotation of a neutron star in the strong magnetic field produces large electric field to accelerate electrons to relativistic speed. The accelerated electrons produce curvature radiation, which create electron/positron pairs. The pairs again produce curvature radiation; thus the numbers of pairs increase rapidly. Finally the pair plasma flow out from the magnetosphere of the neutron star at the relativistic speed. The flow is called as the pulsar wind. The pulsar wind will collide with the ambient matter to produce the termination shock. Because the shock appears as a nebula, it is called as a PWN. The energetic electrons (positrons) responsible for the VHE γ-ray emission may be produced in the termination shock. The past observations of the PWNe were basically made to observe the synchrotron emission from the energetic electrons. Thus it was difficult to estimate the electron energy and the magnetic field separately; only the coupled parameter can be estimated. However, if we observe the Compton up-scattered emission in the VHE γ-ray band, we can directly measure the electron energy. This in principle make it possible to disentangle the coupling between the electron energy and the magnetic field. Thus systematic studies of the PWNe detected in the VHE γ-ray band may be effective in revealing the acceleration mechanism of the relativistic particles. However, current studies of the PWNe are mostly concentrated to the individual sources, and no systematic analysis were made so far.

In this thesis, we make systematic analysis of the PWNe possibly associated with the unidentified VHE γ-ray sources in the X-ray band. In Chapter 2, we review the properties of the PWNe and the related phenomena in the universe with the underlying physics. We describe X-ray instruments used in this thesis in Chapter 3. Because we used Suzaku to obtain new X-ray data for two PWNe, description is most detailed for the instruments on board Suzaku. The analyses and results of the X-ray observations of the PWNe are summarized in Chapter 4. Implication of the analysis results are discussed in Chapter 5. Chapter 6 lists up the conclusions of the current studies.

Chapter 2

Review

In this chapter, we summarize the properties of the pulsar wind nebulae, and the related phenomena in the universe together with the underlying physics. Very high energy γ-ray observations, which were developed only recently, have revealed the presence of unique sources in this last electromagnetic window. Pulsar wind nebulae may be the main constituent of these high energy sources. Because the VHE γ-radiation is closely related to the cosmic rays, we start our review with the brief description of them in §2.1. One of the long-standing problems regarding the cosmic rays is how and where they are accelerated. We explain the basic mechanisms of particle acceleration in §2.2, which is followed by the description of the particle propagation in §2.3. Possible acceleration sites of cosmic rays in Galaxy are reviewed in §2.4. After these preliminaries, we describe the recent progress of the TeV γ-ray observations, and the main constituent of the TeV γ-ray sources, i.e. the PWNe in §2.5. Nature of the PWNe is reviewed in §2.6, and their emission mechanisms in §2.7.

2.1 Cosmic Rays

Cosmic rays are high energy radiation in space. While the most abundant constituent are protons, which account for $\sim 90\%$ of the cosmic rays, $\sim 9\%$ are atomic nuclei, which have been found in the entire range of the periodic system. In addition, electrons have been found to occupy about 1% of protons at the same energy. Since the discovery of the cosmic rays with balloon experiments (Hess, 1912), the origin and the acceleration mechanism have been one of the biggest problems in the space physics.

Energy spectrum of cosmic rays (dN/dE, N: number flux, E: energy of cosmic ray) were measured from 0.1 GeV up to 10^{20} eV as shown in figure 2.1. The total energy spectrum (including all the elements) can be roughly represented as a power law, i.e. $dN/dE \propto E^{-\alpha}$, but the slope ($\alpha$) changes around $10^{15.5}$ eV, which is called a "knee" energy. The slope is $\alpha \sim 2.7$ below the knee, while it increases to $\alpha \sim 3.3$ above the knee. Assuming the average interstellar magnetic field of ~ 1 μG, the gyro-radius

of the particle with the knee energy becomes 3 pc. This means that the gyro-radius is much smaller the thickness of the Galactic disk ($\sim$1 kpc), and the cosmic rays are effectively confined in Galaxy by frequently changing their propagation direction. Steepening the slope above the knee may be due to the rapid escape of the cosmic rays from Galaxy. Intensity of the cosmic ray protons at 10 GeV is approximately 20 m^{-2} sr^{-1} GeV^{-1} s^{-1}. Using the above energy spectrum, total flux of cosmic rays integrated above 10 GeV and solid angle gives $\sim$0.01 m^{-2} s^{-1}. The flux below 10 GeV is modulated by the solar activity and is shielded by the geomagnetic field.

Detailed studies of the cosmic ray elements provide an important clue on the origin and propagation of the cosmic rays. Light elements, such as Li, Be, B, have very small cosmic abundance, while they are known to be frequently observed in cosmic rays. This difference is interpreted as the results of spallation during the propagation of interstellar space. Heavier elements such as C, N, O are considered to collide with the interstellar matter to produce Li, Be, B. Therefore, the fraction of Li, Be, B in the cosmic rays is related to the effective thickness of matter through which the cosmic rays traveled before reaching the earth. Current observations indicate the effective thickness of 6–8 g cm^{-2}. If we assume a mean number density of $\sim$1 cm^{-3} for interstellar matter, this corresponds to the distance of 10^6 pc, and to the travel time of a few millions year. Note that the above distance is the integrated one along the trajectory of the cosmic rays. The mean life time of the cosmic rays can also be estimated from the fraction of unstable elements, such as ^{10}Be, ^{26}Al, ^{36}Cl, etc. Recent observations indicate a mean life of 10^7 yr. Here, the life time actually means the confinement time of the cosmic rays in Galaxy. Cosmic rays generated in somewhere in Galaxy are considered to diffuse gradually in galaxy, and finally to escape from Galaxy in 10^7 yr. Cosmic rays travel through 6–8 g cm^{-2} of matter before escaping from Galaxy.

2.2 Particle Acceleration in Shock Fronts

The acceleration mechanism of cosmic rays is still unclear. Here, we explain the most successful acceleration mechanism, first-order Fermi acceleration according to Bell (1978).

Let us suppose that a strong shock propagates at a supersonic velocity v_1, and a particle energy is constant in the shock frame while the particle is in the upstream or downstream regions. A schematic view of the shock front is shown in figure 2.2. In the rest frame of the shock, u_u is the velocity of the upstream, while u_d is the velocity of the downstream, which is referred to as an advection velocity. A relativistic particle with energy of E_k which experienced k cycles, passing the shock from upstream to

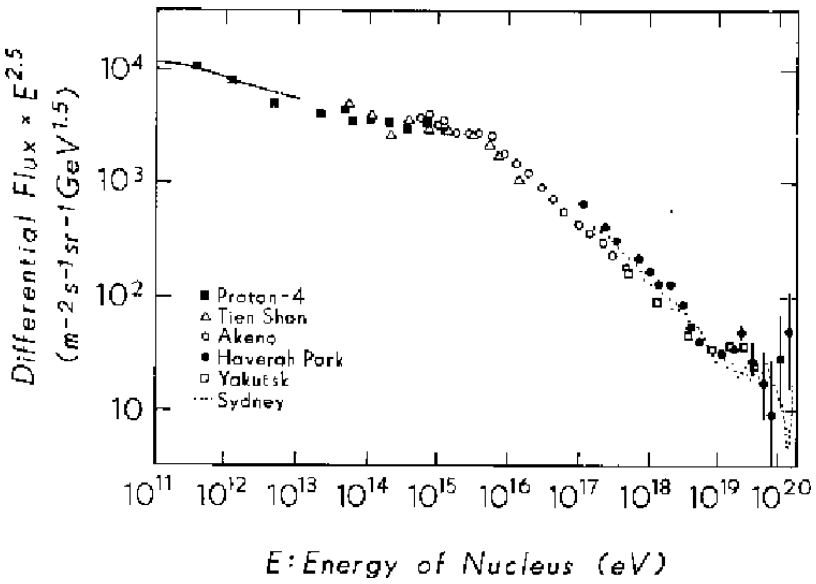

Figure 2.1: Energy spectrum of cosmic protons (Sokolsky, 1989). In order to make it clear the structure of the spectrum at the knee energy, the vertical axis is written in differential flux times $E^{2.5}$.

downstream and back to upstream, has its energy increased to

$$E_{k+1} = E_k \left(\frac{1 + v_{ku}(u_u - u_d)\cos\theta_{ku}/c^2}{1 + v_{kd}(u_u - u_d)\cos\theta_{kd}/c^2} \right), \tag{2.1}$$

where v_{ku} is the velocity at which the particle crosses from upstream to downstream with an angle θ_{ku} with respect to the normal direction of the shock front, and v_{kd} and θ_{kd} are the respective quantities for the return crossing. Assuming that the scattering is isotropic and $(u_u - u_d) \ll c$, the particle energy after n cycles of scattering with respect to the energy when the particle injected into the system, E_0, is

$$\begin{aligned} \ln\left(\frac{E_n}{E_0}\right) &= n\left[\left\langle \ln\left(1 + \frac{u_u - u_d}{c}\cos\theta_{ku}\right)\right\rangle - \left\langle \ln\left(1 + \frac{u_u - u_d}{c}\cos\theta_{kd}\right)\right\rangle\right] \\ &\simeq \frac{4}{3}n\frac{u_u - u_d}{c}\left(1 + O\left(\frac{u_u - u_d}{c}\right)\right). \end{aligned} \tag{2.2}$$

Here E_0 is assumed to be much greater than its rest mass energy, that is, $v_{ku} \sim v_{kd} \sim c$.

Bell (1978) calculated the probability that a scattered particle escapes from the acceleration region for each round-trip as

$$\eta_s = 4\frac{u_d}{v_p}, \tag{2.3}$$

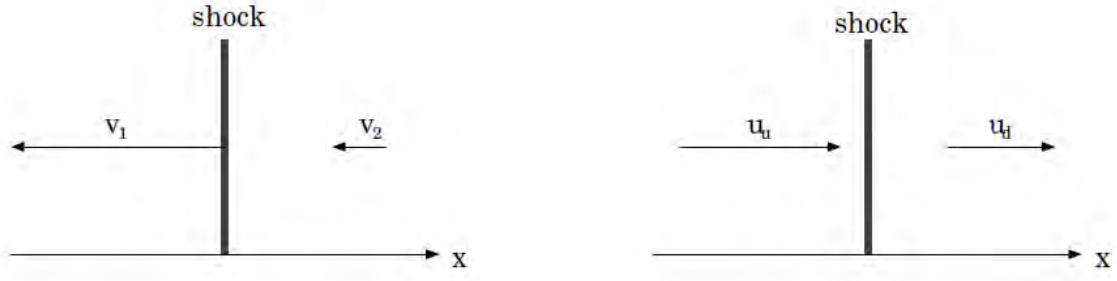

Figure 2.2: A schematic view of the shock front in laboratory frame (left) and the rest frame of the shock (right). v_1 is the shock velocity relative to the unshocked material, and v_2 is that of shocked material.

where v_p is a particle velocity. The probability of a particle completing at least n round-trips is

$$\begin{aligned} \ln P_n &= n \ln(1-\eta_s) = n \ln(1-4\beta_d) \\ &= -\left(\frac{3u_d}{u_u - u_d} + O\left(\frac{u_u - u_d}{c}\right)\right) \ln\left(\frac{E_n}{E_0}\right). \end{aligned} \tag{2.4}$$

Here we assumed the particle is relativistic ($v_p \sim c$).

Using Eq.(2.4), the differential energy spectrum is derived as

$$N(E)dE \propto E^{-\frac{u_u+2u_d}{u_u-u_d}}. \tag{2.5}$$

From the conservations of the mass, energy, and momentum, we can obtain the relation of $u_d = u_u/4$ for ideal gas of monoatomic molecules in the strong shock wave. Eq.(2.5) is then

$$N(E) \propto E^{-2}. \tag{2.6}$$

Thus the resulting energy spectrum undergoing first-order Fermi acceleration turns out to be a power-law with the slope of $\alpha = 2$.

2.3 Particle Propagation

When particles escape the acceleration sites, they propagate in Galaxy by diffusion. In this subsection, we describe how they propagate. As the scattering is assumed to be resonant scattering from magnetic-field fluctuations, the mean free path λ can be written in terms of the particle gyroradius r_g as $\lambda \equiv \xi r_g = \xi(E/eB)$, where the second expression is valid for the extreme-relativistic particles. The factor ξ is known as the gyrofactor; it is considered that the smallest physically reasonable mean free path is

$\lambda = r_g$ (Bohm limit), thus $\xi \geq 1$. If the diffusion is treated as a small perturbation to unperturbed gyromotion trajectories, ξ can be expressed as (Blandford & Eichler, 1987)

$$\xi \sim \left(\frac{B}{\delta B}\right)^2. \tag{2.7}$$

The diffusion timescale $\tau_{\rm dif}$ is given from the random-walk theory as

$$\tau_{\rm dif} = \frac{r_{\rm dif}^2}{K}, \tag{2.8}$$

where $r_{\rm dif}$ is the scale length of the spatial distribution of the relativistic electrons and K is the diffusion coefficient. The scale length of the spatial distribution is then $r_{\rm dif} = \sqrt{K\tau_{\rm dif}}$, that is, the relativistic electrons propagate in proprotion to the square root of the diffusion timescale. In case the scattering occurs along the direction of the magnetic field, the diffusion coefficient $K_\parallel$ can be written as

$$K_\parallel = \frac{1}{3}\xi r_g c = \frac{1}{3}\xi\frac{E_e c}{eB}. \tag{2.9}$$

The ratio of the diffusion coefficient perpendicular to the magnetic field $K_\perp$ to $K_\parallel$ is given by (Jokipii, 1987)

$$\frac{K_\perp}{K_\parallel} = \frac{1}{1+(\lambda_\parallel/r_g)^2} = \frac{1}{1+\xi^2}. \tag{2.10}$$

The diffusion coefficient K for general direction can be written as a combination of parallel and perpendicular coefficient,

$$K = K_\parallel \cos^2\theta + K_\perp \sin^2\theta, \tag{2.11}$$

where θ is an angle between the magnetic field and the particle velocity. From equations (2.9), (2.10) and (2.11), the effective diffusion coefficient along the shock normal is then written as

$$K = \frac{1}{3}\xi r_g c\left(\cos^2\theta + \frac{\sin^2\theta}{1+\xi^2}\right). \tag{2.12}$$

2.4 Particle Acceleration Sites in the Milky Way Galaxy

In §2.2, we explained the basic mechanism of particle acceleration in shock. The shock needs to be sustained for a long term to accelerate particles to high energies. Here we describe the candidate acceleration sites of high energy particles in the Milky Way Galaxy.

Supernova remnants (SNRs) are the most plausible candidates of the particle accelerators. An SNR is the structure produced by the shocks of the supernova explosion. Two types of supernova type I and II are known. Originally the two types were defined by the absence/presence of the hydrogen lines in the optical band. However, it is now considered that progenitor of type I (precisely speaking type Ia) is the white dwarf in a binary system and that of the other types is the evolved massive star. Because the SNR caused by these two types of the supernova share the common properties, we do not distinguish them in the following description. Its explosion energy is typically 10^{53} ergs. Roughly 99% of this energy is radiated away by neutrinos, while about 1% of which is converted into the kinetic energy. The stellar ejecta carrying of order 10^{51} ergs of kinetic energy interact with surrounding circumstellar or interstellar medium. Initial speed of the ejecta reaches up to 10^{3-4} km s^{-1}, which form strong shock waves, gradually decelerating over tens of thousands of years. The acceleration of ~ 100 TeV electrons in SNRs was first suggested by the discovery of synchrotron X-ray emission from shock fronts of an SNR SN 1006 (Koyama et al., 1995). In its shock front, electrons are accelerated by the first-order Fermi acceleration explained in §2.2. Because there is no mechanism to discriminate protons from electrons, protons are considered to be similarly accelerated in the SNR. RX J1713.7–3946 is the first SNR detected in TeV γ-ray, whose shell was resolved in γ-rays (Aharonian et al., 2004). Cassiopeia A, RCW86, RX J0852.0–4622 (Vela Jr.) and CTB 37B are other samples of TeV emitting SNRs (Hinton, 2007b; Aharonian et al., 2008b).

Pulsar wind nebulae (PWNe) are also candidate accelerators. A supernova explosion of a massive star may leave a neutron star. Pulsars are highly magnetized, rapidly rotating neutron stars emitting beams of radiation. The pulsar generates relativistic electron and positron flow, which is called "pulsar wind". The rapid spin of the pulsar steadily slows down converting its rotational energy into the kinetic energy of the pulsar winds. The pulsar winds collide with their surrounding medium to form a shock, called a termination shock where particles are accelerated. The Crab nebula is the most well-known PWN, associated with a supernova explosion in 1054 AD. It is the brightest, steady and compact source in both X-ray and TeV γ-ray band, whose emission mechanism are the synchrotron radiation and inverse Compton scattering by the relativistic electrons, respectively. PWNe have now emerged as the largest population of TeV sources (Hinton, 2007b).

The other candidate accelerators in our Galaxy are the star forming regions and the binary systems, and some of those were detected in the VHE γ-ray band. However, the number of those with established multi-wavelength counterparts is still small (Hinton, 2007b).

Until now, the number of SNRs whose association with TeV γ-ray sources are well-established is four, while that of PWNe is nine (Hinton, 2007b). Since PWNe

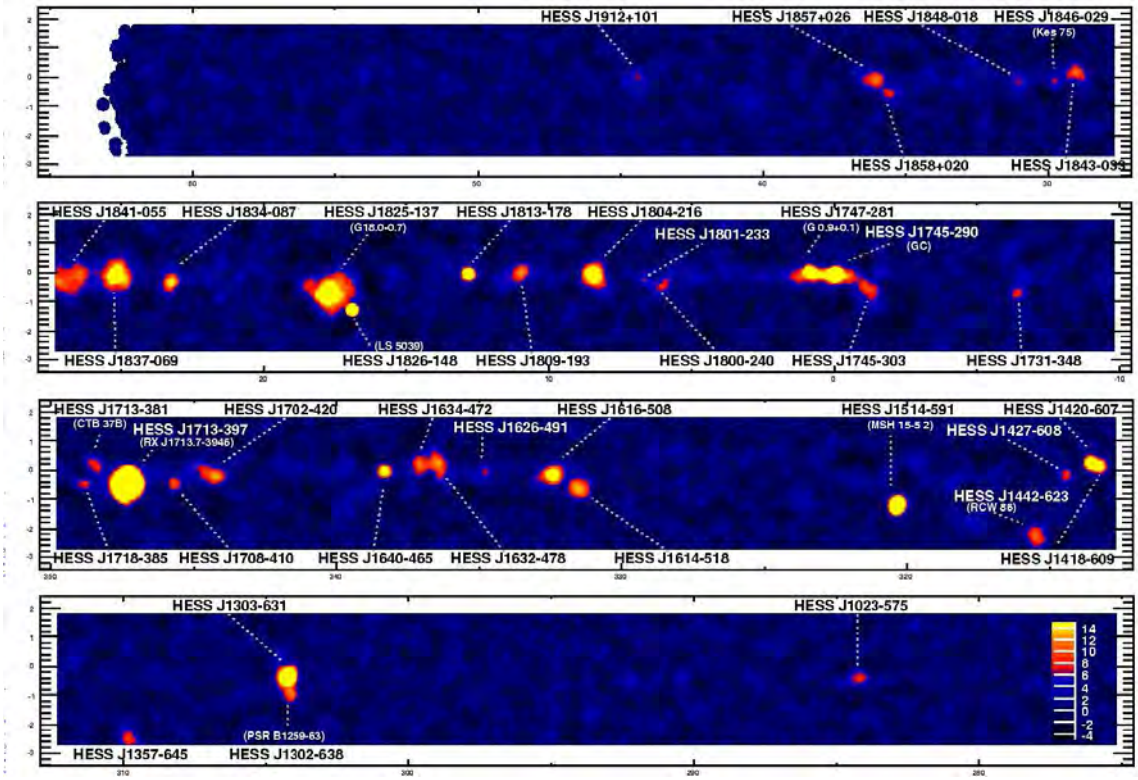

Figure 2.3: The HESS survey image of the inner galaxy in $\sim$ 1 TeV γ-ray band. The color scale indicates the statistical significance of extended sources. The sources with no name in parentheses are unID TeV sources. This figure is adapted from Hinton (2007b).

may be the majority of Galactic accelerators, we concentrate on the study of PWNe.

2.5 Newly Discovered Sources in the VHE γ-ray band on the Galactic Plane

In 1980's, a ground-based γ-ray imaging telescope was constructed, named Whipple Observatory. The telescope detected γ-ray signal from the Crab Nebula for the first time in 1989 (Weekes et al., 1989). Since the detection, ground-based technique has grown to be the most successful approach in γ-ray astronomy. It is based on the detection of the Cherenkov light produced by photon initiated cascades in the Earth's atmosphere. This technique can also reject a large fraction of the cosmic ray background based on the shape of the Cherenkov images. Multiple Cherenkov telescopes allows stereoscopic reconstruction of the shower, which provides a further breakthrough in sensitivity and resolution. Three multiple Cherenkov telescope arrays

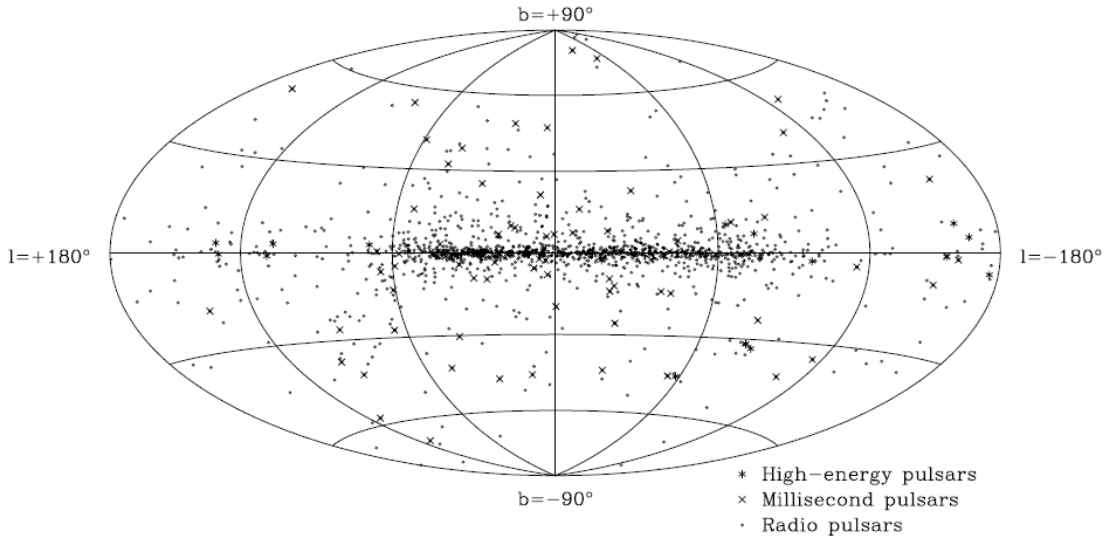

Figure 2.4: Distribution of pulsars in Galactic coodinate with the Galactic center at the center of the plot. This figure is taken from Manchester et al. (2005).

are currently in operation: VERITAS, CANGAROO-III and HESS.

HESS is a system of four imaging atmospheric Cherenkov telescopes located in the Khomas highlands of Namibia. Until the completion of HESS in early 2004, no VHE γ-ray survey of comparable sensitivity of the southern sky or of the central region of the Galaxy had been performed.

Galactic plane survey with HESS was conducted and revealed the presence of tens of new VHE γ-ray sources (Aharonian et al., 2005a, 2006a). This survey covers essentially the whole inner galaxy: $-85° < l < 60°, -2.5° < b < 2.5°$, while the positive galactic latitude extent of this survey is limited by zenith angle constraints. Figure 2.3 shows the detected VHE sources in the survey. Some of them are identified as SNRs, PWNe and binaries. However, the majority of galactic VHE γ-ray sources have no clear counterpart at other wavelengths. These sources are thus called "unidentified (unID) TeV sources". Today, there are 30 such unidentified TeV sources on the Galactic plane (Hinton, 2007b).

2.6 Pulsars and Pulsar Wind Nebulae

Neutron stars are formed through the supernova explosion of a massive star ($\geq 8\ M_\odot$). They are highly compact (radius of $\sim$10 km), yet having a mass comparable to the Sun (mass of $\sim 1.4\ M_\odot$). Pulsars are highly magnetized, rapidly rotating neutron stars, which emit beams of radiation in the energy range from radio to γ-ray. Because

Figure 2.5: Color composite of the Crab synchrotron nebula showing a Chandra X-ray image in blue, a visible light mosaic taken with HST in green, and a VLA radio image in red. The pulsar is seen as the bright blue point source at the center of the image. Adapted from Hester (2008).

the emission can be observed only when the beam points to us, the signals detected are pulsed, which is responsible for the name of "pulsar". Since the discovery of the first pulsar, the number of known pulsars has now grown to more than 1500. Figure 2.4 shows the distribution of pulsars in Galactic coodinate. Most of the high-energy pulsars are young (median characteristic age of $\sim 2 \times 10^4$ yr) and hence are concentrated along the Galactic plane, whereas most of the milisecond pulsars are very old (median characteristic age $\sim 4 \times 10^9$ yr) and have left from their region of birth (Manchester et al., 2005).

A neutron star rotating in the strong magnetic field induces large electric field. Accelerated by the electric field, charged particles move close to the speed of light. They move along the curved magnetic field lines, and emit γ-rays through curvature radiation. These γ-rays interact with surrounding magnetic field or photons and produce electron-positron pairs. The produced electron-positron pairs are accelerated, move along the magnetic field, and emit γ-rays. Thus electron-positron pairs are produced in sequence and flow out as a very high energy plasma. This flow is called a pulsar wind.

In some case of rotation powered pulsars, diffuse emission from the region surrounding the pulsar is observed, which is called pulsar wind nebula. This emission is understood to be caused by the interaction between the pulsar wind and the surrounding material. Figure 2.5 shows the Crab nebula in X-ray, visible, and radio wave bands surrounding the pulsar at the center of the image.

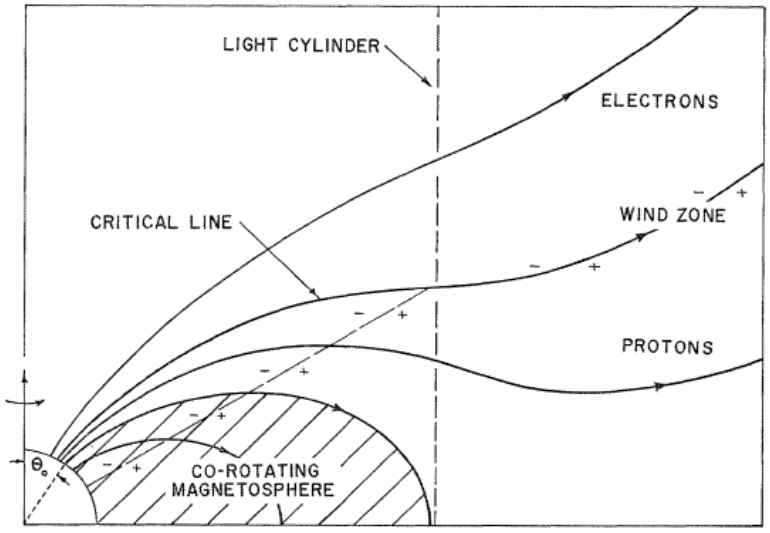

Figure 2.6: Schematic diagram showing the corotating magnetosphere around a pulsar. This figure is adapted from Goldreich & Julian (1969).

The emission from PWNe is powered by pulsar's rotational energy. First we introduce the properties of the rotation powered pulsars.

2.6.1 Properties of Rotation Powered Pulsars

A rotation-powered pulsar is powered by the release of the rotation energy of the neutron star. The energy loss causes the pulsar's spin down. Regarding the cause of energy loss as the magnetic dipole radiation, we can estimate an equatorial surface magnetic field strength:

$$B_{\rm s} = \left(\frac{3\mu_0 c^3 I P \dot{P}}{32\pi^3 R_{\rm N}^6} \right)^{\frac{1}{2}} = 3.2 \times 10^{19} \left(\frac{P}{1\ {\rm s}} \right)^{\frac{1}{2}} \dot{P}^{\frac{1}{2}}\ {\rm G}, \tag{2.13}$$

where P is a spin period, $\dot{P}$ is a period derivative with respect to time, $\dot{P} \equiv dP/dt$, μ_0 is the permeability of free space, $R_{\rm N}$ is the radius of the neutron star, and I is the neutron star's moment of inertia. Here we assume $R_{\rm N} = 10$ km and $I = 10^{45}$ g cm^2. Magnetic field strength inferred from Equation (2.13) range between $\sim 10^8$ G for millisecond pulsars up to $> 10^{15}$ G for magnetars. Most pulsars with prominent PWNe have inferred magnetic fields in the range 1×10^{12} to 5×10^{13} G.

The poloidal magnetic-field structure is shown in figure 2.6. The particles restricted to closed magnetic-field lines corotate with the pulsar. The velocity of corotating magnetosphere with the pulsar equals the velocity of light at the light cylinder.

A radius of the light cylinder is

$$R_{\rm LC} \equiv \frac{c}{\Omega} = 5 \times 10^9 \left(\frac{P}{1\ {\rm s}}\right)\ {\rm cm}, \tag{2.14}$$

where $\Omega = 2\pi/P$, and the magnetic field strength at the light cylinder is given by

$$B_{\rm LC} = B_{\rm s}\left(\frac{R_{\rm N}}{R_{\rm LC}}\right)^3 = 3.0 \times 10^8 \left(\frac{P}{1\ {\rm s}}\right)^{-5} \dot{P}^{\frac{1}{2}}\ {\rm G}. \tag{2.15}$$

The magnetic-field lines which pass through the light cylinder are open, and charged particles stream out along them.

We assume that a pulsar's spin down can be described as $\dot{\Omega} = -k\Omega^n$, and n is the "breaking index". If we assume k to be a constant, the age of the pulsar is derived as

$$\tau = \frac{P}{(n-1)\dot{P}}\left\{1 - \left(\frac{P_0}{P}\right)^{n-1}\right\}. \tag{2.16}$$

If we assume $n = 3$, which correspond to spin down via magnetic dipole radiation, and $P_0 \ll P$, Equation (2.16) becomes

$$\tau_c \equiv \frac{P}{2\dot{P}}, \tag{2.17}$$

which is called the "characteristic age" of a pulsar. Although equation (2.17) often overestimates the true age, it is widely used as a representative age of the pulsar. For example, the characteristic age of the Crab Nebula is $\sim$1300 yr, which is close to the true age of $\sim$950 yr.

The spin down luminosity of the pulsar, $\dot{E} = -dE_{\rm rot}/dt$, is the rate of the rotational kinetic energy loss:

$$\dot{E} = -I\Omega\dot{\Omega} = 4\pi^2 I \frac{\dot{P}}{P^3}. \tag{2.18}$$

For example, $\dot{E}$ for the Crab pulsar is 5×10^{38} ergs s^{-1}, which is the largest among the known pulsars. Relatively young and energetic pulsars with $\dot{E} \geq 4 \times 10^{33}$ ergs s^{-1} produce prominent PWNe (Kargaltsev et al., 2008b).

2.6.2 Pulsar Wind Termination Shock

The highly relativistic pulsar wind and its wound-up toroidal magnetic field inflate an expanding bubble whose outer edge is confined by the expanding shell of supernova ejecta. Because the relativistic bulk velocity of the wind leaving the pulsar magnetosphere is obviously supersonic with respect to the ambient medium, such a wind produces a termination shock (TS) at a distance $R_{\rm TS}$ from the pulsar where the bulk

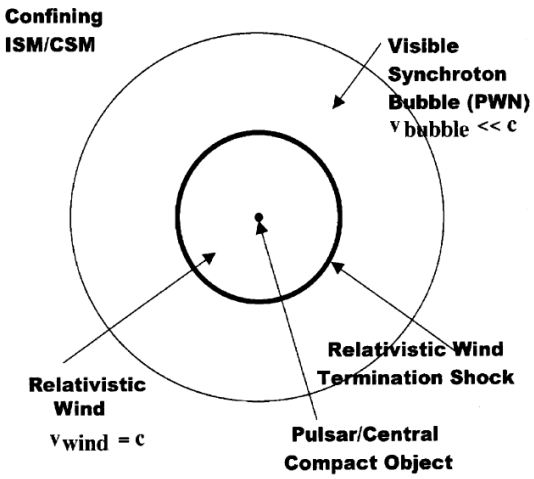

Figure 2.7: Schematic structure of a PWN, for which the pulsar space velocity is small compared to the bubble's expansion speed. Adapted from Arons (2004).

wind pressure, $P_w \sim \dot{E}/(4\pi c R_{\rm TS}^2)$, is equal to the ambient pressure $P_{\rm amb}$. The TS radius is estimated as

$$R_{\rm TS} \sim \sqrt{\dot{E}/(4\pi c P_{\rm amb})} \sim 0.05 \left(\frac{\dot{E}}{10^{36}\ {\rm ergs\ s^{-1}}}\right)^{1/2} \left(\frac{P_{\rm amb}}{10^{-10}\ {\rm dyn\ cm^{-2}}}\right)^{-1/2} {\rm pc}. \tag{2.19}$$

Upstream of the termination shock, the particles do not radiate, but flow relativistically along with the frozen-in magnetic field. At the shock, particles are thermalized and reaccelerated, producing synchrotron emission in the magnetic field and inverse Compron radiation in the ambient radiation field. Particles flow in the downstream with the advection speed to the outer boundary of the nebula, where the relativistic flow is confined by the supernova remnant (Kennel & Coroniti, 1984).

2.7 Emission from PWNe

2.7.1 Emission Processes

Relativistic electrons interact with surrounding magnetic field and radiate radio to hard X-ray photons through synchrotron radiation. In addition, relativistic electrons scatter the cosmic microwave background photons in the interstellar medium and convert a low-energy photons to high-energy photons. This process is called inverse Compton (IC). Figure 2.8 indicates the wide band spectral energy distribution of the Crab nebula shown in Aharonian & Atoyan (1998). The synchrotron and IC mechanisms provide a reasonable explanation of the overall nonthermal radiation of the

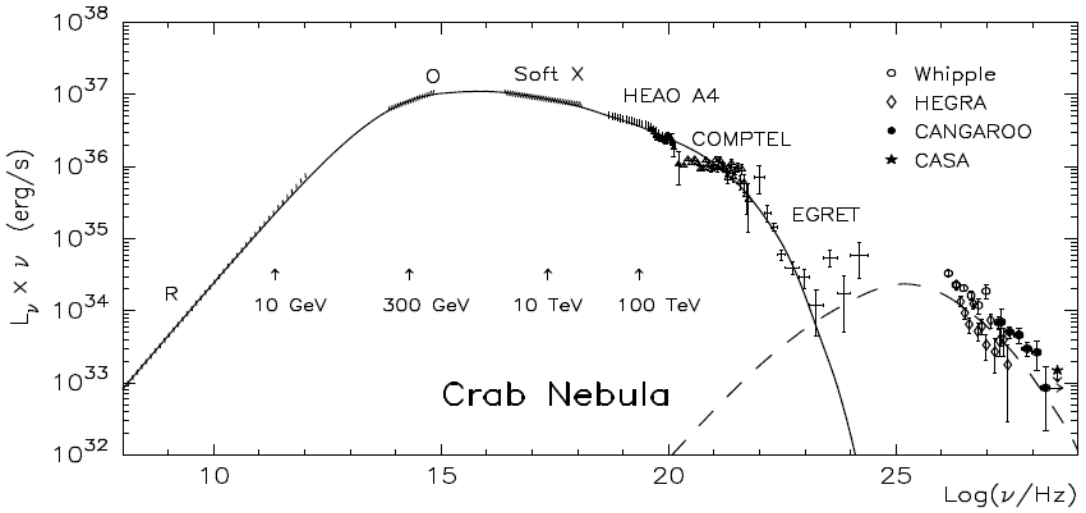

Figure 2.8: Wide band spectral energy distribution of the Crab nebula, adapted from Aharonian & Atoyan (1998). The solid and dashed curves correspond to the calculated synchrotron and inverse Compton components of radiation, respectively.

Crab nebula. In the case of the Crab nebula, the target photons for the IC scattering are synchrotron, far-infrared (FIR), cosmic microwave background (CMBR) photons (Atoyan & Aharonian, 1996).

Here we overview both emission processes according to Rybicki & Lightman (1979), particularly focusing to the spectral shapes.

Synchrotron Radiation

Relativistic particles interacting with a magnetic field will radiate. This radiation is known as synchrotron radiation.

Consider the case that a particle of a mass m_e and charge q is moving with a velocity v in a uniform magnetic field B. The power per unit frequency emitted by each electron with a frequency ω is given as

$$P(\omega) = \frac{\sqrt{3}}{2\pi} \frac{q^3 B \sin\alpha}{m_e c^2} F\left(\frac{\omega}{\omega_c}\right), \tag{2.20}$$

and

$$\omega_c = \frac{3\gamma^2 eB \sin\alpha}{2m_e c}, \tag{2.21}$$

where $\gamma^{-1} = \sqrt{1-(v/c)^2}$, α is the pitch angle, which is the angle between field and

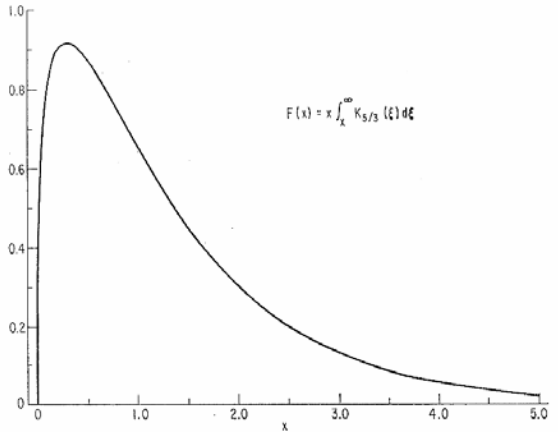

Figure 2.9: Function describing the total power spectrum of synchrotron emission as a function of $x = \omega/\omega_c$. Adapted from Blumenthal & Gould (1970).

velocity, and the function $F(x)$ is a nondimensional function, described as

$$F(x) \equiv x \int_x^\infty K_{\frac{5}{3}}(\eta) d\eta, \tag{2.22}$$

where $K_{\frac{5}{3}}(\eta)$ is the modified Bessel function of 5/3 order. $F(x)$ has a peak at $x \sim 0.29$ as shown in figure 2.9. Asymptotic forms for small and large values of x are:

$$F(x) \sim \frac{4\pi}{\sqrt{3}\,\Gamma(\frac{1}{3})} \left(\frac{x}{2}\right)^{\frac{1}{3}}, \qquad x \ll 1, \tag{2.23}$$

$$F(x) \sim \left(\frac{\pi}{2}\right)^{\frac{1}{2}} e^{-x} x^{\frac{1}{2}}, \qquad x \gg 1. \tag{2.24}$$

Integrating the power per unit frequency described in equation(2.20) over all frequencies or ω, we can derive the total power as

$$P = \frac{4}{3} \sigma_T c \beta^2 \gamma^2 U_B, \tag{2.25}$$

where $\sigma_T = 8\pi r_0^2/3$ is the Thomson cross section, and U_B is the magnetic energy density, $U_B = B^2/8\pi$.

Particles accelerated at the shock are distributed according to a power-law distribution as explained in §2.2. Let us assume that the number density of particles with energies between E and $E + dE$ is described by a power-law distribution in the form

$$N(E)dE \propto E^{-p} dE, \tag{2.26}$$

or

$$N(\gamma)d\gamma \propto \gamma^{-p} d\gamma. \tag{2.27}$$

The total power per unit volume per unit frequency is given by the integral of $N(\gamma)d\gamma$ times the single particle radiation formula over all energies or γ. Thus we have

$$P_{\rm tot}(\omega) \propto \int P(\omega)\gamma^{-p}d\gamma \propto \int F\left(\frac{\omega}{\omega_c}\right)\gamma^{-p}d\gamma, \tag{2.28}$$

Let us change variables of integration to $x \equiv \omega/\omega_c$, noting $\omega_c \propto \gamma^2$;

$$P_{\rm tot}(\omega) \propto \omega^{-(p-1)/2}\int F(x)x^{(p-3)/2}dx. \tag{2.29}$$

If the energy band is sufficiently wide, the integral is approximately constant. In that case, we have

$$P_{\rm tot}(\omega) \propto \omega^{-(p-1)/2}, \tag{2.30}$$

so that the spectral index s can be written with the particle distribution index p as

$$s = \frac{p-1}{2}. \tag{2.31}$$

Above X-ray energies, the emission is often discribed as a power-law distribution of photons, such that $N_E \propto E^{-\Gamma}$, where N_E is the number of photons emitted between energies E and $E + dE$, and $\Gamma \equiv 1 + s = (1 + p)/2$ is the photon index. When $p \sim 2$ from equation (2.6), Γ becomes $\sim$1.5.

Inverse Compton Scattering

Now we consider the Compton scattering of a single photon off a single electron. Here we show average formulas for the case of a given isotropic distribution of photons scattering off a given isotropic distribution of electrons.

Here we consider the case that the incident photon energy in the electron rest frame is significantly low compared with the rest energy of electron, implying Thomson scattering in the rest frame (Thomson limit). The power per unit frequency emitted by each electron is given as

$$P = \frac{4}{3}\sigma_T c\gamma^2\beta^2 U_{\rm ph}, \tag{2.32}$$

where $U_{\rm ph}$ is the initial photon energy density.

Now we assume the electron energy distribution as Eq.(2.27) again, and suppose the isotropic incident photon field is monoenergetic:

$$I(\epsilon) = F_0\delta(\epsilon - \epsilon_0), \tag{2.33}$$

where F_0 is the number of photons per unit area, per unit time per steradian. ere, we consider only the case that electrons are relativistic, or $\beta \sim 1$ ($\gamma \gg 1$). Under these assumptions, the emission function is given by

$$j(\epsilon_1) = \frac{3N\sigma_T F_0}{4\gamma^2\epsilon_0}f(x), \tag{2.34}$$

where ϵ_1 is the photon energy after scattering, and

$$f(x) \equiv \frac{2}{3}(1-x), \qquad 0 < x < 1, \tag{2.35}$$

where

$$x \equiv \frac{\epsilon_1}{4\gamma^2 \epsilon_0}. \tag{2.36}$$

Let us use the initial photon number density $v(\epsilon)$ related to the isotropic intensity by $v(\epsilon) = 4\pi c^{-1} I(\epsilon)$. Then the total power per volume per energy resulting from the scattering of an arbitrary initial spectrum off a power law distribution of relativistic electrons is

$$\begin{aligned} \frac{dE}{dV\ dt\ d\epsilon_1} &= 4\pi\epsilon_1 j(\epsilon_1) \\ &= 3c\sigma_T C 2^{p-2} \epsilon_1^{-(p-1)/2} \int d\epsilon \epsilon^{(p-1)/2} v(\epsilon) \int_{x_1}^{x_2} dx x^{(p-1)/2} f(x), \end{aligned} \tag{2.37}$$

where $x_1 \equiv \epsilon_1/(4\gamma_1^2\epsilon)$ and $x_2 \equiv \epsilon_1/(4\gamma_2^2\epsilon)$. Integrating over all ϵ_1, we obtain the spectral index s,

$$s = \frac{p-1}{2}, \tag{2.38}$$

which is identical to the case of synchrotron emission (see Eq.(2.31)).

2.7.2 Energy Scales and Lifetimes of X-Ray Synchrotron and VHE Gamma-Ray IC Emitting Electrons

Here we estimate the energy and lifetime of electrons emitting X-ray photons through synchrotron radiation and inverse Compton scattered VHE γ-ray photons.

Electron Energy Scale

The characteristic energy of the synchrotron photons is $\epsilon_{\rm syn} \simeq \hbar\omega_c/3$, where ω_c is a frequency defined in equation (2.21). In the case of isotropical pitch angle ψ, the photon energy is

$$\epsilon_{\rm syn} \simeq 0.2 \left(\frac{B}{10\ \mu{\rm G}}\right) \left(\frac{E_e}{1\ {\rm TeV}}\right)^2\ {\rm eV}. \tag{2.39}$$

For IC scattering in the Thomson limit, the characteristic energy of IC photons is $\epsilon_{\rm IC} \simeq (4/3)h\nu_0(E_e/m_e c^2)^2$, where $h\nu_0$ is the energy of the target photons. Thus

$$\epsilon_{\rm IC} \simeq 5 \left(\frac{h\nu_0}{10^{-3}\ {\rm eV}}\right) \left(\frac{E_e}{1\ {\rm TeV}}\right)^2\ {\rm GeV}. \tag{2.40}$$

Solving equation (2.39) and (2.40) for the energy of the electron, we obtain

$$E_e^{\rm syn} = 70 \times \left(\frac{B}{10\ \mu{\rm G}}\right)^{-\frac{1}{2}} \left(\frac{\epsilon_{\rm syn}}{1\ {\rm keV}}\right)^{\frac{1}{2}}\ {\rm TeV}, \tag{2.41}$$

$$E_e^{\rm IC} = 0.5 \times \left(\frac{h\nu_0}{1\ {\rm eV}}\right)^{-\frac{1}{2}} \left(\frac{\epsilon_{\rm IC}}{1\ {\rm TeV}}\right)^{\frac{1}{2}}\ {\rm TeV}. \tag{2.42}$$

For the CMBR seed photons, the mean energy of the target photons is $h\bar{\nu}_0 = kT \sim 6\times10^{-4}$ eV, thus the production of the IC γ-ray photon with $\epsilon_{\rm IC} \sim 1$ TeV requires the electron energy of $E_e^{\rm IC} \sim 20$ TeV, which is typically lower than that required energy of $E_e^{\rm syn} \sim 70$ TeV to produce a synchrotron photon of $\epsilon_{\rm syn} \sim 1$ keV. Considering the target photons as FIR originated from the dust with the temperature of ~ 100 K (characteristic value for the Crab (Marsden et al., 1984)) and the starlight photons with the temparature of ~ 5000 K, the electron energy is required $E_e \sim 3$ TeV and 0.5 TeV to Compton-upscatter the target photons to 1 TeV γ-rays, respectively.

Electron Lifetime

If we define the lifetime of electrons in a magnetic field B and a photon field of energy density $U_{\rm ph}$ to be $\tau = E_e/P$, the lifetime of electrons is determined as

$$\begin{aligned}\tau(E_e) &= \left(\frac{4}{3}\sigma_{\rm T} c U_0 E_e / m_e^2 c^4\right)^{-1} \\ &= 3.1\times10^5 \times \left(\frac{E_e}{1\ {\rm TeV}}\right)^{-1} \left(\frac{U_0}{1\ {\rm eV\ cm^{-3}}}\right)^{-1}\ {\rm yr},\end{aligned} \tag{2.43}$$

where $U_0 = U_B + U_{\rm ph}$ and the magnetic energy density $U_B = B^2/8\pi$. If we assume the target photon as CMBR, the photon energy density $U_{\rm ph} = 0.25$ eV cm^{-3}. In the case of low magnetic fields comparable with the ISM magnetic field, $B_{\rm ISM} \sim 3\ \mu$G, both synchrotron and IC processes, with $U_0 \sim 0.5$ eV cm^{-3} equally contribute to the total energy losses. Typically, the lifetime $\tau \sim 30$ kyr for the electrons with the energy of $E_e^{\rm IC} \sim 20$ TeV, while $\tau \sim 9$ kyr for those with the energy of $E_e^{\rm syn} \sim 70$ TeV. In a high magnetic fields such as $B \sim 300\ \mu$G (the average magnetic field in the Crab Nebula), a magnetic energy density $U_B \sim 5.7\times10^4$ eV cm^{-3} is much larger than the photon energy density of CMBR. Typically, the lifetime $\tau \sim 0.3$ yr for the electrons with the energy of $E_e^{\rm IC} \sim 20$ TeV, while $\tau \sim 0.08$ yr for those with the energy of $E_e^{\rm syn} \sim 70$ TeV.

Chapter 3

Instruments

In this study, we use observational data obtained with four X-ray satellites; ASCA, Suzaku, Chandra, XMM-Newton. The schematic view of these satellites is shown in figure 3.1. In the following sections, we introduce the equiped instruments and their properties.

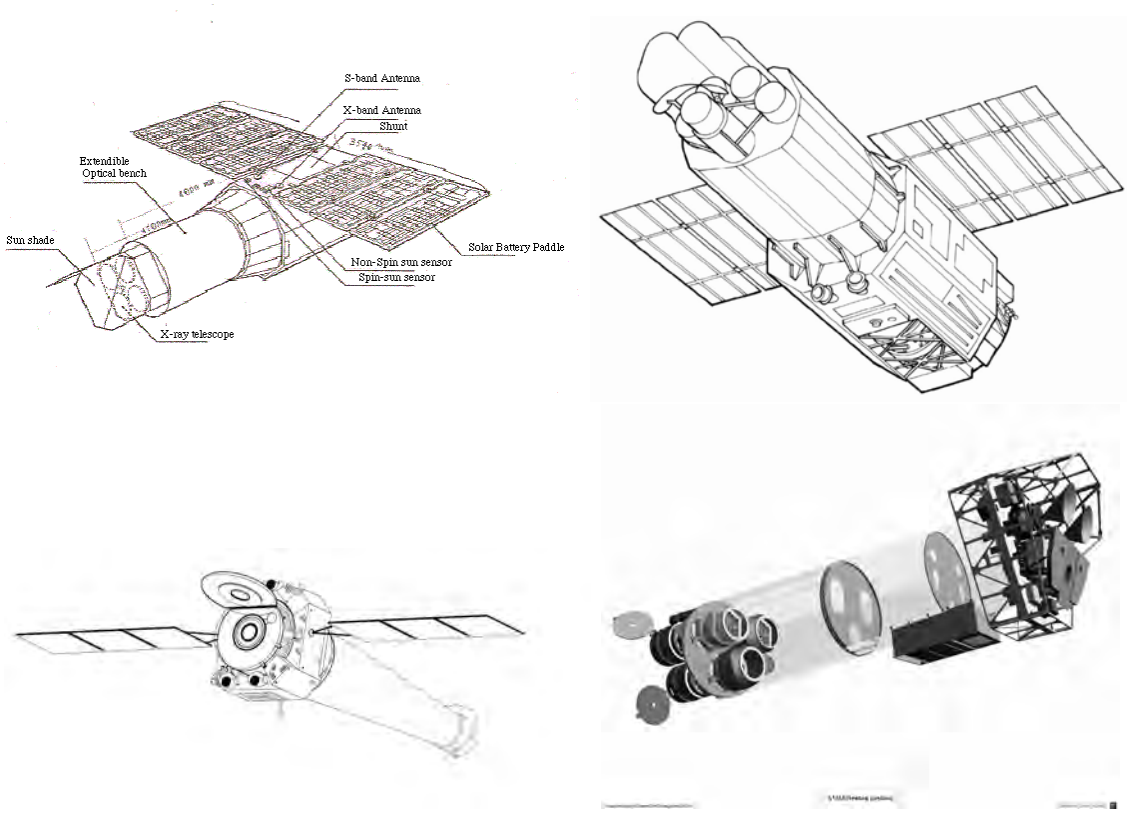

Figure 3.1: Schematic view of the ASCA (top left), Suzaku (top right) Chandra (bottom left) and XMM-Newton (bottom right) satellites in orbit after the deployment of the solar paddles and the extensible optical bench.

3.1 ASCA

ASCA (Advanced Satellite for Cosmology and Astrophysics) is the fourth Japanese X-ray astronomy satellite launched on February 20, 1993 (Tanaka et al., 1994). ASCA was equipped with two types of instruments at the focal plane of X-ray telescopes (XRT: Serlemitsos et al. (1995)): two sets of the CCD camera (Solid-state Imaging Spectrometer, SIS: Burke et al. (1994)) and two sets of the gas scintillation imaging proportional counter (Gas Imaging Spectrometer, GIS: Ohashi et al. (1996)). Schematic view of ASCA is shown in figure 3.1. Characteristics of the scientific instruments are summarized in table 3.1.

ASCA was the first X-ray astronomy satellite which had the imaging capability up to 10 keV. Combined with the high energy resolution of SIS, ASCA provided very unique data useful for the spectroscopic studies of X-ray sources. Simultaneously, the wide field of view of GIS made it suitable for the survey observations. In fact, ASCA carried out numbers of galactic surveys during its long life of 8 years. The survey data constitute an important part of the ASCA archives.

3.1.1 XRT

ASCA utilized four identical sets of the grazing-incidence X-ray telescope. The telescope adopted multi-nested (119 layers) thin-foil conical optics, which could allow maximum usage of the aperture for X-ray reflection. Thanks to this technology, XRT could achieve a large effective area, yet light-weighted. The angular resolution of the telescope was modest, with a half-power diameter (diameter which encircles 50% of the photons of a point source) of $\sim$3.6 arcmin. However, the point-spread function contained a sharp cusp, which enabled us to resolve two point sources separated only $\sim$1 arcmin.

3.1.2 SIS

Two of the XRTs had the X-ray sensitive CCD camera (SIS) at the focal plane operated in the photon-counting mode. Basic structure of the X-ray sensitive CCD is same as that of the optical CCD, but its operation principle is very different. In an optical CCD, large numbers of photons are photo-absorbed in a single CCD pixel; this means that CCD is used to measure the energy flux. On the other hand, an X-ray CCD is read out frequently so that each pixel does not detect more than a single X-ray photon (so-called photon counting mode). Because an X-ray photon produces thousands of electron-hole pairs and each pixel detects at most a single X-ray photon, we can determined the energy of the incident X-ray photon accurately by measuring the number of generated electrons. SIS achieved a good energy resolution of 2% at

Table 3.1: Overview of ASCA capabilities

XRT	Focal Length	3.5 m
	Field of View	$24'$ at 1 keV
		$16'$ at 7 keV
	Geometrical Area/telescope	558 cm^2
	Weight/telescope	9.84 kg
	Effective Area/telescope	300 cm^2 at 1.5 keV
		150 cm^2 at 7.0 keV
	Angular Resolution	$3'.6$ (HPD)
SIS	Field of View	$20' \times 20'$
	Bandpass	0.4–10 keV
	Number of Pixels/CCD	420×422
	Pixel Size	27 μm $\times$ 27 μm
	Energy Resolution	$\sim$2% at 6 keV
	Time Resolution	4, 8, 16 s (faint and bright mode)
		16 ms (parallel sum mode)
GIS	Field of View	$50'$ in diameter
	Bandpass	0.7–20 keV[1]
	Energy Resolution	7.8 % at 6 keV
	Time Resolution	61 μs (maximum)

[1] The upper bound becomes 10 keV when combined with the mirror.

6 keV with such a method. This energy resolution is an order of magnitude better than that of a conventional proportional counter.

Each SIS is equipped with 4 sets of CCD chips arranged in the 2×2 configuration. When only a single CCD chip is read out repeatedly (1-ccd mode), exposure time can be as short as 4 sec. However, field of view is reduced to $10' \times 10'$. The 1-ccd mode was used to observe relatively bright point sources. The 4 CCD chips can also be read out sequentially (4-ccd mode). In this mode, field of view is as large as $20' \times 20'$, but the exposure time is increased to 16 sec. The 4-ccd mode was used to observe extended sources.

The electron cloud produced by an X-ray photon absorbed in the depletion layer extends at most 4 CCD pixels (2×2 pixels). Therefore, if we output the pulse-height information of 3×3-pixels centered on the X-ray absorbed pixel to the telemetry, we can recover the original pulse height of the X-ray photon on ground. On the other hand, it is also possible to estimate the original pulse height of the X-ray photon on board. The former is called a faint mode in SIS, and the latter a bright mode. Because various corrections (eg. charge transfer inefficiency, dark frame), which was difficult on board, were possible only on ground, we could obtain better performance of SIS in the faint mode. On the other hand, the faint mode required larger telemetry capacity. Thus it was not usable for bright sources.

3.1.3 GIS

ASCA was equipped with two identical sets of GIS, gas scintillation imaging proportional counter. It is basically a gas counter, but does not utilize the electron avalanche unlike the conventional proportional counters. An X-ray photon entered the detector through the entrance window (10 μm thick Be) is photo-absorbed in the detector gas (Xe 90% and He 10%) to produce the primary electron cloud. The electron cloud is accelerated by the moderately strong electric field to excite the Xe atoms through collisions. However, the electric field is adjusted not to ionize the Xe atoms. Thus the number of electrons does not change. The excited Xe atoms produce UV scintillation photons when de-excite, which are detected by the (position sensitive) photo-multiplier tube. Because the number of electrons does not change in the gas scintillation proportional counter, statistical fluctuation due to the electron avalanche is suppressed. This enabled the GIS to achieve a factor of 2 better energy resolution (7.8% at 6 keV) compared to the conventional proportional counter.

GIS worked complementary to the SIS. It afforded larger field of view, better time resolution, and better detection efficiency in higher energy band. On the other hand, energy and position resolutions were better in SIS. GIS was not sensitive to X-rays below $\sim$1 keV due to the photo-electric absorption of the entrance window.

3.2 Suzaku

The fifth Japanese X-ray astronomy satellite, Suzaku, was launched on July 10, 2005, and was successfully put into a near-circular orbit at an altitude of ∼570 km and an inclination of 32 degrees. However, one of the main instruments, the X-ray micro-calorimeter (XRS), stopped operation due to the sudden loss of the liquid He at the initial stage of the mission. Thus the rest of two types of instruments are used for scientific observations: the X-ray Imaging Spectrometer (XIS: Koyama et al. (2007)) at the focal plane of X-Ray Telescope (XRT: Serlemitsos et al. (2007)) and the Hard X-ray Detector (HXD: Takahashi et al. (2007), Kokubun et al. (2007)). XIS is similar to ASCA SIS in many respects, but afford much larger flexibility in reading out the CCD. HXD is a non-imaging detector which achieved very low background utilizing the well-type active shield. We summarize the characteristics of these instruments in table 3.2. Schematic view of Suzaku on orbit is shown in figure 3.1.

In spite of the loss of XRS, Suzaku is producing unique data of X-ray universe. Suzaku is especially suited for the study of the non-thermal phenomena, such as synchrotron emission from the relativistic electrons, Compton up-scattered emission from the vicinity of the black holes, and so on, because of the simultaneous coverage of the soft and hard X-ray bands. Furthermore, low and stable non-X-ray background of XIS makes it suited to observe diffuse X-ray sources with low surface brightness. Because many of the non-thermal X-ray sources are extended as we see in this thesis, Suzaku is best suited for the study of the non-thermal sources.

3.2.1 XRT

Suzaku is equipped with a total of five light-weight thin-foil X-Ray Telescopes (XRTs). The structure of XRT is basically the same as that on board ASCA. It approximates the Walter-I optics with two conical reflectors made of thin aluminum foil. This makes it possible to produce a light-weighted telescope, yet have a large effective area. However, angular resolution remains moderate compared to the currently operating best X-ray telescope. Unlike the ASCA XRTs, Suzaku XRTs are equipped with the pre-collimators, which cut-off the stray light. This is especially useful when observing a dim source near the bright one. Furthermore, the pre-collimator helps to reduce the contribution of the cosmic X-ray background. This is essential to observe dim, extended sources.

Four XRTs (XRT-I) utilize XIS as the focal plane detector, and the other XRT (XRT-S) utilizes XRS. As we explained earlier, XRS (and XRT-S) is not operational now. The focal length of XRT-I is 4.75 m and the half-power diameter (HPD) is $\sim 1'.9$. We show the point-spread function and encircled energy function in figure 3.3. It can be seen from the figure that, although the angular resolution of XRT is moderate, its

Table 3.2: Overview of Suzaku capabilities

XRT	Focal Length	4.75 m
	Field of View	$20'$ at 1 keV
		$14'$ at 7 keV
	Geometrical Area/telescope	873 cm^2
	Weight/telescope	19.3 kg
	Effective Area/telescope	450 cm^2 at 1.5 keV
		250 cm^2 at 7.0 keV
	Angular Resolution	$2'.0$ (HPD)
XIS	Field of View	$17'.8 \times 17'.8$
	Bandpass	0.2–12 keV
	Number of Pixels/CCD	1024×1024
	Pixel Size	24 μm $\times$ 24 μm
	Energy Resolution	$\sim$ 2 % at 6 keV
	Effective Area	340 cm^2 (FI), 390 cm^2 (BI) at 1.5 keV
		150 cm^2 (FI), 100 cm^2 (BI) at 8 keV
	Time Resolution	8 s (Normal mode)
		7.8 ms (P-Sum mode)
HXD	Field of View	$4°.5 \times 4°.5$ ($\geq$100 keV)
	Field of View	$34' \times 34'$ ($\leq$100 keV)
	Bandpass	10–600 keV
	– PIN	10–70 keV
	– GSO	40–600 keV
	Energy Resolution (PIN)	$\sim$ 4.0 keV (FWHM)
	Energy Resolution (GSO)	$7.6/\sqrt{E_{\rm MeV}}$ % (FWHM)
	Effective Area	$\sim$ 160 cm^2 at 20 keV, $\sim$ 260 cm^2 at 100 keV
	Time Resolution	61 μs

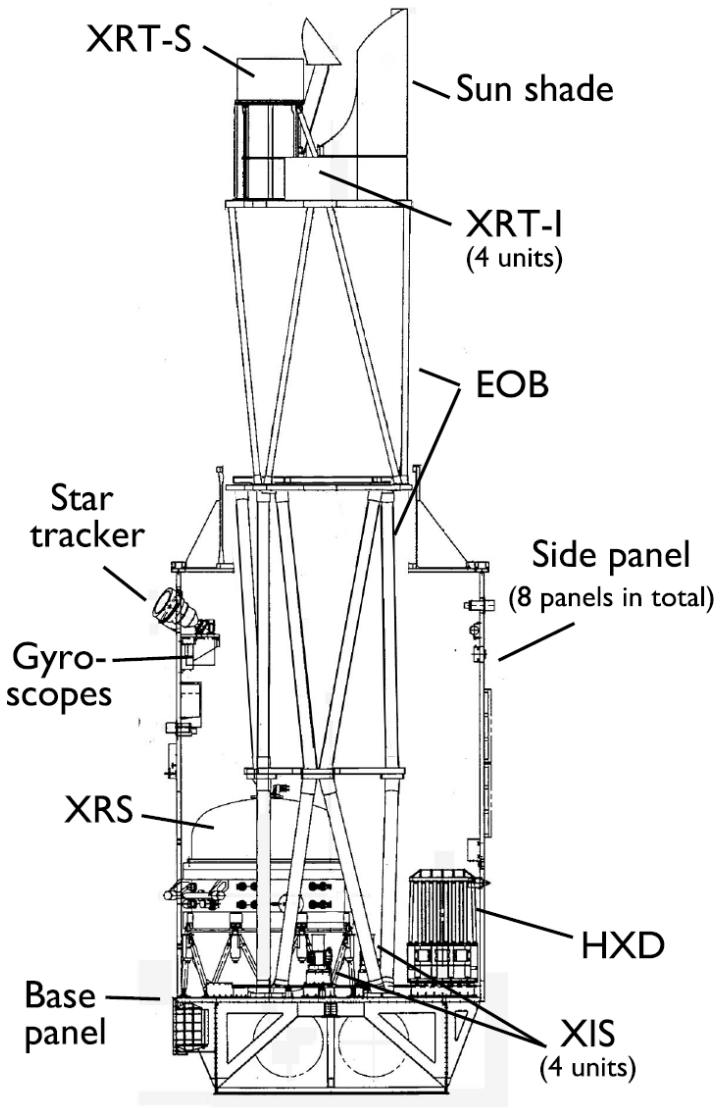

Figure 3.2: Side view of Suzaku with the optical bench extended showing the internal structures.

angular response has a sharp cusp. Thus the resolving power of two adjacent point sources is better than that expected from the face value of the angular resolution.

We show in figure 3.4 the total effective area of Suzaku (sum of 4 sets of XRT and XIS) in comparison with those of other currently working satellites. As seen in the figure, the effective area of Suzaku is much larger than that of Chandra and is comparable to XMM-Newton above $\sim$ 5 keV.

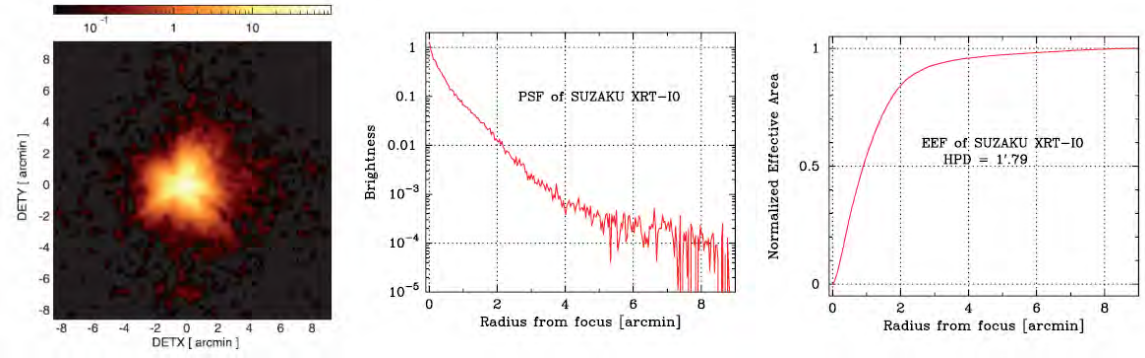

Figure 3.3: Image, Point-Spread Function (PSF), and Encircled-Energy Function (EFF) of XRT-I0 in the focal plane. Figures are adapted from Serlemitsos et al. (2007)

3.2.2 XIS

Suzaku is equipped with four X-ray Imaging Spectrometers (XISs) located at the focal plane of the telescope. An XIS employs an X-ray sensitive silicon charge-coupled device (CCD), which is operated in a photon-counting mode. A picture of XIS (CCD + camera body) is shown in figure 3.6. The four Suzaku XISs are named XIS0, 1, 2 and 3. One of the XISs, XIS1, uses a back-side illuminated (BI) CCD, while the other three use front-side illuminated (FI) CCDs. The BI CCD has superior quantum efficiency (QE) at lower energies, below $\sim$1 keV, because there is no gate structures at the back surface, through which the X-rays enter. However, the QE at higher energies is limited because of the relatively thin depletion layer. We show QEs for both the FI and BI CCDs as a function of the incident X-ray energy in figure 3.7. XIS exhibits moderate energy resolution of $\sim$130 eV (FWHM) at 5.9 keV. In addition, the non-X-ray background (NXB), which is induced by charged particles, is low compared with other missions as shown in figure 3.8. Each XIS sensor has ^{55}Fe calibration sources to illuminate the two far-end corners from the read-out node. XIS2 showed anomaly on Nov 9, 2006, and were not used for scientific observations since then.

XIS has large flexibility to clock the CCD. In the normal clocking mode, which is used most often, the whole imaging area are read out regularly every 8 sec. This

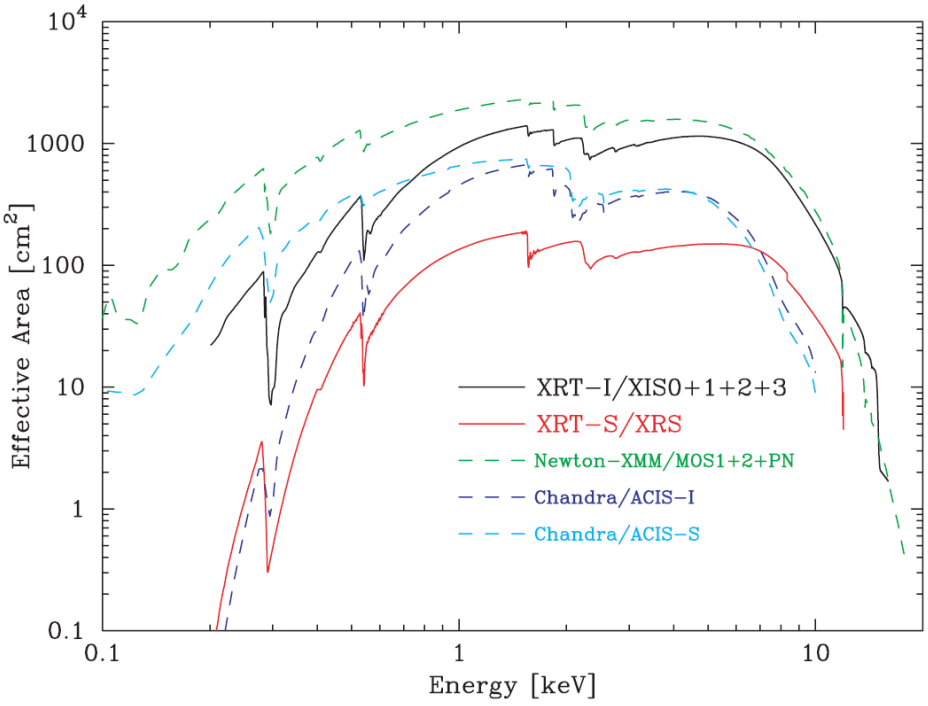

Figure 3.4: Total effective area of the four XRT-I modules compared with that of XMM-Newton and Chandra. Adapted from Serlemitsos et al. (2007)

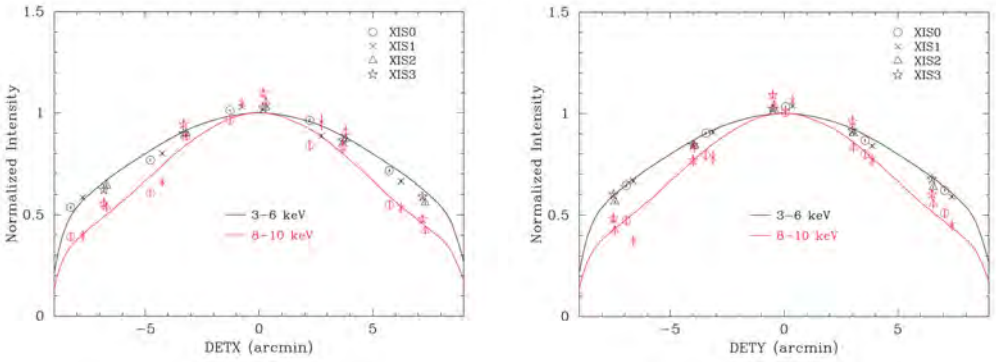

Figure 3.5: Vignetting of the four XRT-I modules deduced from the observations of the Crab Nebula with various offsets. The model curves were calculated using the ray-tracing simulator.Adapted from Serlemitsos et al. (2007)

means that the exposure time (and time resolution) is 8 sec. When observing a bright point source, an 8 sec exposure may be too long and could cause significant photon pile-up. This situation is mitigated by using an window option; a small region, called a window, is read out frequently when this option is applied. Two types of window options are available: 1/4 window and 1/8 window option. In the 1/4 window option, a 1/4 area (256×1024 pixels) of the CCD is read out every 2 sec. The area is further reduced to 128×1024 pixels in the 1/8 window option, but the time resolution (i.e. exposure time) is reduced to 1 sec. In some cases, a whole CCD area (1024×1024 pixels) is necessary, while the photon pile-up could be a problem. A burst option is used under such a situation. When a burst option is applied, a dummy exposure is inserted in the 8 sec interval. For example, when a dummy exposure of 7 sec is inserted, an effective exposure is reduced to 1 sec. The burst option is used for bright, extended sources. The burst and window options can be applied simultaneously. This is especially useful when the source is so bright that the window option is not enough to prevent the photon pile-up.

Because an X-ray CCD is sensitive to the radiation damage, its performance gradually degrades in the space environment. In the case of XIS, the effect appeared most clearly in the decrease of the charge transfer efficiency. A charge packet produced by the photo-electric absorption of an X-ray photon can not be transfered completely to the read-out gate. Some electrons are lost in the charge traps during the transfer, which corresponds to the defects in the lattice produced by the bombardment of the high energy particles. Because the electrons are lost stochastically, decrease of the charge transfer efficiency increases the uncertainty of the original number of electrons. This means that the energy resolution is degraded.

In order to reduce the effect of the radiation damage, the so-called charge injection method was adopted in the operation of XIS since September 2006. In this method, artificial charge is injected every 54 rows. The charge works to fill the traps produced by the radiation damage. Even if a trap is filled with an electron, the electron will be released spontaneously due to the thermal excitation. Thus the traps need to be filled frequently. This is the reason we inject charge every 54 rows. It turned out that the charge injection was very effective. XIS almost recovered the original performance just after the launch. Therefore, basically all the observations were done using the charge injection since late 2006.

Although XIS was operated successfully for more than a year, one of the XIS, XIS2, suddenly showed anomaly. Nearly a half of the CCD chip was flooded with extra charge and could not be used for the detection of X-ray photons. Although the origin of the anomaly is not known, impact of micro-meteoride is suspected. Since November 2006, XIS2 is not used for scientific observations.

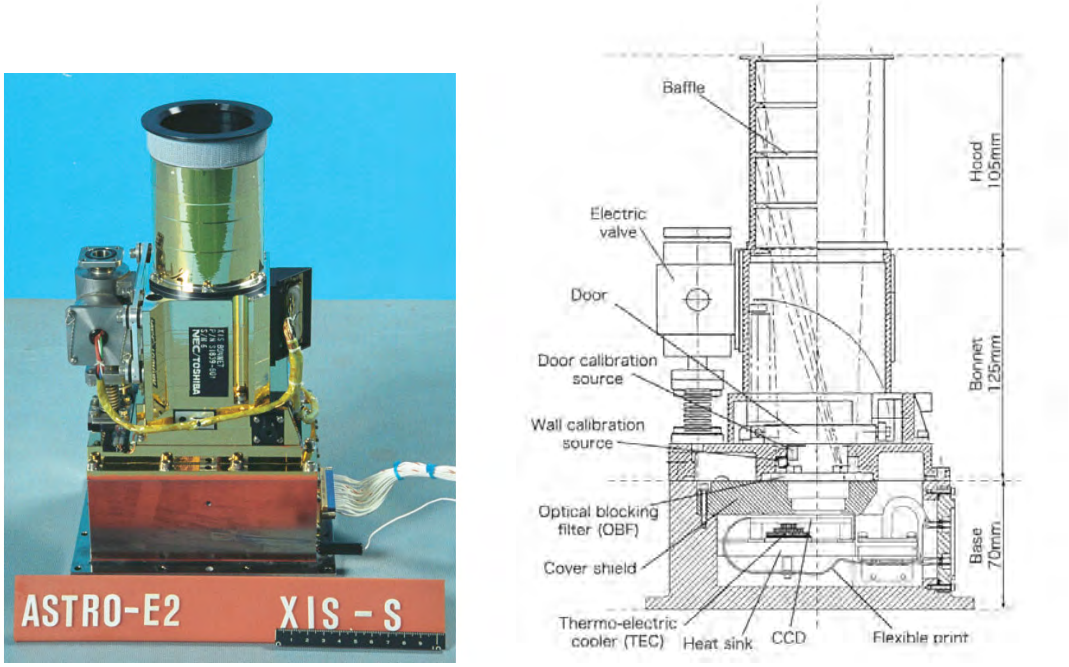

Figure 3.6: Left: A picture of the XIS sensor. Right: Cross section of the XIS sensor.

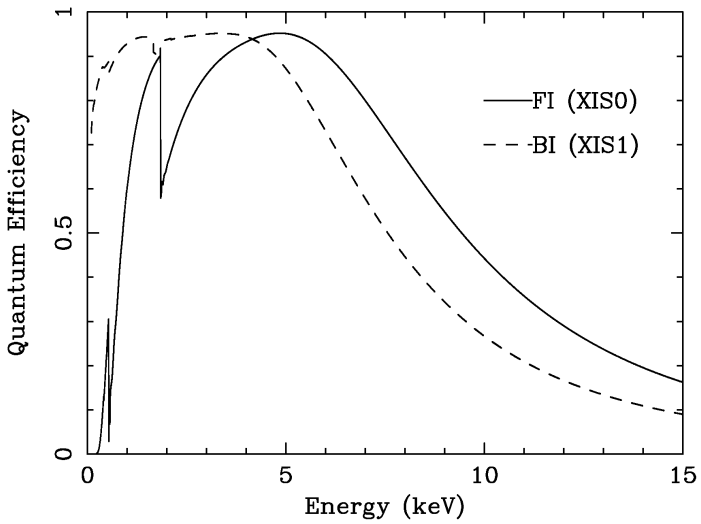

Figure 3.7: The QE as a function of incident energy. The solid line represents the FI CCD (XIS 0) and the broken line is for the BI CCD (XIS 1). Adapted from Koyama et al. (2007)

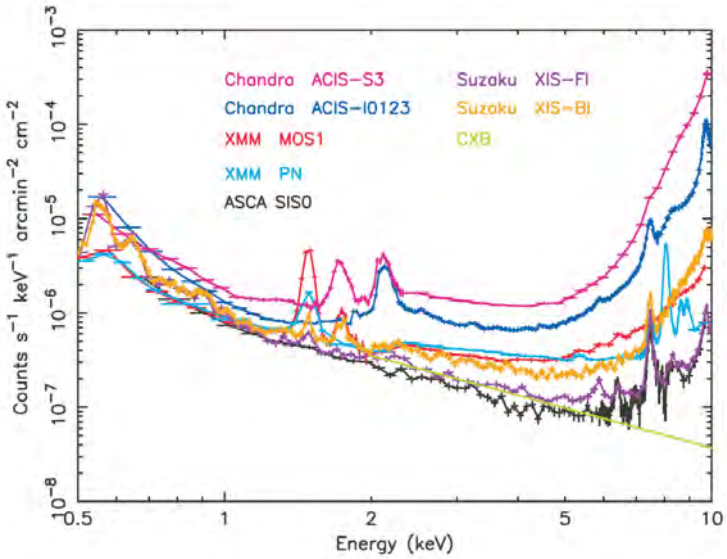

Figure 3.8: XIS background counting rate as a function of energy. The background rate was normalized with the effective area and the field of view. Background spectra of ASCA, Chandra, and XMM-Newton are shown for comparison. Adapted from Mitsuda et al. (2007)

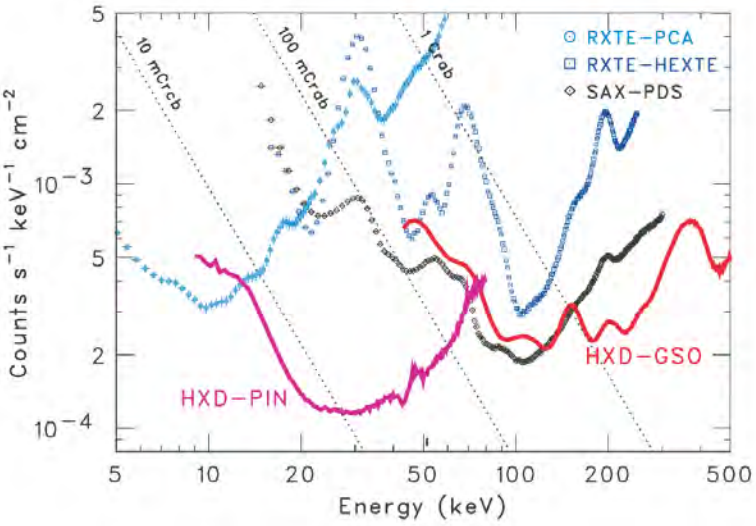

Figure 3.9: HXD background counting rate as a function of energy. The background rate was normalized with the effective area. Background spectra of RXTE and Beppo-SAX are shown for comparison. The intensity of the Crab nebula is also shown. This figure was taken from Mitsuda et al. (2007).

3.2.3 HXD

HXD is a compound-eye detector instrument consisting of 16 main detectors (arranged as a 4×4 array) and the surrounding 20 crystal scintillators for active shielding. Each unit actually consists of two types of detectors: a GSO/BGO phoswich counter, and 2 mm-thick PIN silicon diodes located inside the well, but in front of the GSO scintillator. Relatively soft X-rays are detected by the PIN diodes, which covers ∼10–70 keV, whereas harder X-rays go through the diodes and are detected by the GSO crystal, which locates just beneath the PIN diodes and covers ∼40–600 keV. A schematic view of HXD is shown in figure 3.10 and the characteristics of the HXD are summarized in table 3.2.

The field of view of HXD is restricted by two types of collimators. One is the well-structure made by the BGO scintillator. This restricts the HXD field of view to 4.5 deg in full-width at half maximum (FWHM). The other is the fine collimator installed inside the BGO well structure. It is made of thin phosphor bronze sheet to form 300 mm length, 3 mm width square collimator arranged in 8×8 array. The fine collimator restricts the field of view to 34 arcmin, but works only below ∼100 keV; it becomes more or less transparent above ∼100 keV. Thus the transmission of the HXD (as a function of the offset angle of the source) is energy dependent above ∼100 keV.

HXD is designed to achieve a very low detector background, and hence very high sensitibity. This is realized by the effective usage of the active shield in 3 stages. The 1st stage is a well structure of the unit counter. The X-ray sensitive parts, PIN diode and GSO scintillator, are installed in the bottom of the deep well structure, which can shield the background particles efficiently. The 2nd stage is the 4×4 configuration of the unit counters. Thus each unit can also work as an active shield of adjacent units. The last shield is the tightly arranged thick active shield surrounding the 4×4 counters. Thanks to these active shields, HXD achieved the lowest detector background so far in energy ranges of 15–70 and 150–500 keV. Detector backgrounds of selected satellites (including HXD) are compared in figure 3.9.

Because HXD is a non-imaging detector, no simultaneous background can be obtained during the observation of the target. Thus it is crucial to estimate and to subtract the background as accurate as possible to achieve the high sensitivity. In the case of HXD, a model background calculated based on the satellite orbit, attitude, monitor data, etc, is supplied from the hardware team. Although details of the model is found in Fukazawa et al. (2009), a brief summary is given below. The detector background of HXD consist of 2-types of components. One is the prompt secondary radiation caused by interactions between cosmic-ray particles and the spacecraft. Because the particle flux is mostly determined by the geomagnetic cutoff rigidity, this component is primarily determined by the satellite's orbit. The other is the delayed emissions from radio-active isotopes induced inside the detector mainly by SAA pro-

tons via nuclear interactions. This component is primarily determined by the fluence of protons in the SAA and shows strong time dependence; the longest time constant involved may be a few hundreds days. Thus the background of this component gradually evolves after the launch of the satellite and saturates within a year or so. These two components can be modeled empirically with appropriate parameters (orbit, attitude, monitor data, etc.). Current systematic error of the model background is ∼3% and ∼1% for PIN and GSO, respectively, for the observations longer than 10 ks.

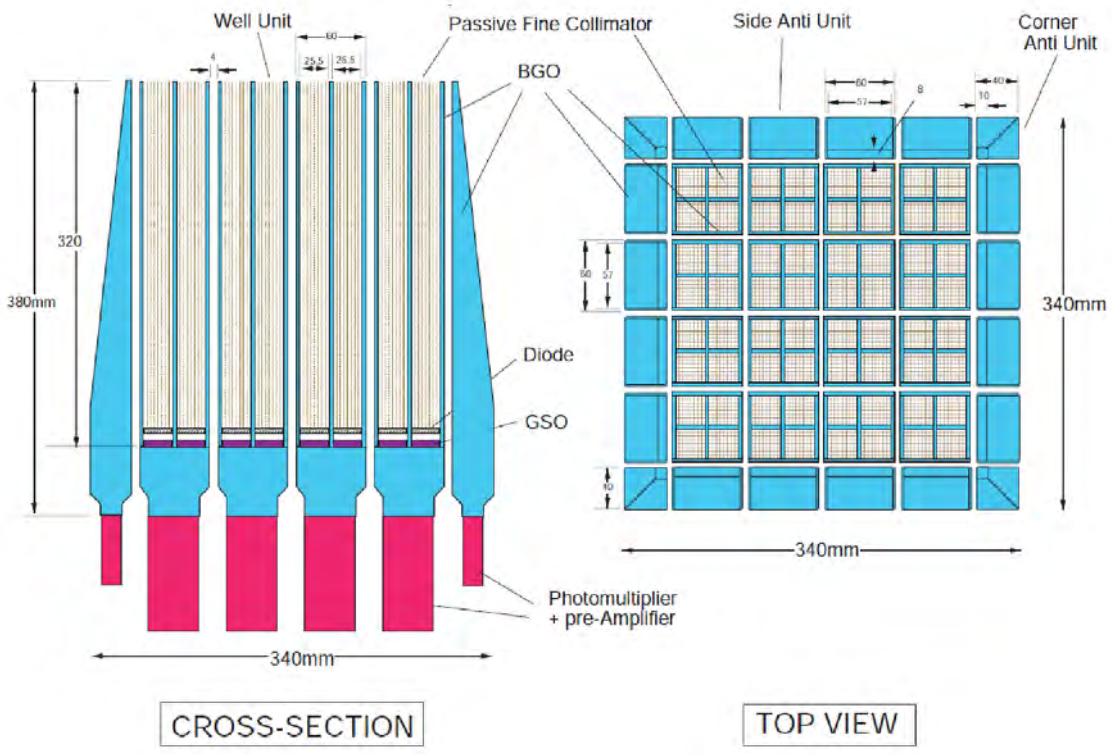

Figure 3.10: Schematic view of HXD.

3.3 Chandra

Chandra X-ray Observatory (CXO) was launched on July 23, 1999. The Chandra orbit is highly elliptical and varies with time. As of December 2007 the apogee height was ∼126,800 km and the perigee height was ∼22,000 km. Schematic view of Chandra on orbit is shown in figure 3.1. The Chandra X-ray Observatory combines the mirrors with four science instruments to capture and probe the X-rays from astronomical sources. The incoming X-rays are focused by the mirrors (HRMA: High Resolution Mirror Assembly) to a tiny spot on the focal plane. The focal plane science

instruments, ACIS and HRC, are well matched to capture the sharp images formed by the mirrors and to provide information about the incoming X-rays: their number, position, energy and time of arrival. Two additional science instruments provide detailed information about the X-ray energy, the LETG and HETG spectrometers. These are grating arrays which can be flipped into the path of the X-rays just behind the mirrors, where they redirect (diffract) the X-rays according to their energy. The X-ray position is measured by HRC or ACIS, so that the exact energy can be determined. The science instruments have complementary capabilities to record and analyze X-ray images of celestial objects and probe their physical conditions with unprecedented accuracy.

Here we only introduce the HRMA, ACIS and HRC, which are on the focal plane of the telescope because we do not use other two instruments. We summarize the characteristics of these instruments in table 3.3.

3.3.1 HRMA

The Chandra X-ray telescope consists of 4 pairs of concentric thin-walled, grazing-incidence Wolter Type-I mirrors called the High Resolution Mirror Assembly (HRMA). The front mirror of each pair is a paraboloid and the back a hyperboloid. The eight mirrors were fabricated from Zerodur glass, polished, and coated with iridium on a binding layer of chromium. The schematic view of HRMA is shown in figure 3.11.

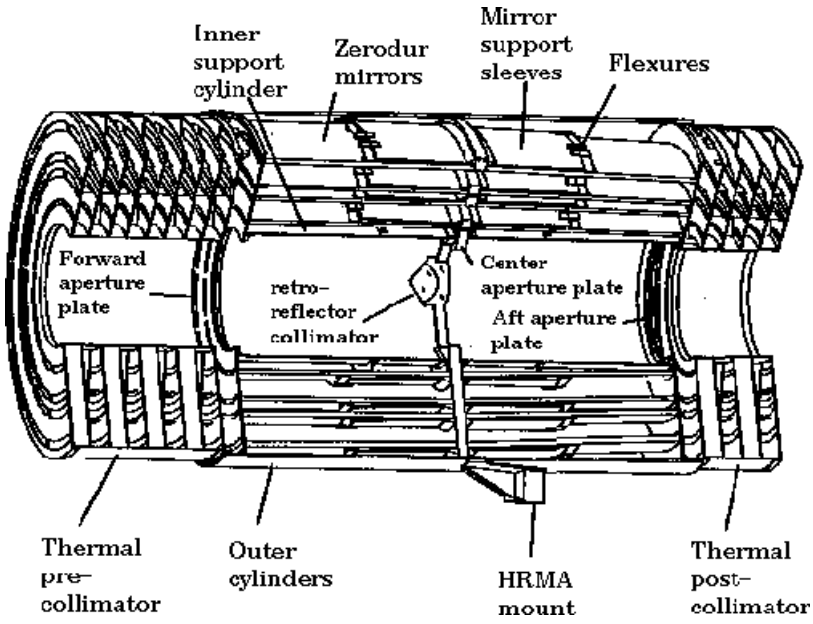

Figure 3.11: The schematic view of HRMA.

Table 3.3: Overview of Chandra capabilities

HRMA	Focal Length	$\sim$10 m
	Field of View	$30'$
	Geometrical Area	1145 cm^2
	Weight	1484 kg
	Effective Area	800 cm^2 at 0.25 keV
		400 cm^2 at 5.0 keV
		100 cm^2 at 8.0 keV
	Angular Resolution	$0''.5$ (HPD)
ACIS	Field of View	$16'.9 \times 16'.9$ (ACIS-I)
		$8'.3 \times 50'.6$ (ACIS-S)
	Bandpass	0.1–10 keV
	Number of Pixels/CCD	1024×1024
	Pixel Size	24 μm $\times$ 24 μm
	Energy Resolution	$\sim$ 2 % at 6 keV
	Effective Area	110 cm^2 at 0.5 keV (FI)
		600 cm^2 at 1.5 keV (FI)
		40 cm^2 at 8.0 keV (FI)
	Time Resolution	3.2 s (full frame)
HRC	Field of View	$30' \times 30'$ (HRC-I)
		$6' \times 99'$ (HRC-S)
	Bandpass	0.08–10.0 keV
	Energy Resolution	$\sim$ 1 keV at 1 keV
	Effective Area	133 cm^2 at 0.277 keV (HRC-I)
		227 cm^2 at 1 keV (HRC-I)
	Time Resolution	16 μs

3.3.2 ACIS

The Chandra Advanced CCD Imaging Spectrometer (ACIS) is one of two focal plane instruments. ACIS is comprised of two CCD arrays, a 4-chip array, ACIS-I; and a 6-chip array, ACIS-S. The CCDs are flat, but the chips in each array are positioned (tilted) to approximate the relevant focal surface: that of the HRMA for ACIS-I and that of the HETG Rowland circle for ACIS-S. ACIS-I was designed for CCD imaging and spectrometry; ACIS-S can be used both for CCD imaging spectrometry and also for high-resolution spectroscopy in conjunction with the HETG grating.

There are two types of CCD chips. ACIS-I is comprised of front-illuminated (FI) CCDs. ACIS-S is comprised of 4 FI and 2 back-illuminated (BI) CCDs, one of which is at the best focus position. The efficiency of the ACIS instrument has been discovered to be slowly changing with time, most likely as a result of molecular contamination build-up on the optical blocking filter. The BI CCDs response extends to lower energies than the FI CCDs and the energy resolution is mostly independent of position. The low-energy response of the BI CCDs is partially compromised by the contaminant build-up. The FI CCD response is more efficient at higher energies but the energy resolution varies with position due to radiation damage caused by protons reflecting through the telescope during radiation-zone passages in the early part of the mission. The schematic layout of ACIS is shown in figure 3.12.

The spacial resolution for on-axis imaging with ACIS is limited by the physical size of the CCD pixels (24.0 μm $\sim 0''.492$) and not by the HRMA. This limitation applies regardless of whether the aimpoint is selected to be the nominal aimpoint on I3 or S3. Approximately 90% of hte encircled energy lands within 4 pixels ($2''$) of the center pixel at 1.49 keV and within 5 pixels ($2''.5$) at 6.4 keV. As the offset from the aimpoint becomes larger, the PSF radius becomes larger.

The ACIS FI CCDs originally approached the theoretical limit of the energy resolution at almost all energies, while the BI CCDs exhibited a poorer resolution.

3.3.3 HRC

The High Resolution Camera (HRC) is also used at the focus of Chandra, where it detects X-rays reflected from an assembly of eight mirrors. The primary components of the (HRC) are two Micro-Channel Plates (MCP). The unique capabilities of the HRC stem from the close match of its imaging capability to the focusing power of the mirrors. When used with the Chandra mirrors, the HRC can make images that reveal detail as small as $0''.5$. The schematic layout of HRC is shown in figure 3.12.

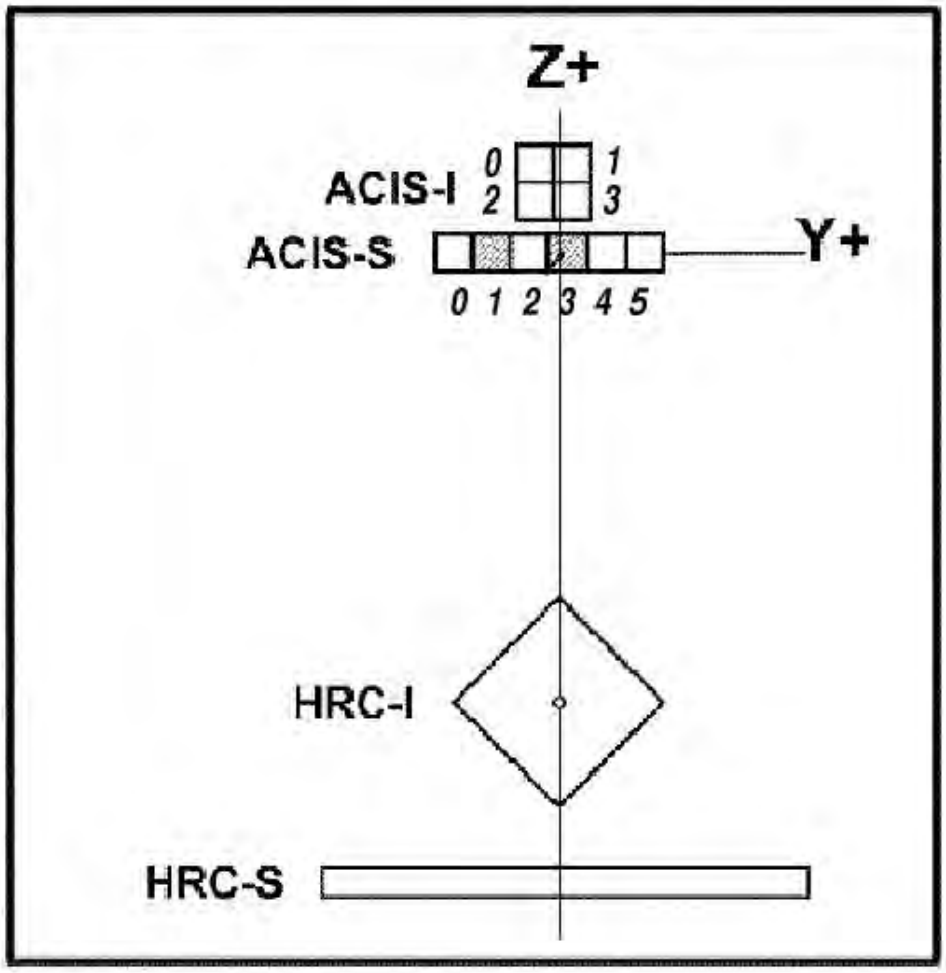

Figure 3.12: Arrangement of the ACIS and the HRC in the focal plane. The view is along the axis of the telescope from the direction of the mirrors. For reference, the two back-illuminated ACIS-S chips are shaded. Numbers indicate positions of chips I0-I3 and S0-S5. The aimpoint can be placed at any point on the vertical solid line.

3.4 XMM-Newton

The name of XMM-Newton stems from the design of its mirrors, a masterpiece of engineering, the highly nested X-ray Multiple Mirrors. XMM-Newton was launched on December 10th, 1999. It carries three very advanced X-ray telescopes. They each contain 58 high-precision concentric mirrors, delicately nested to offer the largest collecting area possible to catch the elusive X-rays. The XMM-Newton spacecraft is carrying a set of three X-ray CCD cameras, comprising the European Photon Imaging Camera (EPIC). Two of the cameras are MOS (Metal Oxide Semi-conductor) CCD arrays (referred to as the MOS cameras). They are installed behind the X-ray telescopes that are equipped with the gratings of the Reflection Grating Spectrometers (RGS). The gratings divert about half of the telescope incident flux towards the RGS detectors such that (taking structural obscuration into account) about 44% of the original incoming flux reaches the MOS cameras. The third X-ray telescope has an unobstructed beam; the EPIC instrument at the focus of this telescope uses pn CCDs and is referred to as the pn camera.

Schematic view of XMM-Newton on orbit is shown in figure 3.1. Here we introduce only EPIC on the focal plane of X-ray Telescopes because we do not use other instruments. We summarize the characteristics of these instruments in table 3.4.

3.4.1 X-ray Telescopes

Each of the three X-ray telescopes on board XMM-Newton consists of 58 Wolter I grazing-incidence mirrors which are nested in a coaxial and cofocal configuration. The design of the optics was driven by the requirement of obtaining the highest possible effective area over a wide range of energies, with particular emphasis in the region around 7 keV. Thus, the mirror system had to utilize a very shallow grazing angle of $30'$ in order to provide sufficient reflectivity at high energies. The telescopes focal length is 7.5 meters and the diameter of the largest mirrors is 70 cm, to be compatible with the shroud of the launcher. Each telescope includes, apart from the mirror modules, baffles for visible and X-ray stray-light suppression and an electron deflector for diverting soft electrons.

3.4.2 EPIC

The main focal plane instrument on XMM-Newton, providing imaging and spectroscopy, is the European Photon Imaging Camera (EPIC). Two of XMM-Newton's X-ray telescopes are equipped with EPIC MOS (Metal Oxide Semi-conductor) CCD arrays, the third carries a different CCD camera called EPIC pn.

The MOS chip arrays consist of 7 individual identical, front-illuminated chips.

Table 3.4: Overview of XMM-Newton capabilities

Telescopes	Focal Length	7.5 m
	Field of View	$30'$ diameter circle
	Geometrical Area/telescope	1145 cm^2
	Weight/telescope	520 kg
	Effective Area/telescope	1500 cm^2 at 2 keV
		900 cm^2 at 7 keV
		350 cm^2 at 10 keV
	Angular Resolution	$15''$ (HPD)
EPIC	Field of View	$30'$ diameter circle
	Bandpass	0.15–12 keV (MOS)
		0.15–15 keV (pn)
	Number of Pixels/CCD	600×600 (MOS)
		200×64 (pn)
	Pixel Size	40 μm $\times$ 40 μm (MOS)
		150 μm $\times$ 150 μm (pn)
	Energy Resolution	$\sim$ 2 % at 6.4 keV
	Effective Area	100 cm^2 (MOS), 500 cm^2 (pn) at 0.5 keV
		400 cm^2 (MOS), 1000 cm^2 (pn) at 1.5 keV
		100 cm^2 (MOS), 500 cm^2 (pn) at 8.0 keV
	Time Resolution	2.6 s (MOS; full frame)
		73.4 ms (pn; full frame)

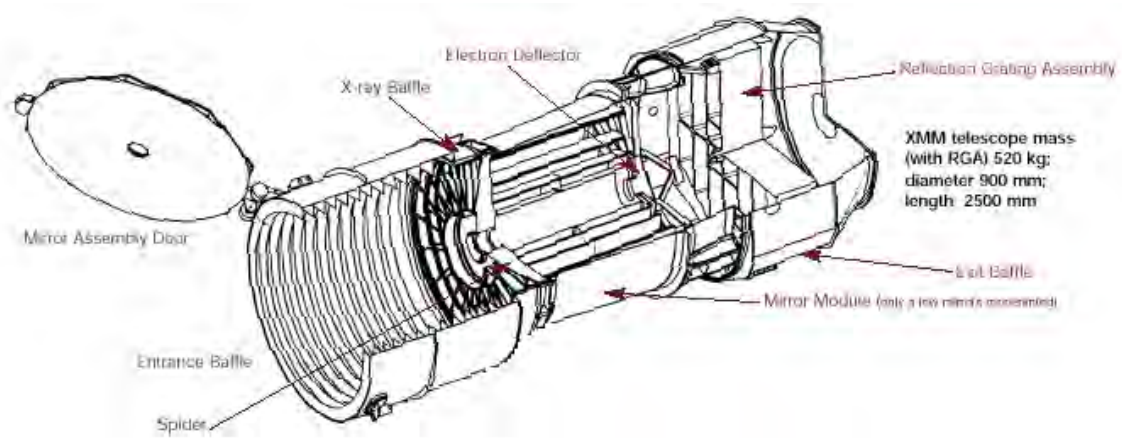

Figure 3.13: Scheme of one of the XMM-Newton Telescopes.

Each CCD is made up of a matrix of 600 × 600 pixels and reads out in a couple of seconds. The layout is shown in figure 3.14 and 3.15 (left). With only a 40-micron sensitive depth of silicon, the detectors are less responsive to hard X-rays.

The heart of the pn camera is a single Silicon wafer with 12 CCD chips integrated. Each pn-CCD has a 200 × 64 pixel matrix. The layout is shown in figure 3.14 and 3.15 (right). The fully depleted 280 μm of silicon determines the pn detector efficiency on the high energy end, while the quality of the radiation entrance window is responsible for the low energy response. As the pn-CCD is back-illuminated, which does not have insensitive layers or coatings, the X-ray detection efficiency is extremely high and homogeneous from the very low to the highest XMM-Newton energies (over 90% from 0.5 to 10 keV). The parallel readout of 768 independent channels enables the camera to be operated quickly: only 80 ms are needed to acquire one picture or frame. Special readout modes allow the observation of transient objects with a time resolution of only 40 ms.

The three EPIC cameras offer the possibility to perform extremely sensitive imaging observations over the telescope's field of view (FOV) of 30 arcmin (see figure 3.15) and in the energy range from 0.15 to 15 keV with moderate spectral ($E/\Delta E \sim 20-50$) and angular resolution (PSF, 6 arcsec FWHM).

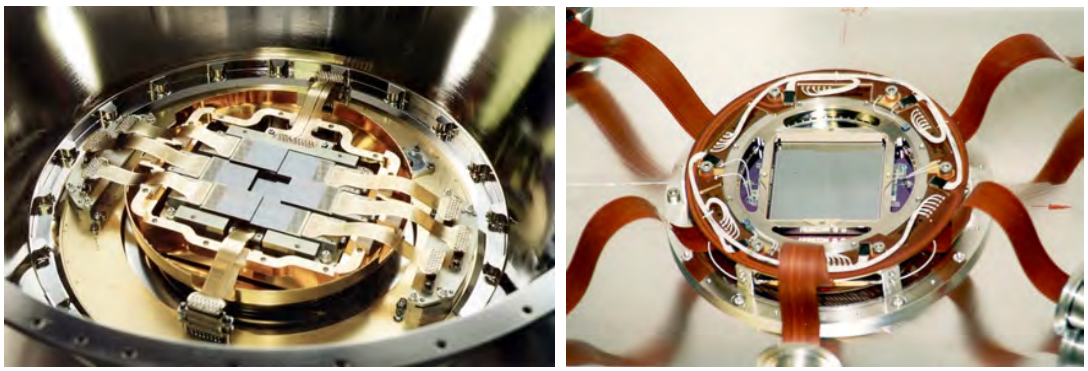

Figure 3.14: Pictures of the CCDs of one of the MOS cameras (left) and those of the pn camera (right).

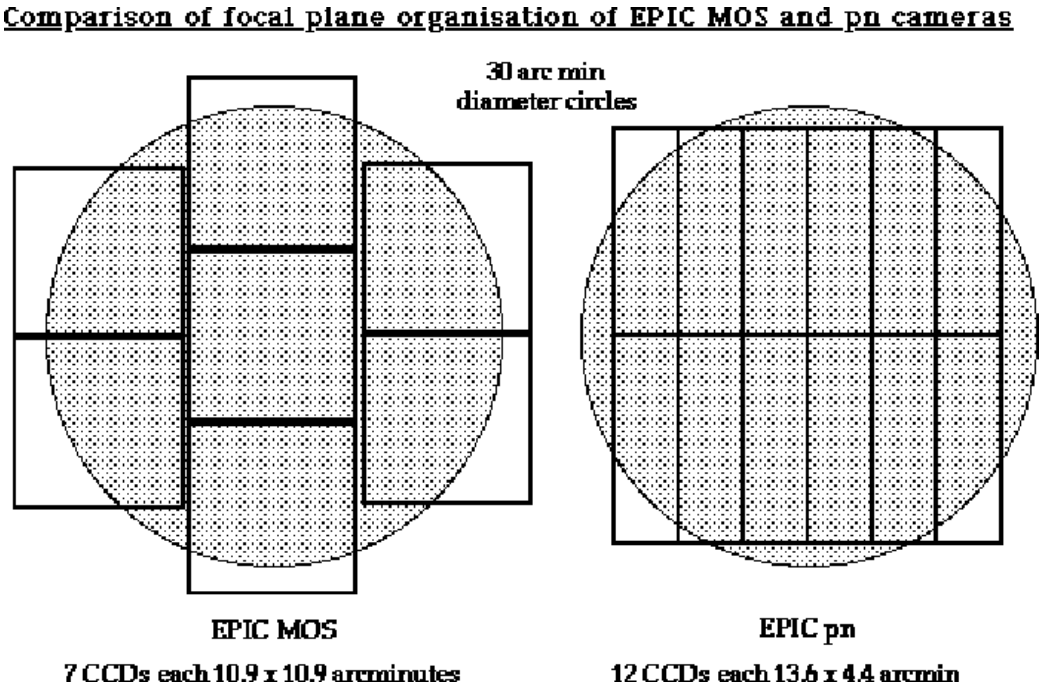

Figure 3.15: A sketch of the field of view of the two types of EPIC camera; MOS (left) and pn (right). The shaded circle depicts a $30'$ diameter area.

Chapter 4

Analysis & Results

HESS Galactic plane survey has revealed $\sim$40 unidentified VHE γ-ray sources (hereafter referred to as HESS sources). Origins of most of the sources are still unclear, but some of them were identified as PWNe (Gallant et al., 2008). It is suspected that major fraction of the unidentified sources may be in fact the PWNe. We have carried out two sets of new Suzaku observations of the unidentified HESS sources, HESS J1837–069 and HESS J1809–193. The former source was considered to be a VHE PWN candidate but the counterpart was unclear. We have also analyzed the X-ray data of the PWNe systematically, which are associated to the HESS sources, to quantify their common properties. For this purpose, we used archive data of various X-ray satellites in addition to the new Suzaku data.

When we analyzed the X-ray archive data, we focused on the morphology of the non-thermal X-ray emission, especially its extension. We compared the morphological information with that in the VHE γ-ray band, which was taken from the literature. We also made detailed analysis of the two sources, HESS J1837–069 and HESS J1809–193, with the new Suzaku (and archive) data. The analysis includes not only the morphological analysis but also the spectral and timing analysis.

Sections in this chapter are arranged as follows. We first describe the analysis and results of HESS J1837–069 and HESS J1809–193, of which we have the new Suzaku observations. We then describe the archival data analysis of other HESS detected PWNe. Each section is almost independent; previous observations, summary of the results, and discussion if appropriate, are given for each section. Finally, we mention the HESS detected PWNe that enough quality of X-ray archive data were not available.

4.1 HESS J1837–069

4.1.1 Previous Observations

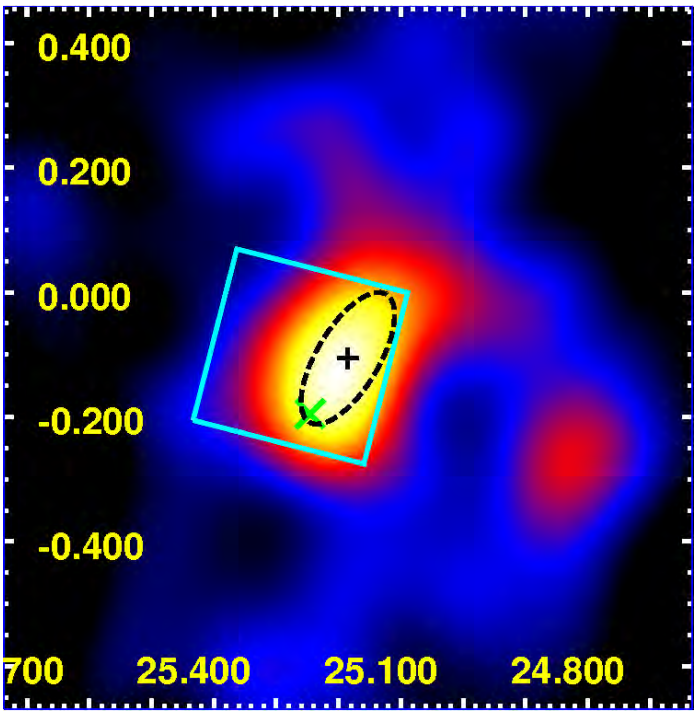

Figure 4.1: Smoothed excess map (smoothing radius 0°.05) measured by HESS in the sky field of HESS J1837–069[2]. The best fit position of the HESS source is marked with a black cross and the fit ellipse with a dashed line. Suzaku XIS field of view of this study is shown with cyan box. Green cross indicates the X-ray pulsar discovered by Gotthelf & Halpern (2008).

HESS J1837–069 is one of the VHE γ-ray sources discovered by the Galactic survey with HESS in 2004. HESS excess map is shown in figure 4.1. Assuming a two-dimensional Gaussian brightness profile, the best fit position of the center of the excess was determined as (RA, Dec) = ($18^{\rm h}37^{\rm m}42^{\rm s}.7$, $-06°55'39''$). It has a significantly elongated shape with an extension of $7'.2 \pm 1'.2$ for the major axis and $3'.0 \pm 1'.2$ for the minor axis, respectively. The spectrum was fit with a power-law function with a photon index of $\Gamma = 2.27 \pm 0.06_{\rm stat} \pm 0.2_{\rm sys}$. The flux in the 1–10 TeV band was $(1.4 \pm 0.4) \times 10^{-11}$ ergs cm^{-2} s^{-1} (Aharonian et al., 2005a, 2006a).

No X-ray sources are known to be positionally coincident to the center of HESS J1837–069, although AX J1838.0–0655, which is located on the edge of the HESS source, was suggested to be a possible counterpart (Gotthelf & Halpern, 2008). ASCA observation revealed that AX J1838.0–0655 had a very hard and strongly absorbed

spectrum (Bamba et al., 2003a). INTEGRAL (Malizia et al., 2005) observations also supported this result. Recently, Gotthelf & Halpern (2008) discovered a 70.5 ms pulsation with RXTE in the sky field including AX J1838.0–0655, and also resolved a bright point source surrounded by diffuse emission with Chandra. They concluded that AX J1838.0–0655 is a PWN.

4.1.2 Observations

We observed HESS J1837–069 with Suzaku in March, 2007. The observation was carried out with the HXD optical axis (which is $\sim 3'$ offset of that of XIS) placed at the center of HESS J1837–069 in order to optimize the HXD throughput. Three XISs (XIS 0, 1, 3) were operated in the normal clocking mode with Spaced-row Charge Injection (SCI) (Nakajima et al., 2008). We analyzed the data prepared by the version 2.0 pipeline. We applied the standard screening criteria to both the XIS[3] and HXD[4] data to obtain cleaned event lists. After the data screening, the net exposures were 42.2 ks and 37.7 ks for XIS and HXD, respectively.

We also used the ASCA archival data of this region, that were previously published by Bamba et al. (2003a). HESS J1837–069 was in the FOV of ASCA GIS in both the 1997 and 1999 observations (Bamba et al., 2003a). The data was screened based on the same criteria as Bamba et al. (2003a). We used HEADAS version 6.3.1 software package for the data analysis of HESS J1837–069.

In addition, we analyzed the Chandra archival data for the morphological analysis in §4.1.3. We used the standard processed and filtered event data. Data reduction and analysis was performed using CIAO (ver. 4.0).

The net exposures after screening are summarized in table 4.1 with the journal of ASCA, Suzaku and Chandra observations.

4.1.3 Analysis & Results

X-ray Image

We extracted the XIS image in 0.4–10.0 keV for each sensor. The data between 5.73–6.67 keV were removed from the image to exclude the calibration sources. We corrected the vignetting effect by dividing the image with the flat sky image simulated at 4.0 keV using the XRT+XIS simulator `xissim` (Ishisaki et al., 2007). The image was binned to 8×8 pixels and smoothed with a Gaussian function of $\sigma = 0'.21$. Combined Suzaku XIS (0+1+3) image is shown in figure 4.2. Yellow cross on this image indicates a centroid of VHE γ-ray emission determined by fitting. The length

[2]Fits file is available from http://www.mpi-hd.mpg.de/hfm/HESS/public/publications/ApJ_636.html
[3]http://www.astro.isas.jaxa.jp/suzaku/process/v2changes/criteria_xis.html
[4]http://www.astro.isas.jaxa.jp/suzaku/process/v2changes/criteria_hxd.html

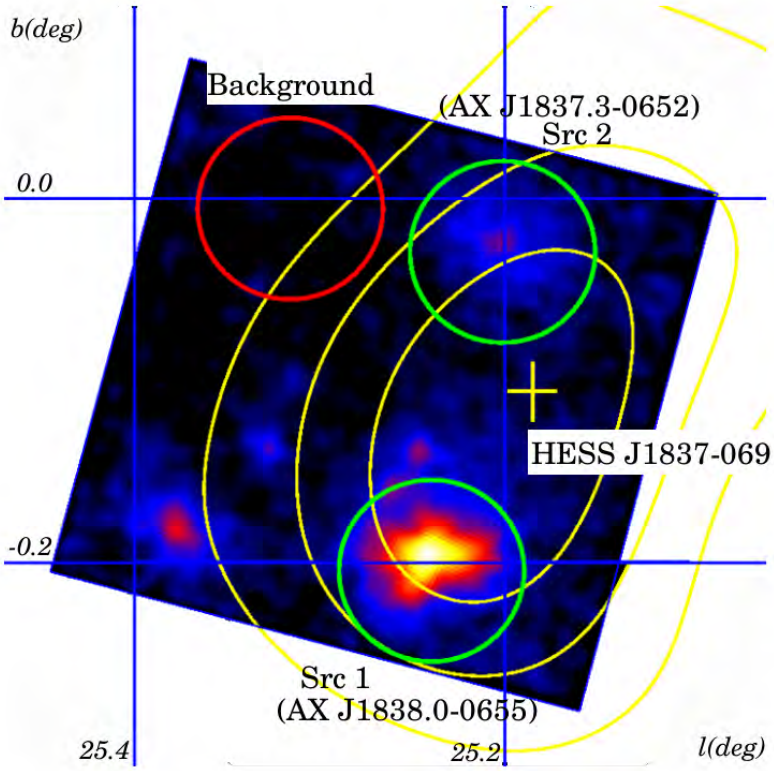

Figure 4.2: Suzaku XIS (0+1+3) image in Galactic coordinate around HESS J1837–069 in the 0.4-10.0 keV band. The data between 5.73–6.67 keV were filtered out to remove the calibration sources. The pseudo-color represents vignetting-corrected, log-scaled intensity levels. Yellow lines represent the 80%, 60%, and 40% contours to the peak of the VHE γ-ray image of HESS J1837–069, and yellow cross indicates the centroid of the HESS source (Aharonian et al., 2006a). Two sources in the green circles are referred to Src 1 (AX J1838.0–0655) and Src 2 (AX J1837.3–0652). Background data were extracted from the red circle whose vignetting is almost the same as the two sources. All the radii of the circles are $3'$. 2E1835.5-0650 was also detected at the position of $(l, b) = (25°.38, -0°.18)$.

Table 4.1: Journal of the ASCA/Suzaku/Chandra observations of HESS J1837–069

Satellite	ASCA	ASCA	Suzaku	Chandra
Sequence ID	55002090	57029000	401026010	6719
Start time[1]	1997/10/14 09:12	1999/09/26 18:12	2007/03/05 12:49	2006/08/19 16:31
End time[1]	1997/10/14 14:17	1999/09/28 03:30	2007/03/06 10:17	2006/08/19 22:28
R.A. (J2000)	$18^{\rm h}37^{\rm m}48^{\rm s}.0$	$18^{\rm h}37^{\rm m}45^{\rm s}.6$	$18^{\rm h}37^{\rm m}42^{\rm s}.7$	$18^{\rm h}37^{\rm m}43^{\rm s}.0$
Decl. (J2000)	$-06^\circ36'42''$	$-06^\circ36'45''$	$-06^\circ55'39''$	$-06^\circ54'21''$
Net exposure (ks)	12.4[2] / 8.4[3]	37.3[2] / 17.6[3]	42.2[4] / 37.7[5]	19.9

[1] Time form of yyyy/mm/dd hh:mm (UT)
[2] GIS, high and medium bit-rate data
[3] GIS, high bit-rate data only
[4] XIS
[5] HXD-PIN

Table 4.2: Suzaku detected X-ray sources in the vicinity of HESS J1837–069

Src	coordinate[1] (J2000)		Association
	R.A.	Decl.	
1	$18^{\rm h}38^{\rm m}03^{\rm s}$	$-06^\circ55'43''$	AX J1838.0–0655
2	$18^{\rm h}37^{\rm m}21^{\rm s}$	$-06^\circ53'14''$	AX J1837.3–0652

[1] Error radius (90%) is $19''$ (Uchiyama et al., 2008a)

of the cross shows the fitting error including the systematic astrometric error of $20''$ of HESS. Two X-ray sources are seen in the extent of HESS J1837–069. Hereafter, we refer to the two sources as Src 1 and Src 2 as indicated in figure 4.2. We determined the peak positions of Src 1 and Src 2 as listed in table 4.2. These positions are consistent with those of the ASCA sources, AX J1838.0–0655 and AX J1837.3–0652, respectively. Locations of these two sources are significantly offset from the center of HESS J1837–069 ($6'.4$ for Src 1 and $5'.7$ for Src 2), although they are both spatially compatible with the reported extension of HESS J1837–069 (yellow regions in figure 4.2).

In order to determine the extension of non-thermal X-ray emission from Src 1, we created the XIS image in 2.0–7.0 keV for each sensor. Combined Suzaku XIS (0+1+3) image is shown in figure 4.3 (top). We created a surface brightness profile from the enclosed region shown in figure 4.3 (top) along the Galactic east to west direction. We fitted the profile with a Gaussian function plus constant ignoring the profile in the region with the radius of $1'$ from the brightest part of Src 1. This is to avoid the contribution from the bright pulsar, whose image is smeared by the point-spread-function of the telescope. Figure 4.3 (bottom) shows fitted profile. The surface brightness is normalized with the peak brightness. The best-fit Gaussian width is $\sigma = 1'.25 \pm 0'.05$.

Chandra archival data are also available around HESS J1837–069. We also analyzed the Chandra ACIS data to confirm the consistency of this analysis between Suzaku XIS and Chandra ACIS. Figure 4.4 (top) shows the exposure-corrected entire four-CCD ACIS-I field image in the 2.0–7.0 keV band. Pseudo-color shows the log-scaled intensity map smoothed with a Gaussian function of $\sigma = 5''$. A green cross in this image indicates the position of the point source in Src 1. In order to study the extension of the diffuse emission from Src 1, we removed point-like sources around Src 1 identified by the CIAO software package source detection tool `wavedetect`. We created the profile of the surface brightness distribution from the Chandra ACIS image. Figure 4.4 (bottom) shows the profile along the Galactic east to west direction extracted from the region indicated by the green box in figure 4.4 (top), which is the same in the sky coordinate as the one shown in figure 4.3 (top). We ignored bins near the pulsar for the fit with a Gaussian profile to see the extension of the diffuse emission. The best-fit Gaussian width is $\sigma = 1'.66 \pm 0'.34$.

The Gaussian width determined with Chandra ACIS is rather large compared with the width determined with Suzaku XIS. Because the point spread function of Suzaku XRT has a long tail, photons from the pulsar may be still included in the profile more than $1'$ away from the pulsar. Thus we may underestimate the extension of the diffuse emission. We consider the systematic error of the extension determined with Suzaku XIS as $0'.4$.

Energy Spectra

We extracted the Suzaku XIS energy spectra of Src 1 and Src 2 within the $3'$ circular regions centered on the sources to avoid nearby faint point source detected by Chandra, which enclose $\sim$90% of photons for each sources (green circles in figure 4.2). Background data were extracted from the source-free region as indicated by a red circle in figure 4.2, whose vignetting is almost same as that of Src 1 and Src 2. Figure 4.5 shows the XIS spectra (averaged for XIS 0, 1 and 3) of Src 1 and Src 2 in the 0.4–10 keV band. The 1.7–2.0 keV band was ignored from the analysis because of large calibration uncertainties around the Si edge[5]. We generated detector and auxiliary response files using `xisrmfgen` and `xissimarfgen` for each source (Ishisaki et al., 2007). We fitted the spectra with an absorbed power-law model using XSPEC version 12.3.1. The fit results are summarized in table 4.3.

We also reanalyzed the data obtained with ASCA GIS in 1997 and 1999 to determined the errors of the source fluxes, which are not published in Bamba et al. (2003a). We extracted the data of Src 1 and Src 2 in the 0.7–10 keV band from the same regions as Bamba et al. (2003a) and subtracted the background extracted from the source-free regions near the sources. We summed up the data in 1997 and 1999

[5]http://www.astro.isas.jaxa.jp/suzaku/doc/suzaku_td/

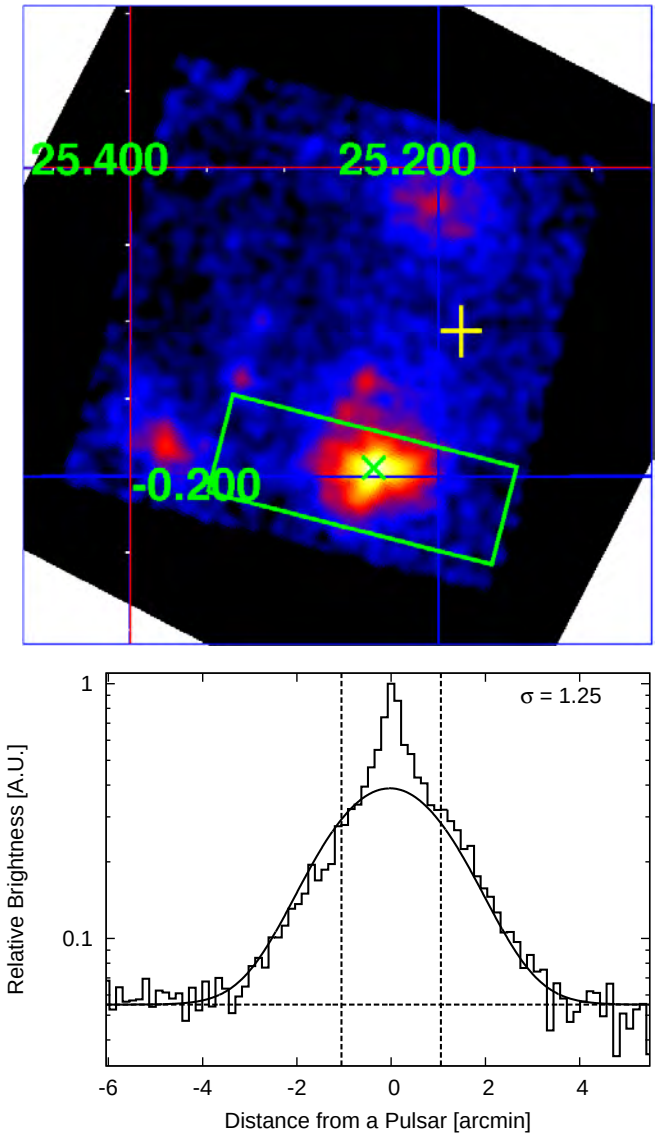

Figure 4.3: Top: Suzaku XIS image in Galactic coordinate around HESS J1837–069 in the 2.0–7.0 keV band. The pseudo-color represents vignetting-corrected, log-scaled intensity levels. Yellow and green crosses indicate the centroid of HESS J1837–069 and the brightest position of Src 1, respectively. Bottom: normalized 1-dimensional profile of the surface brightness obtained from the enclosed region with a green box in the top panel with a spatial bin size of $8''.4$. Solid curve and horizontal dashed line show the best-fit line of the Gaussian profile and a constant, respectively. Bright part near the pulsar was ignored in this fit ($2'$ across, inner part between the vertical dashed lines).

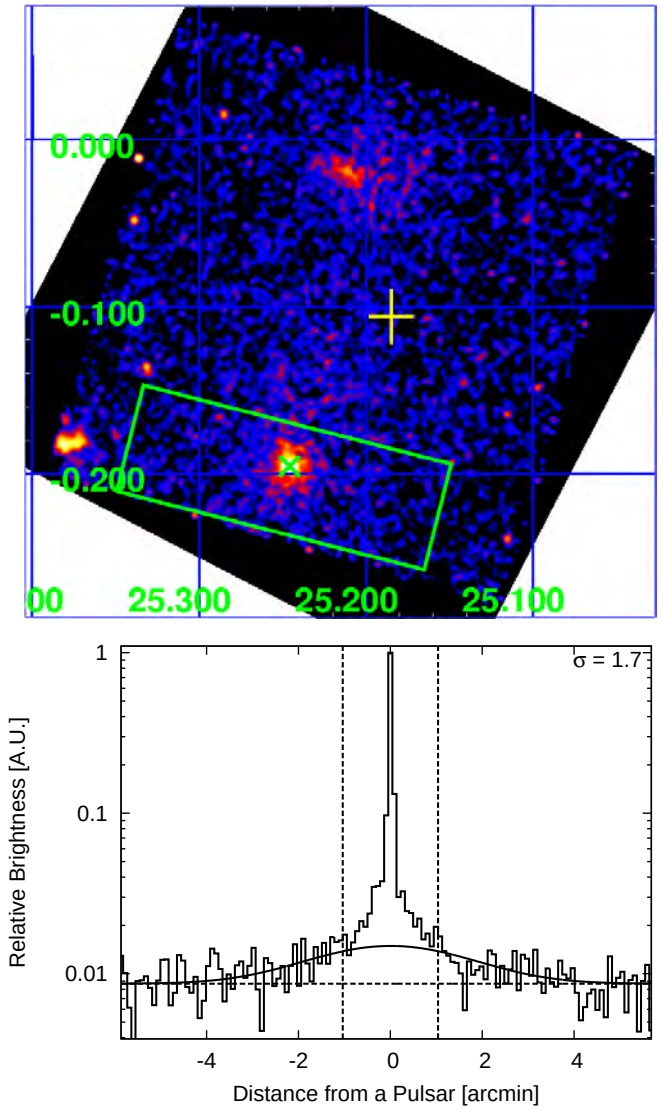

Figure 4.4: Top: Chandra ACIS-I image in Galactic coordinate around HESS J1837–069 in the 2.0–7.0 keV band. Point-like sources around AX J1838.0–0655 was removed and filled. The image was exposure-corrected and smoothed with a Gaussian function of $\sigma = 5''$. Yellow and green crosses indicate the centroid of HESS J1837–069 and the brightest position of Src 1, respectively. Bottom: normalized 1-dimensional profile of the surface brightness obtained from the enclosed region with a green box in the top panel with a spacial bin size of $5''.4$. Solid curve and horizontal dashed line show the best-fit Gaussian profile and a constant, respectively. Bright part near the pulsar was ignored in this fit ($2'$ across, inner part between the vertical dashed lines).

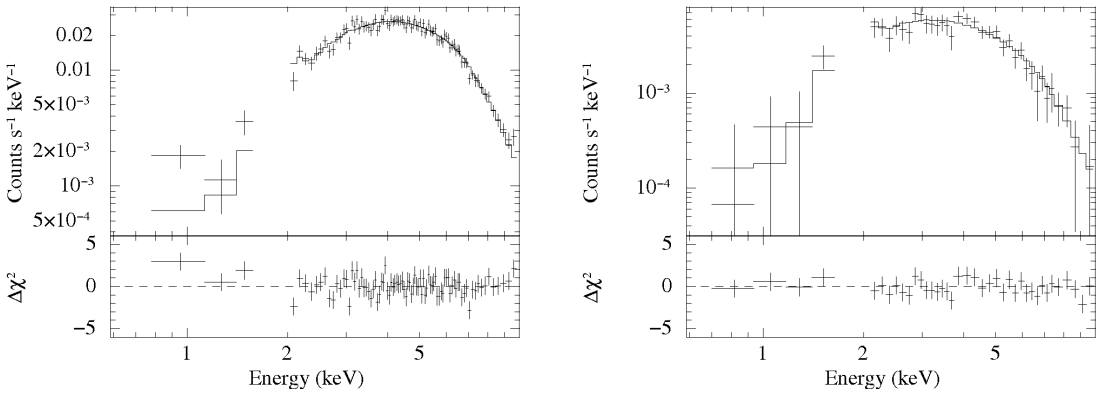

Figure 4.5: Background-subtracted XIS spectra of Src 1 (left) and Src 2 (right), respectively. Solid lines show the best-fit model. The bottom panels show residuals to the best-fit model.

Table 4.3: Best-fit parameters of the absorbed power-law model

Source	Instrument	Γ	$N_{\rm H}$[1]	Flux[2]	χ^2 / dof
1	Suzaku/XIS	1.27±0.11	5.4±0.5	$13.2^{+0.8}_{-0.6}$	97.7 / 86
	ASCA/GIS	0.8±0.4	$4.0^{+1.6}_{-1.3}$	14^{+2}_{-1}	12.9 / 12
2	Suzaku/XIS	$2.2^{+0.4}_{-0.3}$	$4.6^{+1.5}_{-1.0}$	$3.1^{+1.5}_{-0.7}$	27.1 / 37
	ASCA/GIS	$2.4^{+0.9}_{-0.8}$	$6.2^{+3.4}_{-2.2}$	6^{+13}_{-3}	35.6 / 33

Note. — Errors represent single-parameter 90% confidence limit.
[1] Absorption column density using the solar abundance ratio (Anders & Ebihara, 1982) in the unit of 10^{22} cm^{-2}.
[2] Unabsorbed flux in the 0.7–10.0 keV band in the unit of 10^{-12} ergs cm^{-2} s^{-1}.

to improve statistics as was done by Bamba et al. (2003a). We fitted the spectra with an absorbed power-law model and calculated the single-parameter 90% confidence regions of the unabsorbed fluxes. The results are listed in table 4.3.

Timing Analysis

Because X-ray pulsation was recently detected from the sky region including HESS J1837–069 (Gotthelf & Halpern, 2008), we carried out timing analysis of the data obtained by Suzaku HXD-PIN and ASCA GIS, which has high timing resolution, to study the long-term change of the pulse period and to identify the source of pulsation. Although HXD-PIN has a large FOV, there are no significant contamination sources to Src 1 in its FOV. Thus we searched for pulsation with HXD-PIN. When we analyzed the HXD-PIN data, we carefully determined the best energy range to maximize the signal-to-noise ratio. In order to minimize the contribution of non-X-

ray background (NXB)[6] , cosmic X-ray background (CXB) and Galactic ridge X-ray emission (GRXE), we selected 12–23 keV for the analysis of the PIN data. In this energy band, the source count rate was 0.41 counts s^{-1} whereas the count rates of NXB and CXB+GRXE were 0.32 and 0.04 counts s^{-1}, respectively. We then applied barycentric correction to the PIN data using `aebarycen` (Terada et al., 2008). Using the `efsearch` ftool, we searched for pulsation at 128 trial periods between 0.0704949–0.0704987 sec and found a significant peak at 0.07049672(8) s with $\chi^2 \sim 46$ (9 degrees of freedom). Here the 1σ error is indicated in parentheses, which was calculated according to Larsson (1996). The chance probability to obtain such a large χ^2 in 128 trial is only 0.01%.

Whereas HXD-PIN is a non-imaging instrument, GIS has an imaging capability and can extract the events from the source region. Assuming that the pulsation originates from Src 1, we searched for pulsation from the GIS data of Src 1. Although the nominal time resolution of GIS in the PH mode is 62.5 ms in the high telemetry bit rate (Ohashi et al., 1996), we can achieve higher time resolution up to 4 ms when the total count rate is low. The GIS event data were output to the fixed format telemetry, whose relative location within a 62.5 ms slot was designed to indicate the finer timing information[7]. The photon arrival time of GIS in the ASCA archive is all assigned taking this finer timing information into account. Because Src 1 (and other sources in the GIS FOV) is faint (2.3 counts s^{-1} compared to the telemetry capacity of 128 counts s^{-1}), we can fully utilize the higher than the nominal time resolution of GIS. The GIS image of Src 1 was elongated due to the proximity to the edge of the FOV. Thus we used an elliptical region of $1'.7 \times 0'.9$ to extract the source events. We used only the high bit rate data in 1999, and 224 photons in 2–10 keV (including background) was extracted in total. We applied barycentric correction using `timeconv`. We searched for pulsation at 128 trial periods between 0.0704838–0.0704865 sec and found a significant peak at 0.070485(2) sec with $\chi^2 \sim 38$ (9 degrees of freedom). The chance probability to obtain a χ^2 larger than 38 is only 0.2%. Thus the peak is statistically significant.

We show the folded pulse profiles of PIN and GIS in figure 4.6 with respective pulse periods determined above. Parameters determined by the timing analysis above are summarized in table 4.4. We divided the PIN data into two phases: on-peak (phase 0.65–1.05) and off-peak (phase 0.05-0.65). We extracted the pulsed spectrum by subtracting the off-peak spectrum from the on-peak spectrum, and fitted it with a power-law model in the 12–50 keV band. The fitted spectrum is shown in figure 4.7. Best-fit photon index and the flux in the 12–50 keV band were found to be $\Gamma = 2.0^{+1.0}_{-0.9}$

[6]We used the quick-version of the NXB model explained in SUZAKUMEMO-2008-03 (http://www.astro.isas.jaxa.jp/suzaku/doc/suzakumemo/suzakumemo-2008-03.pdf), and also in Fukazawa et al. (2009).

[7]http://heasarc.gsfc.nasa.gov/docs/asca/newsletters/time_assignment4.html

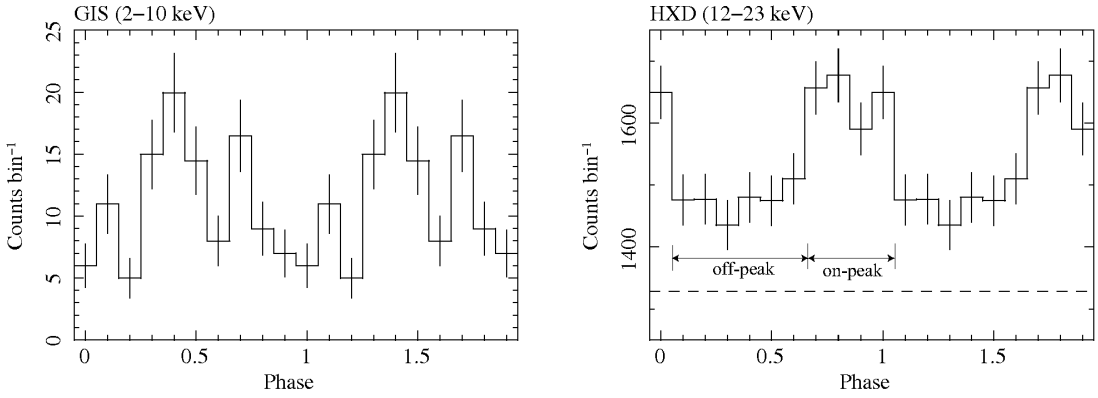

Figure 4.6: Left: Pulse profile obtained with the GIS data of Src 1 in the 2–10 keV band. Right: Pulse profile obtained with PIN in the 12–23 keV band. Dashed line indicates the estimated background level. The pulse profile is corrected for the constant dead time (93%).

Table 4.4: Timing Parameters of Src 1

Parameter	GIS	HXD-PIN
Epoch (MJD TDB)	51447	54164
Period, P (ms)	70.485(2)	70.49672(8)

Note. — 1σ uncertainties are given in parentheses.

and $F = 1.8^{+0.8}_{-0.6} \times 10^{-11}$ ergs cm^{-2} s^{-1}. We tried the same analysis for the GIS data, but could not obtain a meaningful result due to poor statistics.

4.1.4 Discussion

Nature of Src 1

We have confirmed that the source of 70.5 ms pulsation, which was recently discovered by RXTE, is indeed Src 1. The pulse profiles obtained by GIS and HXD-PIN are consistent with that of RXTE. We show in figure 4.8 a long-term history of the pulse period. All the data are consistent with the stable spin-down with $\dot{P} = 4.917(4) \times 10^{-14}$ s s^{-1} (1σ error is indicated in parentheses), which is also consistent with (and more precise than) the instantaneous spin-down rate determined by RXTE for the interval of $\sim$16 days (Gotthelf & Halpern, 2008). The pulse period and the period derivative indicate the spin-down luminosity of $\dot{E} = 5.5 \times 10^{36}$, characteristic age of $\tau = 23$ kyr and the surface magnetic field strength of $B_s = 1.9 \times 10^{19}$ G.

The spectral parameters (flux, photon index, column density) of Src 1 determined by the GIS data were all consistent with those of XIS. The flux and the column

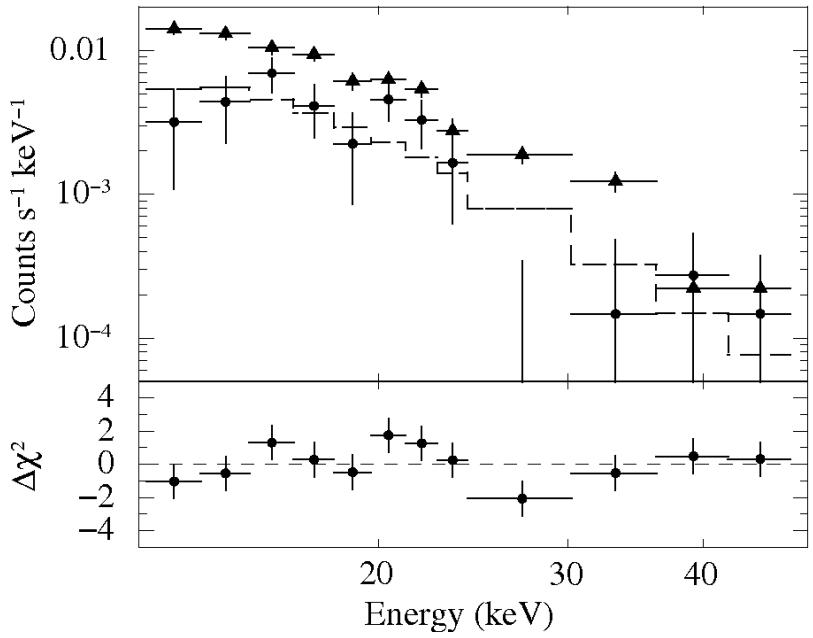

Figure 4.7: HXD-PIN pulsed spectrum obtained by subtracting the off-peak spectrum from the on-peak spectrum (closed circle). Dashed histogram represents the best-fit power-law model. Total HXD-PIN spectrum subtracted NXB is also shown as triangle.

density were also consistent with those of Chandra. Therefore, we conclude that Src 1 is an intrinsically stable source. The column density of Src 1 is very large compared with the total Galactic $N_{\rm H} \sim 1.6 \times 10^{22}$ cm^{-2} toward that direction estimated from the FTOOLS `nh` tool derived from the HI map by Dickey & Lockman (1990). If we assume that the mean density of the intersteller medium is 1 cm^{-3}, the column density of Src 1 suggests that it locates at a distance of $\sim$18 kpc. This value seems to be too large. On the other hand, Src 1 locates near an unusual cluster of a red supergiant stars RSGC1 (Figer et al., 2006), which is determined a distance of 6.6 kpc from the radial velocity of the cluster (Davies et al., 2008). It is acceptable that Src 1 locates at a distance of 6.6 kpc if we assume Src 1 was born in the cluster. The large difference between the column density determined by the X-ray observations and that of the Galactic value may due to the extinction by the dense intersteller medium.

From the evidences that Src 1 has an energetic pulsar embedded in the diffuse emission and its flux stays constant, we are convinced that Src 1 is a PWN.

Gotthelf & Halpern (2008) claimed that the Chandra spectrum of the pulsar component was significantly harder ($\Gamma = 0.5 \pm 0.2$) than the pulsed component obtained by RXTE in 2–20 keV ($\Gamma = 1.2 \pm 0.1$). They suggested a steepening of the spec-

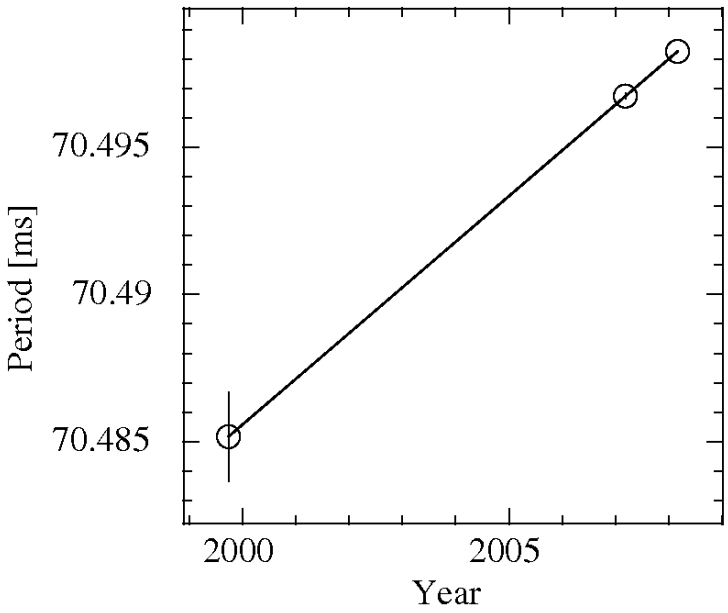

Figure 4.8: History of the pulse period. The data points from left to right indicate the pulse periods determined by ASCA, Suzaku and RXTE, respectively.

trum in the 8–15 keV band. The Suzaku HXD-PIN data indicate a photon index of $\Gamma = 2.0^{+1.0}_{-0.9}$ for the pulsed component in the 12–50 keV. This photon index is consistent with the RXTE result and supports the steepening of the spectrum in the hard X-ray band.

Nature of Src 2

Src 2 was also observed by ASCA and is known to have a non-thermal spectrum (Bamba et al., 2003a). Current Suzaku observation suggests no time variation of Src 2 since the ASCA observation. Therefore we speculate that Src 2 is also a PWN. However, Chandra could detect neither the putative pulsar point source in Src 2 nor any pulsation (Gotthelf & Halpern, 2008). Further observations are required to reveal the nature of this source.

Origin of HESS J1837–069

Because Src 1 is slightly offset from the center of HESS J1837–069, we need to check the chance coincidence of the sources. The chance probability for high-power pulsars and VHE γ-ray sources was estimated by Carrigan et al. (2007). For Src 1 with $\dot{E}/d^2 \sim 10^{35}$ ergs s^{-1} kpc^{-2}, the chance probability is $\sim 12\%$. Thus we consider Src 1 is likely to be associated to HESS J1837–069.

Src 2 is also located at the opposite edge of the extension of HESS J1837–069 with the angular distance of $4'7$ from its center. Thus Src 2 may also contribute to HESS J1837–069.

4.2 HESS J1809–193

4.2.1 Previous Observations

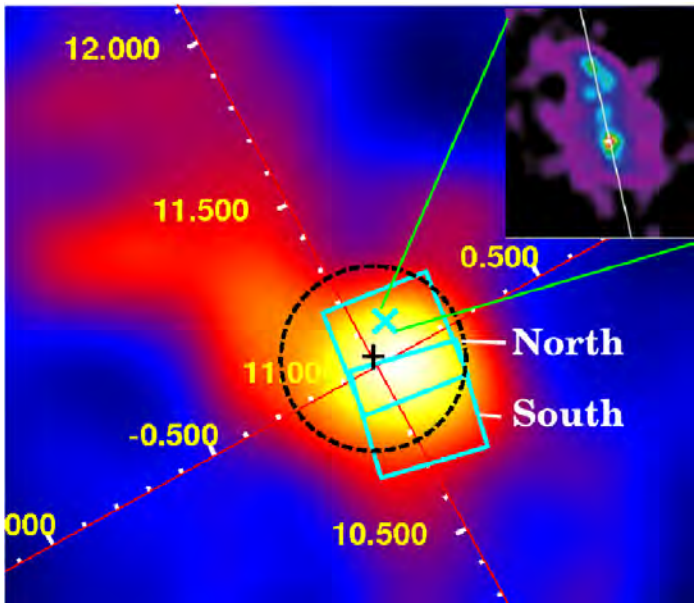

Figure 4.9: Smoothed excess map measured by HESS around HESS J1809–193. Fits image was provided by Gerd Pühlhofer. The position of the pulsar PSR J1809–1917 is marked with a cyan oblique cross. The best fit position for the γ-ray source is marked with a black cross and the fit ellipse with a dashed line. Two cyan squares indicate the two pointings of XIS FOVs, which are referred to as north and south pointings, respectively in this study. On the top right of this figure, an X-ray image of PSR J1809–1917 obtained by Chandra is shown, which is adapted from Kargaltsev & Pavlov (2007).

The first HESS observations of the region around PSR J1809–1917 were made as part of the systematic survey of the inner Galaxy from May through June 2004 (Aharonian et al., 2005a, 2006a). As the marginal VHE γ-ray signal was detected, HESS J1809–193 was observed again in 2004 and 2005 and significant γ-ray emission was confirmed (Aharonian et al., 2007). Recent study of this source was reported by Renaud et al. (2008). The excess map is shown in figure 4.9. Fitting the excess map with a 2-D symmetric Gaussian, the best fit position and intrinsic source extension (in rms) were determined as (RA, Dec) = ($18^{\rm h}09^{\rm m}52^{\rm s}$, $-19°23'42''$) and $0°.25 \pm 0°.02$, respectively.

PSR J1809–1917 is a radio pulsar discovered by the Parkes Multibeam Pulsar Survey (Morris et al., 2002). The pulsar is located at the position of (RA, Dec) = ($18^{\rm h}09^{\rm m}43^{\rm s}.1$, $-19°17'38''$) with a pulse period of P = 82.7 ms and the period

derivative of $\dot{P} = 2.55 \times 10^{-14}$ s s^{-1}. The distance to the source was determined as $d = 3.5$ kpc from the pulsar's dispersion measure using the NE2001 Galactic electron-density model (Cordes & Lazio, 2002). The characteristic age and the spin-down luminosity are $\tau_c = 51$ kyr and $\dot{E} = 1.8 \times 10^{36}$ ergs s^{-1}, respectively. The surface magnetic field is estimated to be $B_{\rm s} = 1.6 \times 10^{12}$ Gauss.

The γ-ray spectral analysis performed by Komin et al. (2007) indicated that the spectral slope was different between the regions near the pulsar and away from the pulsar. This is the second case that such a spectral slope variation was revealed in the VHE γ-ray emission[8].

ASCA observation revealed diffuse, non-thermal emission in the vicinity of PSR J1809–1917 (Bamba et al., 2003a). Kargaltsev & Pavlov (2007) detected a bright point X-ray source which was positionally consistent with the pulsar PSR J1809−1917, and resolved the pulsar and its surrounding PWN utilizing the very high angular resolution of Chandra; the PWN has a head-tail profile, with southern pulsar and northern tail. They say that this cometary morphology can be attributed to a bow shock created by the pulsar moving supersonically to the southern direction.

4.2.2 Observations

We observed HESS J1809–193 with Suzaku in April, 2008. The observation was carried out with two pointings, north and south, in order to cover the pulsar and extended VHE γ-ray emission region along the direction of the elongated shape of the PWN presented by Kargaltsev & Pavlov (2007), which is reproduced in figure 4.9. Three XISs (XIS 0, 1, 3) were operated in the normal clocking mode with the Spaced-row Charge Injection (SCI) (Nakajima et al., 2008). We analyzed the data prepared by the version 2.2 pipeline. We concentrated on the analysis of the XIS data because we are interested in the spatial variations of the emission. We applied the standard screening criteria to the XIS[9] data to obtain cleaned event lists. After the data screening, the net exposures was 51.5 ks and 44.2 ks for the north and south pointings of XIS, respectively. The exposures are summarized in table 4.5 with the journal of Suzaku observations. We used HEADAS version 6.5 software package for the data analysis.

[8]The other case is HESS J1825–137 (Aharonian et al., 2006e), which is largely extended in both VHE γ-ray and X-ray band (Uchiyama et al., 2008b).

[9]http://www.astro.isas.jaxa.jp/suzaku/process/v2changes/criteria_xis.html

Table 4.5: Journal of the two sets of Suzaku observations of HESS J1809–193

Sequence ID	503078010	503079010
Start time (UT)[1]	2008/03/31 14:06	2008/04/01 16:34
End time (UT)[1]	2008/04/01 16:30	2008/04/02 14:47
Aim point R.A. (J2000.0)	$18^{\rm h}09^{\rm m}37^{\rm s}.4$	$18^{\rm h}09^{\rm m}21^{\rm s}.0$
Aim point Decl. (J2000.0)	$-19°21'24''$	$-19°32'02''$
Net exposure (ks)	51.5	44.2

[1] Time form of yyyy/mm/dd hh:mm

4.2.3 Analysis & Results

X-ray Image

We extracted the XIS image in 0.4–1.0 keV and 2.0–10.0 keV for each sensor. The data between 5.73–6.67 keV were removed from the image to exclude the calibration sources. We corrected the vignetting effect by dividing the image by the flat sky image simulated using the XRT+XIS simulator `xissim` (Ishisaki et al., 2007). In this simulation, we assumed the input energy spectrum as that extracted from the region enclosed with a red rectangle, which can be considered as GRXE (as explained in the next subsection). The image was binned to 8×8 pixels and smoothed with a Gaussian function of $\sigma = 0'.42$. Combined Suzaku XIS (0+1+3) image is shown in figure 4.10.

In order to determine the extension of the non-thermal emission, we extracted photons in the green rectangle region shown in figure 4.11 (top). We created a 1-dimensional profile of the surface brightness from the rectangle region shown in figure 4.11 (top), which runs from north to south. The profile obtained is shown in figure 4.11 (bottom). Note that the surface brightness is normalized to the peak brightness. We fitted the profile with a Gaussian function plus a constant to evaluate its extension. When fitting, we ignored the brightest part (Src 1) of an width of $2'.9$, because we were interested in the dim emission around the source. The profile becomes constant (which can be considered as GRXE; see §4.2.3) more that $\sim 17'$ away from the pulsar. The Gaussian center was found to be offset by $\sim 3'$ from the pulsar and the rms width to be $\sigma = 6'.8 \pm 1'.0$.

Energy Spectra

We studied the spatial variations of the X-ray energy spectra with the Suzaku XIS data. We generated detector and auxiliary response files using `xisrmfgen` and `xissimarfgen` (Ishisaki et al., 2007) and performed model fitting to the spectra using XSPEC version 12.4.0.

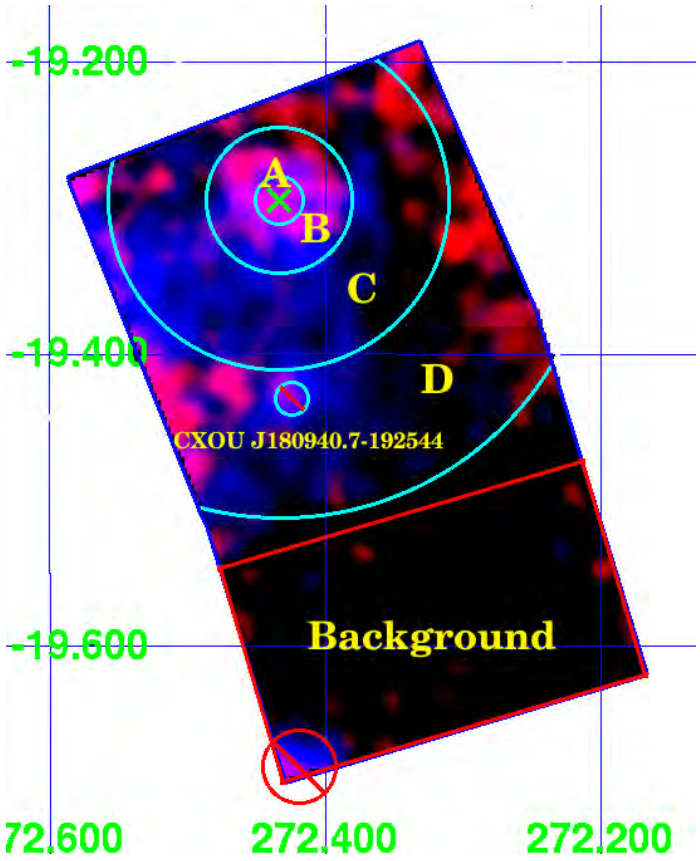

Figure 4.10: Suzaku XIS (0+1+3) image of the region including HESS J1809−193 in equatorial coordinate. The data between 5.73–6.67 keV were filtered out to remove the calibration sources. The brightness represents vignetting-corrected, log-scaled intensity levels. The pseudo-color represents the energy bands; red shows the 0.4–1.0 keV band and blue 2.0–10.0 keV band. Green cross indicates the position of the pulsar. Cyan concentric circles show the region, from which the energy spectra were extracted to see the spectral parameters around the pulsar. The background region is indicated as a red box excluding a bright source at the south corner.

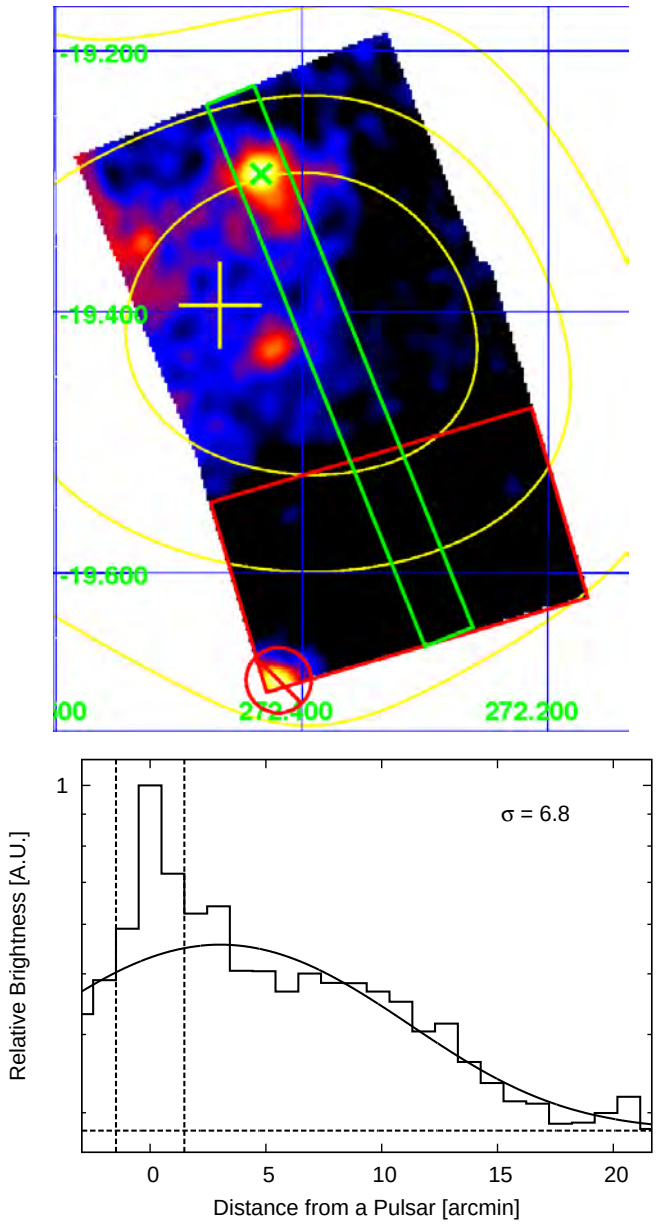

Figure 4.11: Top: Suzaku XIS image of the region including HESS J1809–193. The pseudo-color represents vignetting-corrected, log-scaled intensity levels in the 2.0–10.0 keV band. Yellow line represents the 80%, 60%, and 40% contour to the peak of the VHE γ-ray image of HESS J1809–193, and yellow cross indicates the centroid of the HESS source (Renaud et al., 2008). Bottom: normalized 1-dimensional profile of the surface brightness in the 2.0–10.0 keV band along the direction from north to south in the green rectangle indicated in figure 4.11 with a spatial bin size of $1'.0$. Solid curve and horizontal dashed line show the best-fit Gaussian profile and a constant, respectively. Bright part near the pulsar was ignored in this fit ($2'.9$ wide, inner part between the two vertical dashed lines).

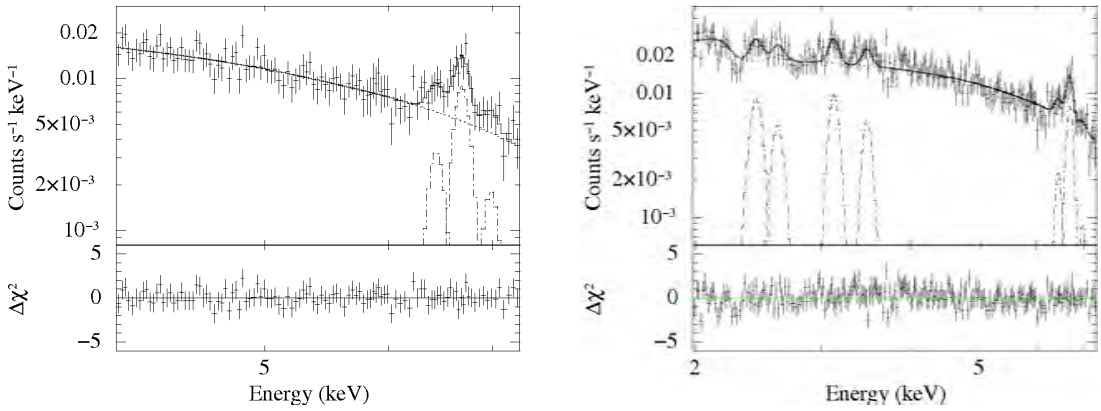

Figure 4.12: Left: NXB-subtracted XIS spectrum in the 4.0–7.2 keV band extracted from the region enclosed with a red rectangle. The best-fit model, an absorbed power-law with three iron lines, is also shown in a solid line (each component in a dot-dashed line). The bottom panel shows residuals to the best-fit model. Right: the same as the left one, but in the 2.0–4.0 keV band. Narrow Gaussians were added to the model below 4 keV.

First we examined the spectra from the red rectangle in figure 4.11 in order to examine the influence of GRXE. The bright source at the south-east corner was removed for this analysis. The equivalent widths of iron lines were compared with those of GRXE. The X-ray emission was so dim that we averaged all of the available XISs (XIS 0,1,3) data. We subtracted a non X-ray background (NXB) estimated using `xisnxbgen` (estimation methods were described in Tawa et al. (2008)). Many emission lines were noticed below 4 keV as shown in figure 4.12 (right), as previously reported by Ebisawa et al. (2008) and so on. Because the NXB becomes high above 7.2 keV in XIS 1, we fitted the spectrum only in 4.0–7.2 keV. The model adopted is a power-law plus three narrow Gaussian (intrinsic width fixed to zero, and the center energies optimized around 6.4 keV, 6.7 keV and 7.0 keV). The spectrum and the best-fit model are shown in figure 4.12 (left). The equivalent widths of the iron lines are summarized in table 4.6. These equivalent widths are comparable to those of GRXE described in Ebisawa et al. (2008). Thus we consider that the X-ray emission in this region can be regarded as pure GRXE and no significant contribution from pulsar is noticed.

Next we extracted spectra around the pulsar from the following regions: $1'$ radius from the pulsar, concentric annuli of radii $1' < r < 3'$, $3' < r < 7'$, and $7' < r < 13'$, in order to examine the spectral shape of the pulsar and the surrounding nebula. We refer these regions as "A", "B","C","D", respectively. These regions are shown in figure 4.10. We used the XIS data only from the north pointing for this analysis; a point source designated as CXOU J180940.7–192544 by Kargaltsev

Table 4.6: Equivalent widths of the iron lines in the background region in figure 4.10.

Center energy (keV)	6.44 ± 0.07	6.69 ± 0.02	6.98 ± 0.08
Equivalent width (eV)	70 (0–140)	240 (160–550)	50 (0–170)
Center Energy* (keV)	6.41 ± 0.02	6.670 ± 0.006	7.00 ± 0.03
Equivalent width* (eV)	80 (60–100)	350 (310–390)	70 (40–100)

Note. — Errors represent single-parameter 90% confidence limit.
* Equivalent width determined by the GRXE observation with Suzaku by Ebisawa et al. (2008).

& Pavlov (2007) was removed. We subtracted the spectrum extracted from the red rectangle in the figure as a background, which can be regarded as pure GRXE as explained in the previous paragraph. We carried out simultaneous model fit to these spectra. Two models were tried: a simple power-law and a power-law + low-temperature thin thermal emission model (MEKAL model in XSPEC; Mewe et al. (1985)). The data between 5.73–6.67 keV were removed from the fitting to exclude the calibration sources. The best-fit model of the latter is shown in figure 4.13 for each region and the best-fit parameters are listed in table 4.7. Comparing the reduced χ^2 of these two models, we concluded that there are significant soft thermal emission in this field. As seen in the figures, thermal emission dominates below 1 keV. It is seen from figure 4.10 that this thermal emission is highly non-uniform. As described in table 4.7, we could not find significant change of the spectral indices in the X-ray band, contrary to the results of the HESS observations.

Although we could not find any spectral variations when the sky region around the pulsar was divided by concentric circles, different scheme of division might detect spatial variation of the spectral slope. Therefore, we tried to divide the sky region of the north pointing into the check pattern as shown in figure 4.14 (left), and to find the possible spatial variations of the spectral slope. Here we refer to these regions as the number indicated in figure 4.14 (left) with a prefix "Grid" (Grid1, Grid2, ...). We used a two component model for the fit: an absorbed power-law plus the GRXE. We do not include the MEKAL model because we restricted the spectral fit above 2 keV as shown in figure 4.13. Because of the poor statistics of data in each grid, we used a model spectrum for GRXE, instead of the GRXE spectrum itself obtained from the background region in figure 4.10, to subtract the background.

The model spectrum of GRXE was constructed as follows. We extracted the background spectrum again and fitted in the 2.0–7.2 keV band with the model of an absorbed power-law plus 7 narrow Gaussians (three for the iron lines and four for the emission lines below 4 keV) (Ebisawa et al., 2008). The absorption column density was fixed to 1.0×10^{22} cm^{-2}, because it was difficult to determine with data only above 2.0 keV. The best-fit parameters are listed in table 4.8. We generated the GRXE

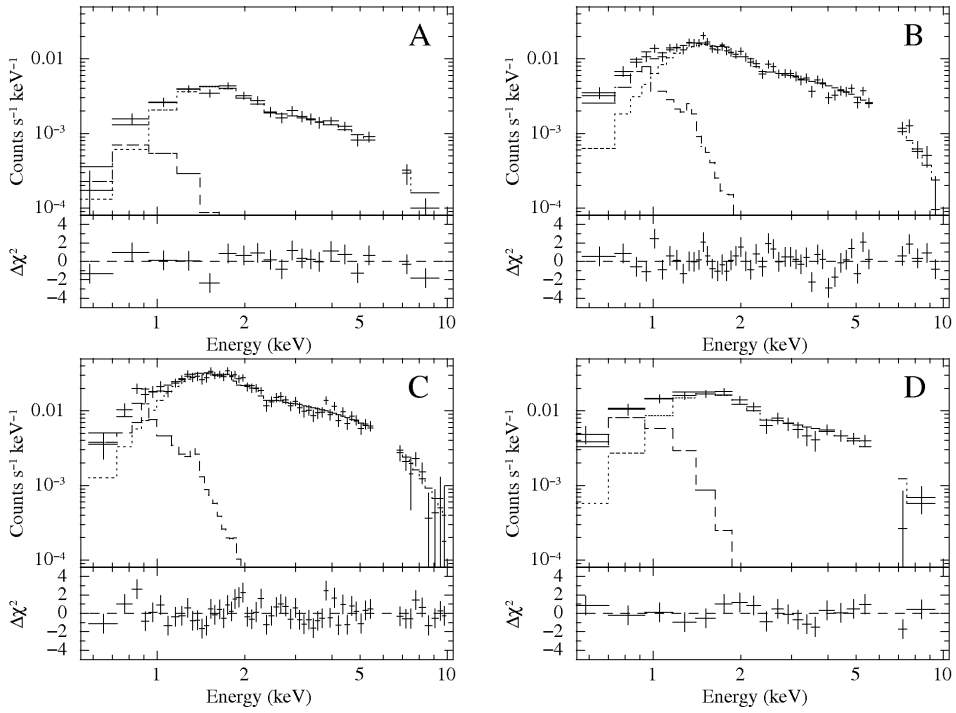

Figure 4.13: Background-subtracted XIS spectra of and around the pulsar. The spectra were fitted with the model of an absorbed power-law (dotted lines) plus thin thermal emission (dashed lines). Solid lines show the best-fit total models. The bottom panels show residuals to the best-fit models.

Table 4.7: Simultaneous fit results for the pulsar and the concentric annuli.

	Model	Power law	Power law + MEKAL
Common	N_H (10^{-21} cm^{-2})	$3.3^{+0.5}_{-0.4}$	$7.1^{+1.1}_{-1.2}$
	kT (keV)	—	$0.18^{+0.05}_{-0.04}$
A	Γ	$1.40^{+0.10}_{-0.09}$	1.67±0.12
	$F^{*}_{\rm pow}$	0.6 ± 0.1	0.6 ± 0.1
	$F^{\dagger}_{\rm mek}$	—	0.6×10^{-3}
B	Γ	$1.53^{+0.08}_{-0.07}$	$1.72^{+0.09}_{-0.10}$
	$F^{*}_{\rm pow}$	1.3 ± 0.1	1.3 ± 0.1
	$F^{\dagger}_{\rm mek}$	—	2.9×10^{-3}
C	Γ	1.38±0.07	$1.64^{+0.09}_{-0.10}$
	$F^{*}_{\rm pow}$	2.7 ± 0.1	2.7 ± 0.1
	$F^{\dagger}_{\rm mek}$	—	3.3×10^{-3}
D	Γ	$1.45^{+0.13}_{-0.12}$	$1.60^{+0.15}_{-0.16}$
	$F^{*}_{\rm pow}$	1.8 ± 0.2	$1.9^{+0.1}_{-0.2}$
	$F^{\dagger}_{\rm mek}$	—	4.2×10^{-3}
	χ^2 / dof	214.1 / 149	158.3 / 149

Note. — Errors represent single-parameter 90% confidence limit.
* Unabsorbed flux of the power-law component in the 2.0–10.0 keV band in the unit of 10^{-12} ergs cm^{-2} s^{-1}.
† Normalization of the MEKAL model is $10^{-14}/(4\pi D^2) \int n_{\rm H} n_e dV$ cm^{-5}, where D is the angular size distance to the source (cm), and n_e, $n_{\rm H}$ (cm^{-3}) are the electron and hydrogen densities respectively.

Table 4.8: Best-fit parameters of an absorbed power-law model with emission lines.

Model component	Parameter		Value
Continuum	$N_{\rm H}$ (10^{22} cm^{-2})		1.0 (fixed)
	Γ		$1.40^{+0.05}_{-0.06}$
Emission lines	Energy (keV)	S_{XV}	2.43 ± 0.02
		S_{XVI}	2.61 ± 0.04
		Ar_{XVII}	3.13 ± 0.02
		Ar_{XVIII}	$3.43^{+0.13}_{-0.07}$

Note. — Errors represent single-parameter 90% confidence limit.

spectrum model using these best-fit parameters except for the overall normalization. The normalization was readjusted taking account of the differences of the vignetting effect, size of the extraction region, and the exposure time between the north and south pointings. The correction factors of the vignetting effect, which are shown in figure 4.14 (right), were determined by simulation; we simulated the intensity map for the flat field with the energy spectrum of GRXE using `xissim`. We subtracted the non X-ray background (NXB) estimated using `xisnxbgen`. We fitted thus obtained spectra with an absorbed power-law plus the corrected GRXE model. Figure 4.16 shows the XIS spectrum (averaged for XIS 0, 1 and 3) and the best-fit model of each region in the 2.0–10 keV band. Because Grid 1, 4, 13 were illuminated with the calibration sources, the data between 5.73–6.67 keV were removed from the fit for these regions. As shown in these spectra, iron lines originated from GRXE were subtracted appropriately. This means that our estimation of the GRXE intensity was correct. Fit results are summarized in table 4.9. The spatial distribution of the spectral indices is shown in figure 4.15. We found that there is no systematic spatial variations in the spectral index in this field of view.

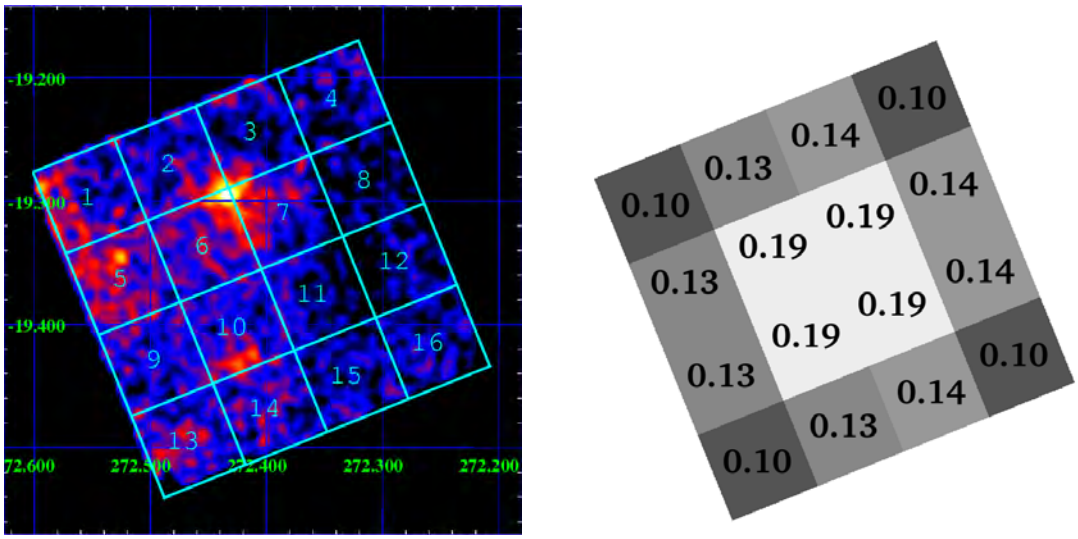

Figure 4.14: Left: Suzaku XIS image of the north pointing in the 2.0-10.0 keV band. Right: constant factors for each region to correct the vignetting effect and the difference of the exposure and the size of the extraction region between the source and the GRXE extracted regions as shown in figure 4.11 with the red rectangle.

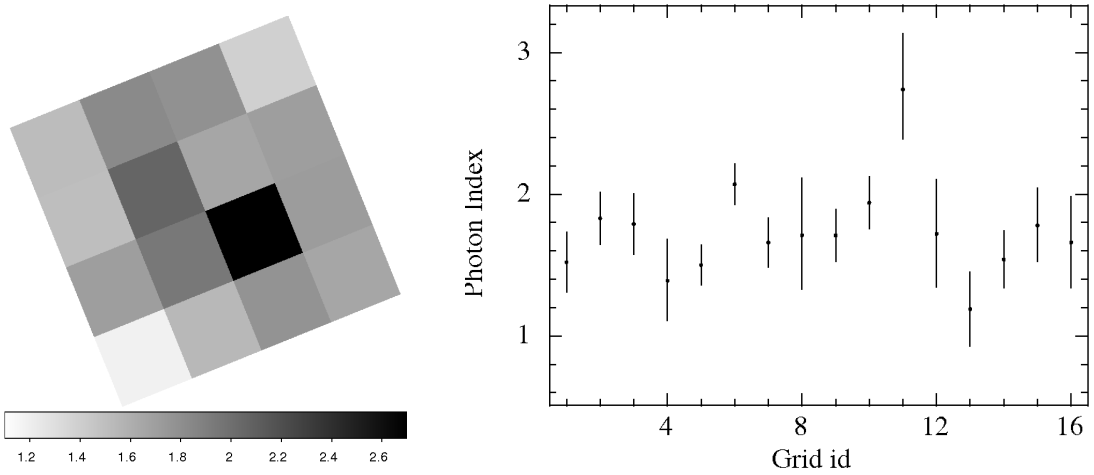

Figure 4.15: Spatial distribution of the spectral indices around PSR J1809–1917. Left: best-fit photon index map. Gray scale indicates the photon indices; light gray means the spectrum is hard while dark gray means soft. Right: photon indices of each grid with 90% error bars.

Table 4.9: Best-fit parameters of an absorbed power-law model plus GRXE model (fixed) for each grid.

Grid id	Γ	Flux* (10^{-13} ergs cm^{-2} s^{-1})
1	1.52 ± 0.21	8.7 ± 0.9
2	1.83 ± 0.18	7.8 ± 0.6
3	1.79 ± 0.21	5.9 ± 0.6
4	1.39 ± 0.28	$6.1^{+0.9}_{-0.8}$
5	1.50 ± 0.14	10.6 ± 0.7
6	2.07 ± 0.14	8.2 ± 0.5
7	1.66 ± 0.17	6.7 ± 0.5
8	$1.71^{+0.40}_{-0.38}$	3.0 ± 0.5
9	1.71 ± 0.18	7.1 ± 0.6
10	1.94 ± 0.18	5.9 ± 0.5
11	$2.74^{+0.39}_{-0.35}$	2.4 ± 0.4
12	$1.72^{+0.38}_{-0.37}$	2.9 ± 0.5
13	1.19 ± 0.26	8.3 ± 1.0
14	1.54 ± 0.20	$7.2^{+0.7}_{-0.6}$
15	1.78 ± 0.25	$4.4^{+0.6}_{-0.5}$
16	1.66 ± 0.32	4.9 ± 0.7

Note. — Errors represent single-parameter 90% confidence limit.
* Unabsorbed flux in the 2.0–10.0 keV band.

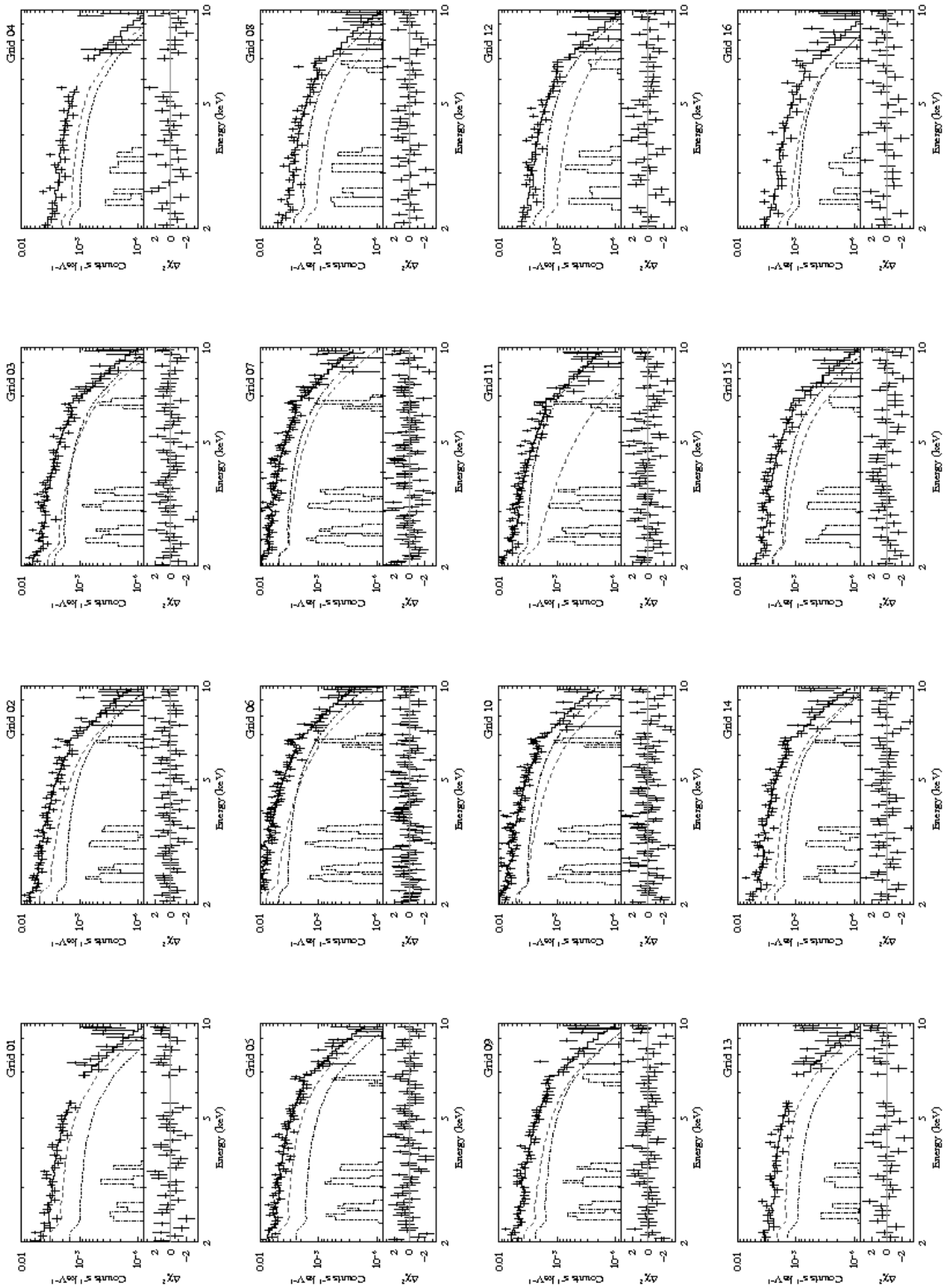

Figure 4.16: NXB-subtracted XIS spectra in the 2.0–10.0 keV band extracted from each grid shown in figure 4.14. Dashed line, dash-dot line and dash-dot histograms indicate the best-fit absorbed power-law model, a GRXE model and emission lines, respectively.

4.2.4 Summary

- We observed HESS J1809–193 with Suzaku. The observation was motivated by the variation of the spectral slope in the VHE γ-ray band. Although non-thermal diffuse X-ray emission was detected, no systematic variation in the X-ray spectral slope could be found in the diffuse emission.

- The synchrotron nebula is extended over $\sigma \sim 7'$, which was determined by fitting the surface brightness profile with a Gaussian function. This size is smaller than that of the HESS source with the rms size of $\sim 15'$. If we define the size of the nebula as 3σ radius of the profile, the size becomes $\sim 21 d_{3.5}$ pc, where $d_{3.5} = d/3.5$kpc is the distance to the associated pulsar PSR J1809–1917 normalized by 3.5 kpc.

4.3 HESS J1825–137

4.3.1 Previous Observations

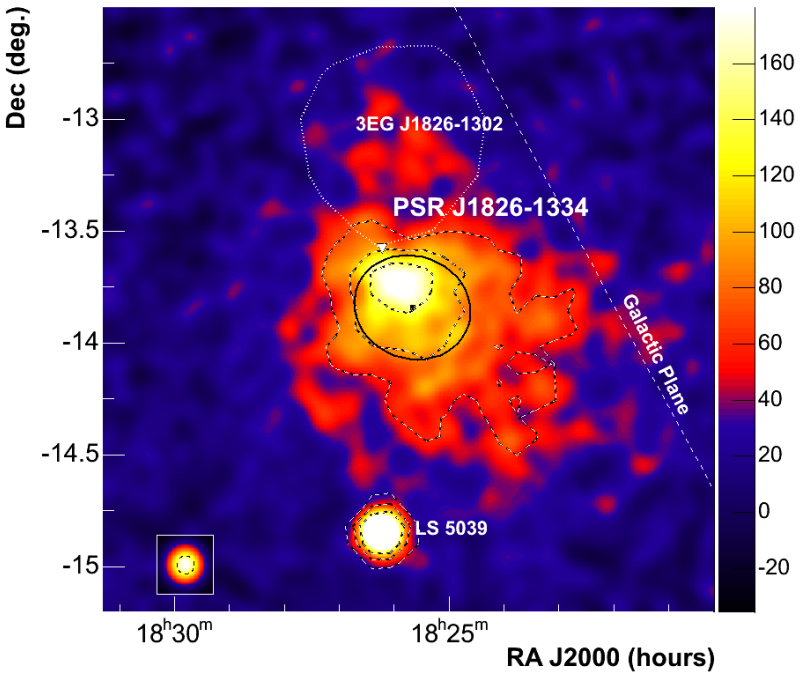

Figure 4.17: HESS excess map of $2°.7 \times 2°.7$ field of view around HESS J1825–137 smoothed with a radius of $2'.7$, which is adapted from Aharonian et al. (2006e). The dashed black and white contours denote the 5, 10 and 15σ significance levels (the 5σ contour being the outermost one). The best fit position of HESS J1825–137 is marked with a black square, the best extension and position angle with a black ellipse. The position of the pulsar PSR J1825–1334 is marked with a white triangle, while the Galactic plane is shown as a white dashed line.

HESS J1825–137 was discovered during the HESS Galactic plane survey in 2004 (Aharonian et al., 2005a, 2006a), and reobserved in 2005 as a part of the observations of the nearby (distance $\sim 1°$) γ-ray emitting microquasar LS 5039, which included HESS J1825–137 in the field of view. The excess map is shown in figure 4.17. HESS J1825–137 clearly shows an extended profile compared to the PSF. Assuming an asymmetric 2-D Gaussian profile, the best fit position of the excess center was determined as (RA, Dec) = ($18^h25^m41^s$, $-13°50'20''$). The intrinsic width of the source was found to be slightly elongated with $0'.26 \pm 0'.02$ for the major axis and $0'.23 \pm 0'.02$ for the minor axis (Aharonian et al., 2006e). For the spectral analysis, events within $\theta = 0°.8$ from the center of the source were regarded as the source events. The spectrum could be

reproduced by a power-law with a photon index of $2.38 \pm 0.02_{\rm stat} \pm 0.15_{\rm sys}$. The source flux in the 1–10 TeV was $(4.9 \pm 1.0) \times 10^{-11}$ ergs cm^{-2} s^{-1}.

PSR J1826–1334 (or PSR B1825–13) is a radio pulsar located at the position of (RA, Dec) = ($18^{\rm h}26^{\rm m}13^{\rm s}.2$, $-13°34'47''$), which is at the edge of the γ-ray emission. Its period and period derivative are 101 ms and 7.5×10^{-14} s s^{-1}, respectively (Manchester et al., 2005). Distance to the source was determined from the pulsar's dispersion measure as $d = 3.9$ kpc using the NE2001 Galactic electron-density model (Cordes & Lazio, 2002). The characteristic age and the spin-down luminosity are $\tau = 21$ kyr and $\dot{E} = 2.8 \times 10^{36}$ ergs s^{-1}, respectively. The strength of surface magnetic field is $B_{\rm s} = 2.5 \times 10^{12}$ Gauss.

XMM-Newton observation revealed an extended core of $30''$ surrounding the pulsar embedded in a faint, diffuse nebula to the south of the pulsar (Gaensler et al., 2003). Recently, Uchiyama et al. (2008b) observed this source with Suzaku and found a diffuse X-ray emission extending up to $15'$ from the pulsar. They fitted the spectrum of the diffuse emission with an absorbed power-law model, which yielded a photon index of $\Gamma = 1.98^{+0.05}_{-0.06}$ and an absorption column of $0.93^{+0.06}_{-0.09} \times 10^{22}$ cm^{-2}. The absorption corrected total flux in the Suzaku XIS field of view in the 2–10 keV band was $\sim 5 \times 10^{-12}$ ergs cm^{-2} s^{-1}.

4.3.2 Observations

Suzaku archival data were available for the region including PSR J1825–1334 and the peak of the VHE emission in the XIS FOV. We analyzed the data prepared by the version 2.0 pipeline. All of the four XISs were operated when this observation was performed. We applied the standard screening criteria[10] to the XIS data. After the data screening, the net exposure was 50.3 ks.

XMM-Newton archival data were also available with PSR J1825–1334 at its optical axis. We also analyzed the XMM-Newton MOS data as a cross-check of the Suzaku XIS analysis on the extension of non-thermal diffuse emission. We used the standard processed and filtered event data. The journal of this observation is summarized in table 4.10.

4.3.3 Analysis & Results

X-ray Image

The XIS image in the 3.0–9.0 keV band was created with three FI chips (XIS 0,2,3). The region illuminated by the calibration sources were removed from the image. The image was binned to 8×8 pixels and smoothed with a Gaussian function of

[10]http://www.astro.isas.jaxa.jp/suzaku/process/v2changes/criteria_xis.html

Table 4.10: Journal of the Suzaku/XMM-Newton observations of HESS J1825–137

Satellite	Suzaku	XMM-Newton	
Sequence ID	501044010	0054540501	0054540701
Start time[1]	2006/10/17 19:37	2001/10/16 04:45	2001/10/18 04:43
End time[1]	2006/10/19 04:02	2001/10/16 12:29	2001/10/18 11:59
R.A. (J2000)	$18^{\rm h}26^{\rm m}00^{\rm s}.0$	$18^{\rm h}26^{\rm m}13^{\rm s}.2$	$18^{\rm h}26^{\rm m}13^{\rm s}.2$
Decl. (J2000)	$-13°41'42''$	$-13°34'47''$	$-13°34'47''$
Net exposure (ks)	50.3	19.0	23.1

[1] Time form of yyyy/mm/dd hh:mm (UT)

$\sigma = 0'.21$. Combined image corrected for the vignetting effect after subtracting NXB is shown in figure 4.18 (top). Figure 4.18 (bottom) shows the profile of the relative surface brightness in the green rectangle region shown in figure 4.18 (top). The horizontal scale represents a distance from PSR J1825–3825. We fitted the profile with a Gaussian function plus a constant model ignoring the profile in the region with the radius of $1'$ from PSR J1825–3825. Constant was set free and the Gaussian center was fixed at the pulsar's position. The best-fit rms width of the Gaussian profile was found to be $\sigma = 3'.5 \pm 0'.4$.

We also created XMM-Newton MOS image in the 2.0–12.0 keV band to cross-check the result of the Suzaku XIS analysis. Figure 4.19 (top) shows the combined XMM-Newton MOS (1 + 2) log-scaled intensity map smoothed with a Gaussian function of $\sigma = 12''$. Vignetting was not corrected. Figure 4.19 (bottom) shows the profile of the relative surface brightness in the green rectangle region shown in figure 4.19 (top). We fitted the profile with a Gaussian function plus a constant model ignoring the same width as the case of Suzaku XIS analysis to compare the result under the same conditions. Constant was set free and the Gaussian center was fixed at the pulsar's position. The best-fit rms width of the Gaussian profile was found to be $\sigma = 3'.2 \pm 0'.2$. The profile is rather narrow compared with that determined by XIS, probably because the XMM-Newton MOS image was not vignetting-corrected. Thus we regard this difference of $\sim 0'.3$ as the systematic error of the width determined by XMM-Newton MOS.

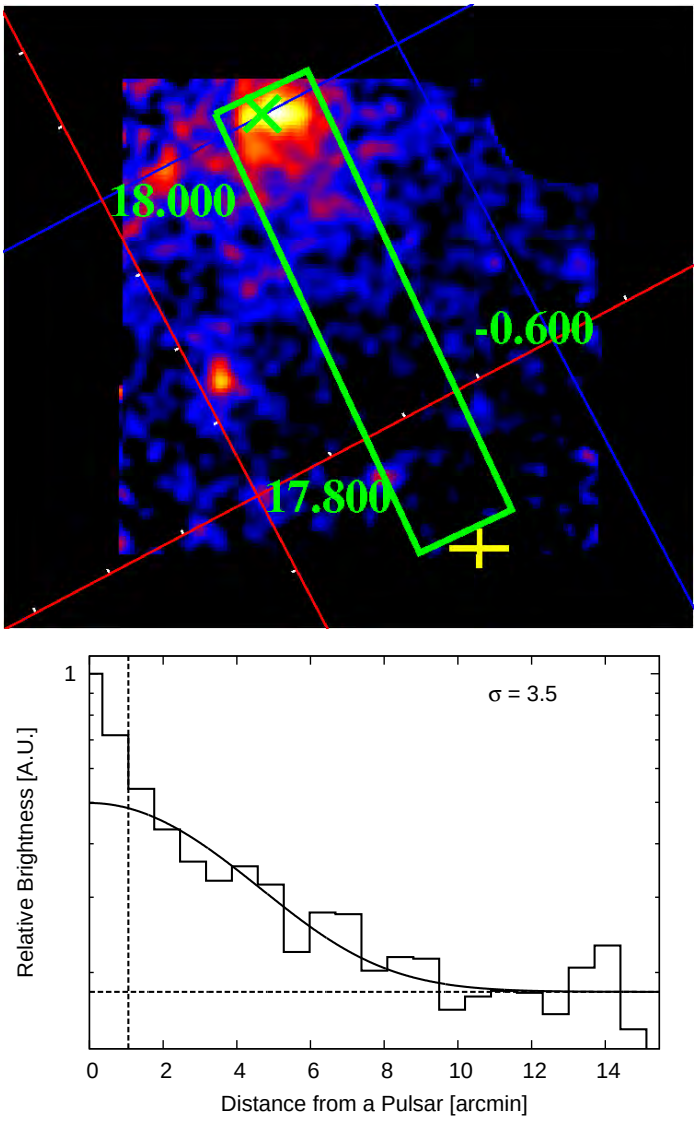

Figure 4.18: Top: Suzaku XIS (0+2+3) image around HESS J1825–385. The pseudo-color represents vignetting-corrected, log-scaled intensity levels in the 3.0–9.0 keV band. Green and yellow crosses indicate the pulsar position and the best-fit position of VHE γ-ray emission with the fitting error. This image is by courtesy of Hideki Uchiyama in Kyoto University. Bottom: a profile of the relative surface brightness along the direction from NE to SW from the enclosed region with a green rectangle indicated in the top panel with a spacial bin size of $42''$. Solid and dashed lines show the best-fit Gaussian profile and a constant, respectively. Bright part near the pulsar was ignored in this fit ($2'.1$ wide, inner part of the vertical dashed line).

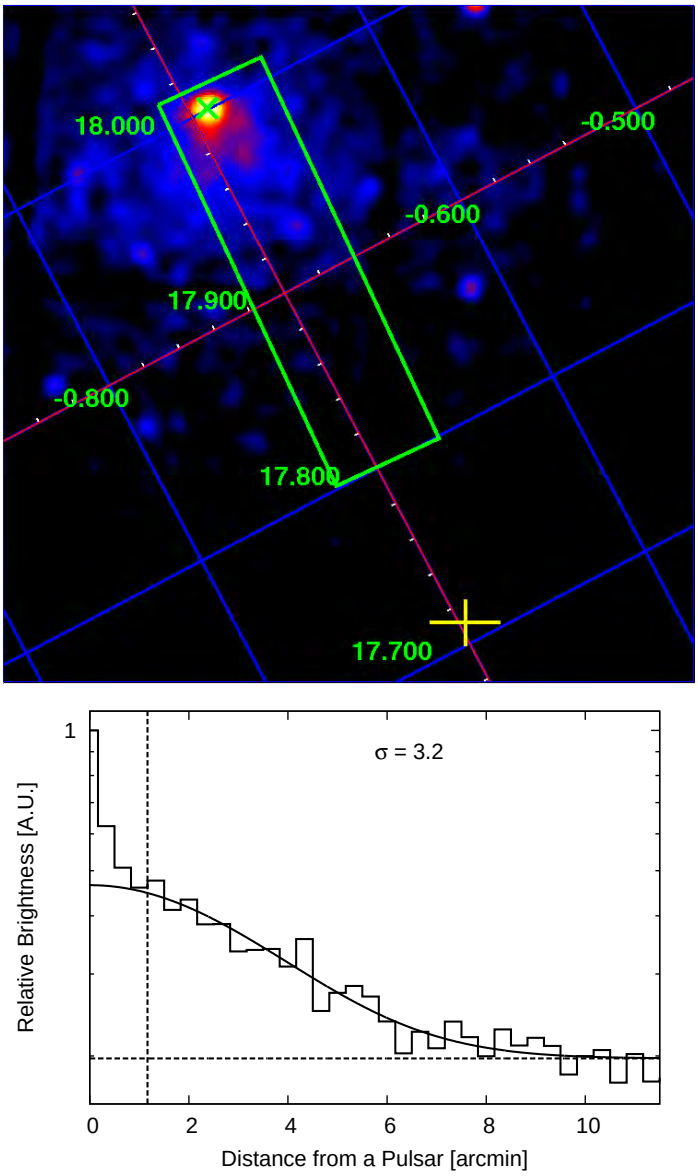

Figure 4.19: Top: XMM-Newton MOS (1+2) image around HESS J1825–385. The pseudo-color represents log-scaled intensity levels in the 2.0–12.0 keV band. Vignetting was not corrected. Green and yellow crosses indicate the pulsar position and the best-fit position of VHE γ-ray emission with the fitting error. Bottom: a profile of the relative surface brightness along the direction from NE to SW from the enclosed region with a green rectangle indicated in the top panel with a spacial bin size of $20''$. Solid and dashed lines show the best-fit Gaussian profile and a constant, respectively. Bright part near the pulsar was ignored in this fit ($2'.3$ wide, inner part of the vertical dashed line).

4.4 Kookaburra (PSR J1420–6048, Rabbit)

4.4.1 Previous Observations

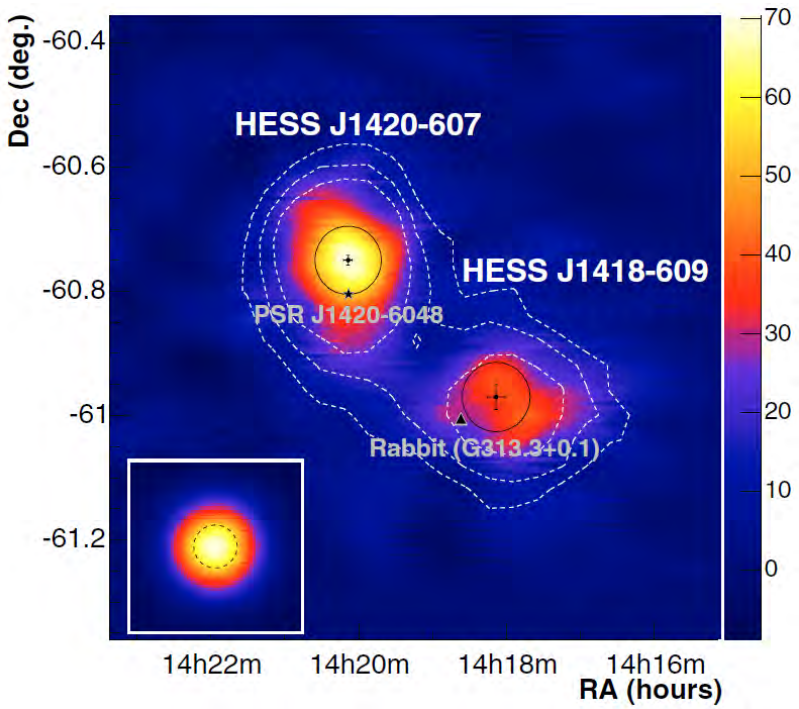

Figure 4.20: A smoothed excess map (smoothing radius 2′) measured by HESS in the Kookaburra region, adapted from Aharonian et al. (2006c). In the bottom left corner the point-spread function of this dataset smoothed in the same way is shown (along with the smoothing radius as a black dashed line). The white contours denote the 5σ, 7.5σ and 10σ significance levels (with the outermost being the 5σ contour). The position of the pulsar PSR J1420–6048 is marked with a star, the position of the Rabbit is marked with a black triangle. The best fit positions of the two sources are marked with error crosses, and the best-fit extensions are given as black circles.

The complex of compact and extended radio/X-ray sources, called Kookaburra (designated by Roberts et al. (1999)), spans over about one square degree along the Galactic plane around $l = 313°.4$. HESS observations of the Kookaburra region were conducted as a survey of the Galactic plane (Aharonian et al., 2005a, 2006a), which was summarized in Aharonian et al. (2006c). Two sources of VHE γ-rays were discovered in this region; the brighter of the two sources, HESS J1420–607, is centered at the position of (RA, Dec) = ($14^{\mathrm{h}}20^{\mathrm{m}}09^{\mathrm{s}}$, $-60°45'36''$) with an intrinsic extension of $3'.3 \pm 0'.5$, and the slightly less bright second source, HESS J1418–609, is centered at the position of (RA, Dec) = ($14^{\mathrm{h}}18^{\mathrm{m}}04^{\mathrm{s}}$, $-60°58'31''$) with an intrinsic extension

of $3'.4 \pm 0'.6$ (a major-axis of $4'.9 \pm 1'.5$ and a minor-axis of $2'.7 \pm 0'.7$ fitted with an elongated Gaussian shape). The smoothed excess map is shown in figure 4.20. The energy spectra of the two sources were extracted both within a radius of $0°.16$ to avoid any overlap in the integration regions for the two sources. The energy spectrum of HESS J1420 − 607 could be fitted with a power-law with a photon index of $2.17 \pm 0.06_{\rm stat} \pm 0.1_{\rm sys}$. The flux in the 1–10 TeV was $(11 \pm 2) \times 10^{-12}$ ergs cm^{-2} s^{-1}. The photon index of HESS J1418 − 609 had a similar value of $2.22 \pm 0.08_{\rm stat} \pm 0.1_{\rm sys}$. The flux of this source in the 1–10 TeV was $(7.7 \pm 1.6) \times 10^{-12}$ ergs cm^{-2} s^{-1}.

There is an energetic pulsar PSR J1420–6048 at the south of HESS J1420–607. It is located at (RA, Dec) = ($14^{\rm h}20^{\rm m}08^{\rm s}.20$, $-60°48'17''.2$), which is $\sim 3'.1$ offset from the center of the VHE γ-ray emission. PSR J1420–6048 is a 68 ms radio/X-ray pulsar with a period derivative of $\dot{P} = 8.3 \times 10^{-14}$ s s^{-1} (D'Amico et al., 2001; Ng et al., 2005). The distance to the pulsar was estimated as $d = 5.6$ kpc based on the pulsar's dispersion measure with the NE2001 Galactic electron-density model (Cordes & Lazio, 2002). The characteristic age and the spin-down luminosity are $\tau = 13$ kyr and $\dot{E} = 1.0 \times 10^{37}$ ergs s^{-1}, respectively. The strength of surface magnetic field is $B_{\rm s} = 2.5 \times 10^{12}$ Gauss.

Chandra observation revealed a diffuse X-ray emission in K3 nebula (designated by Roberts et al. (1999) with the radio observation) around PSR J1420–6048 (Ng et al., 2005). Spectral fitting with an absorbed power-law model to the K3 nebula ($2'$ radius from the pulsar) yielded an absorption column of $N_{\rm H} = 5.4^{+2.2}_{-1.7} \times 10^{22}$ cm^{-2} with a photon index of $\Gamma = 2.3^{+0.9}_{-0.8}$. The unabsorbed flux of the whole K3 nebula in the 2–10 keV band was determined as $F_X = (1.3 \pm 0.14) \times 10^{-12}$ ergs cm^{-2} s^{-1}.

Ng et al. (2005) also analyzed the Rabbit nebula using XMM-Newton observation. It is located at the Eastern edge of HESS J1418–609 with a distance of $8'.2$ to the best-fit central position of the VHE emission. They found two point-like sources, labeled as R1 and R2. The brighter source (R1) is located at the edge of the Rabbit, while the fainter source (R2) at (RA, Dec) = ($14^{\rm h}18^{\rm m}39^{\rm s}.90$, $-60°57'56''.5$), which appears embedded in the diffuse emission. Timing analysis with the EPIC pn data revealed a 108 ms pulsation with a period derivative of $\dot{P} = 1.07 \times 10^{-12}$ s s^{-1} from R2, although not highly significant. Fitting the spectrum from the whole Rabbit nebula ($3'$ radius) with an absorbed power-law model, they found an absorption column of $N_{\rm H} = 1.4 \pm 0.2 \times 10^{22}$ cm^{-2} and a photon index of $\Gamma = 1.5 \pm 0.14$. A total unabsorbed flux in the 2–10 keV band was determined as $F_X = (7.3 \pm 0.2) \times 10^{-12}$ ergs cm^{-2} s^{-1}.

4.4.2 Observations

We analyzed the archival data of the two sources in the Kookaburra region. We used the data acquired by Chandra for PSR J1420–6048, which had the longest exposure (net exposure of 70.2 ks) among the available data. For the Rabbit nebula, we

Table 4.11: Journal of the Chandra and XMM-Newton observations of Kookaburra.

Satellite	Chandra	XMM-Newton
Observation ID	7640	0151100201
Start time (UT)[1]	2007/06/14 21:30	2003/03/10 11:56
End time (UT)[1]	2007/06/15 17:55	2003/03/10 19:30
Aim point R.A. (J2000.0)	$14^{\rm h}18^{\rm m}39^{\rm s}.8$	$14^{\rm h}18^{\rm m}39^{\rm s}.8$
Aim point Decl. (J2000.0)	$-60°57'56''$	$-60°58'03''$
Net exposure (ks)	70.2	24.6

[1] Time form of yyyy/mm/dd hh:mm

analyzed an XMM-Newton observation, which was rather short but enough for this study. We used the standard processed and filtered event data for both observations. The journal of these observations are summarized in table 4.12.

4.4.3 Analysis & Results

X-ray Image around PSR J1420–6048

Figure 4.21 (top) shows the exposure-corrected log-scaled ACIS-S3 field image around PSR J1420–6048 in the 2.0–7.0 keV band smoothed with a Gaussian function of $\sigma = 5''.9$. Green and yellow crosses indicate the position of the pulsar and the best-fit center of the VHE γ-ray emission, respectively. The size of the yellow cross indicates the uncertainty of the center. Figure 4.21 (bottom) shows the 1-dimensional profile of the surface brightness along the NW to SE direction, calculated using the data from the green box in figure 4.21 (top). We fitted the profile with a Gaussian function plus a constant model. We ignored bins near the pulsar for the fit. Constant and the Gaussian center were also set free in addition to the Gaussian width and normalization. The best-fit Gaussian width was found to be $\sigma = 1'.5 \pm 0'.4$.

X-ray Image around the Rabbit nebula

Figure 4.22 (top) shows the combined image of the entire MOS 1 and MOS 2 fields around the Rabbit nebula in the 2.0–12.0 keV band smoothed with a Gaussian function of $\sigma = 6''$. Vignetting is not corrected. A green cross in this image indicates the position of the pulsar in the Rabbit nebula. Figure 4.22 (bottom) shows the 1-dimensional profile of the surface brightness along the east to west direction, which coincides the major-axis of the X-ray emission. The profile was calculated with the data in the green box in figure 4.22 (top). We ignored bins near the pulsar for the fit with a Gaussian profile. Constant and the Gaussian center were set free during

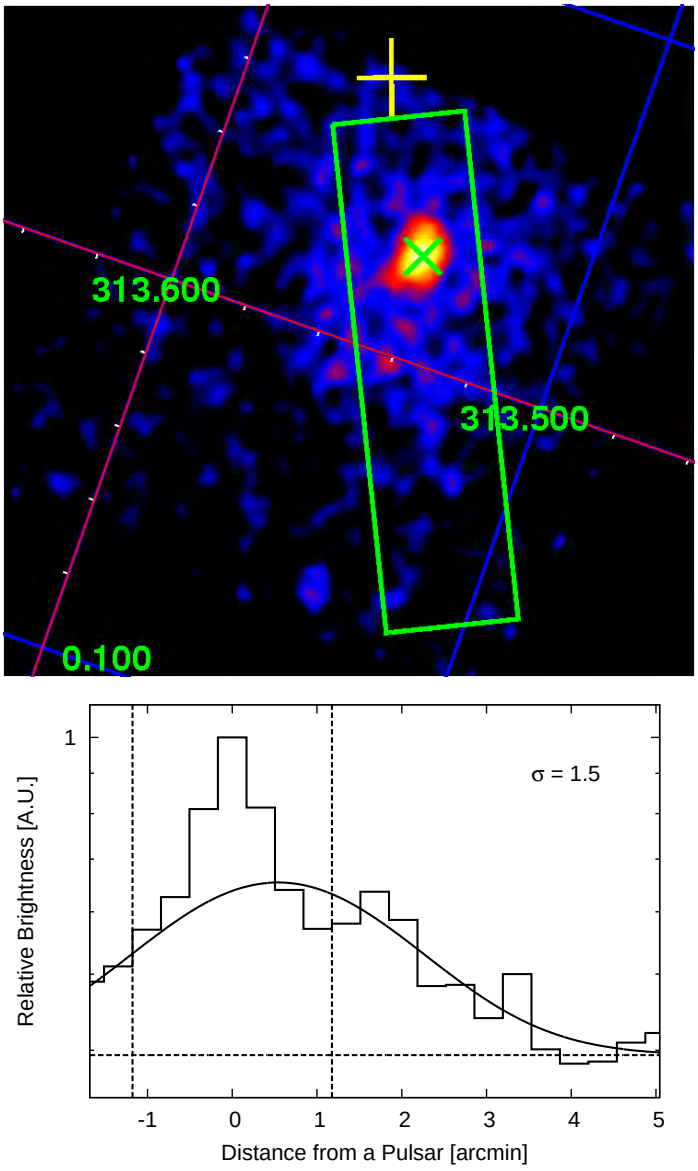

Figure 4.21: Top: Chandra ACIS-S3 image in equatorial coordinate around PSR J1420–6048 in the 2.0–7.0 keV band. The image is smoothed with a Gaussian function of $\sigma = 6''$. The pseudo-color represents vignetting corrected, log-scaled intensity levels. Green and yellow crosses indicate the position of the PSR J1420–6048 and the best-fit center of the VHE γ-ray emission, respectively. The size of the yellow cross represents statistical uncertainty of the center. Bottom: normalized 1-dimensional profile of the surface brightness calculated from the data in the green box (top panel). The bin size of the profile is $14''$. Solid and dashed lines show the best-fit Gaussian profile and a constant, respectively. Bright region near the pulsar was ignored in the fit ($2'.1$ wide, inner part between the two vertical dashed lines).

the fitting in addition to the Gaussian width and the normalization. The best-fit Gaussian width was found to be $\sigma = 1'.8 \pm 0'.3$.

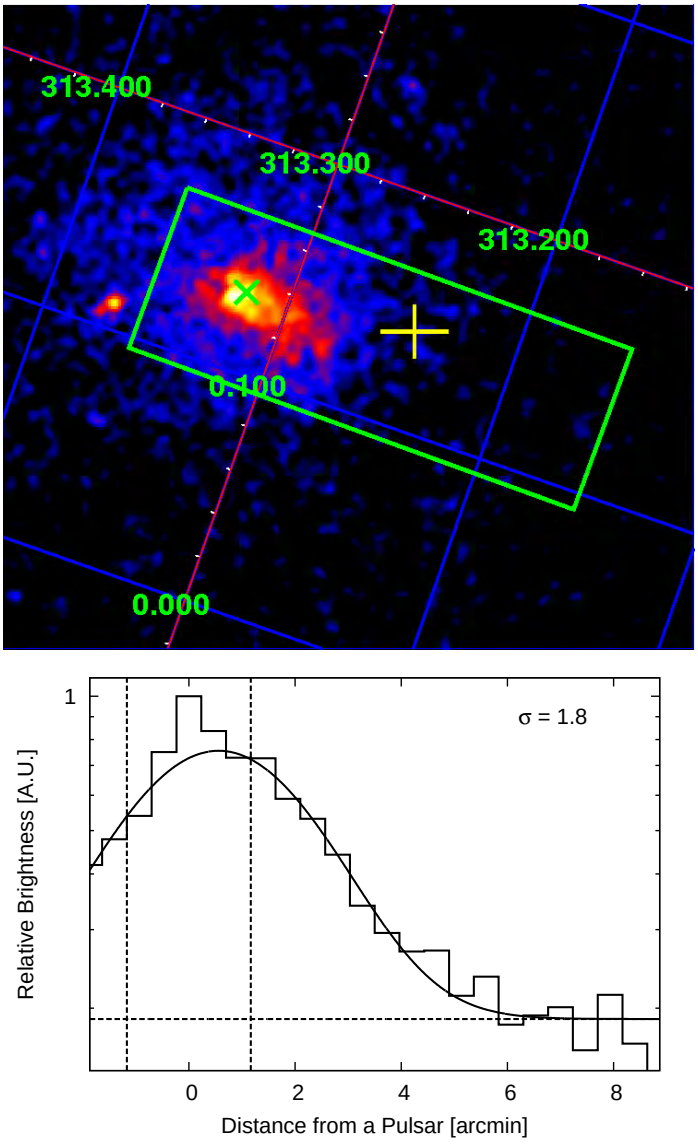

Figure 4.22: Top: XMM-Newton MOS 1 and MOS 2 combined image around the Rabbit nebula in the 2.0–12.0 keV band. The image is smoothed with a Gaussian function of $\sigma = 6''$ and is displayed in log scale. Green and yellow crosses indicate the position of the pulsar and the best-fit center of the VHE γ-ray emission, respectively. The size of the yellow cross represents the uncertainty of the center. Bottom: normalized 1-dimmensional profile of the surface brightness calculated from the data in the green box in the top panel. The profile is binned with a spatial size of $28''$. Solid and dashed lines show the best-fit Gaussian profile and a constant, respectively. Bright part near the pulsar was ignored in this fit ($2'.3$ wide, inner region between the two vertical dashed lines).

4.5 Vela X

4.5.1 Previous Observations

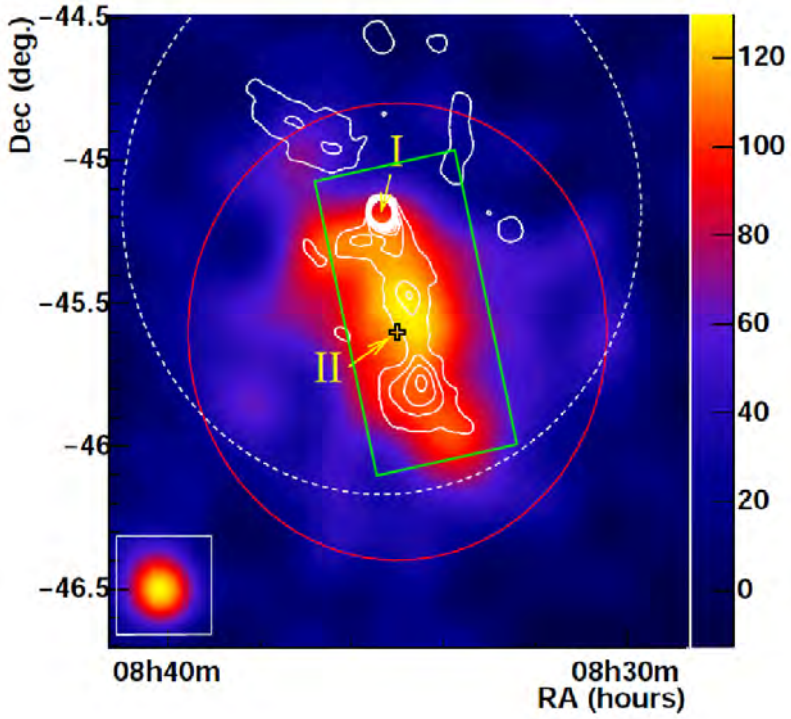

Figure 4.23: A HESS excess map in the sky region surrounding the Vela pulsar smoothed with a radius of 0°.09. The Vela pulsar is indicated as position I. The white contours show the X-ray image obtained by ROSAT. The solid circle represents the HESS integration region for the spectral analysis, while the dashed circle represents the field of view of the ROSAT observations. The inset in the bottom left corner indicates the PSF of HESS. See the caption of figure 4.25 for the green rectangle. This image is adapted from Aharonian et al. (2006b).

The Vela SNR, at a distance of $\sim$ 290 pc (Dodson et al., 2003), is composed of complex regions containing a number of sources of non-thermal radio emission, including those designated by Rishbeth (1958) as Vela X, Vela Y, Vela Z. The Vela pulsar, or PSR B0833–45, is located in the Vela X region at the position of (RA, Dec) = ($08^{\rm h}35^{\rm m}20^{\rm s}.6$, $-45°10'35''$). The pulsar has a period of 89 ms and a period derivative of 1.25×10^{-13} s s^{-1}. The characteristic age and the spin-down luminosity are $\tau = 11$ kyr and $\dot{E} = 6.3 \times 10^{36}$ ergs s^{-1}, respectively. The surface magnetic field is estimated as $B_{\rm s} = 3.1 \times 10^{12}$ Gauss.

The observations of the Vela region by HESS in 2004 and 2005 detected a strong

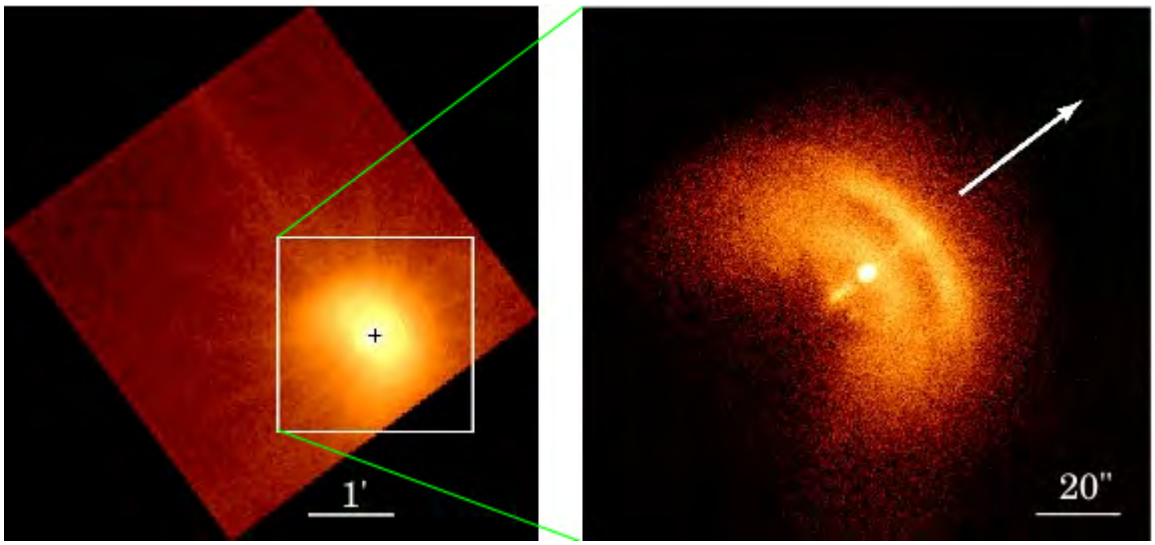

Figure 4.24: Left: An EPIC pn image of the Vela pulsar in equatorial coordinate. The black cross marks the pulsar position. White box marks the region covered by the Chandra image of the right figure. Right: A Chandra HRC image of the Vela pulsar. White arrow indicates the direction of the pulsar's proper motion. These images are adapted from Manzali et al. (2007).

signal from an extended region including the Vela pulsar at the north edge (Aharonian et al., 2006b). The HESS image is shown in figure 4.23. The extent and position of the excess was determined by fitting a two dimensional, elongated Gaussian, convolved with the point spread function of the instrument. The best-fit intrinsic width along the major axis is $0°.48 \pm 0°.03$, while that along the minor axis is $0°.36 \pm 0°.03$. The best-fit center of gravity of the emission region is (RA, Dec) = ($08^{\rm h}35^{\rm m}01^{\rm s}$, $-45°34'40''$), which is indicated as position II in figure 4.23. Position II is $\sim 25'$ offset from the position of the Vela pulsar. The spectrum was extracted from the integration region of a radius of $0°.8$ surrounding position II (indicated as a solid circle in figure 4.23). The spectrum was well reproduced by a power law function with a photon index of $\Gamma = 1.45 \pm 0.09_{\rm stat} \pm 0.2_{\rm sys}$ and an exponential cutoff at $13.8 \pm 2.3_{\rm stat} \pm 4.1_{\rm sys}$ TeV. The flux in the 1–10 TeV was $(5.5 \pm 1.8) \times 10^{-11}$ ergs cm^{-2} s^{-1}.

Observations of the Vela pulsar with Einstein in the 0.1–4.5 keV band showed that it was embedded in a nebula of $2'$ size, which emitted a power-law spectrum with a photon index $\gamma = 1.7 \pm 0.2$ (Harnden et al., 1985). The Vela PWN was further studied in soft X-rays with EXOSAT in the 0.03–2.4 keV band (Oegelman & Zimmermann, 1989) and ROSAT in the 0.9–2.0 keV band (Markwardt & Ogelman, 1995). The ROSAT image is shown in figure 4.23 as white contours, which shows extended shape to the southeast of the pulsar. Chandra observation resolved a toroidal morphology of the X-ray nebula surrounding the pulsar along with a jet, which is similar to that

observed in the Crab Nebula (Helfand et al., 2001; Pavlov et al., 2001). Figure 4.24 shows the XMM-Newton pn (left) and Chandra HRC (right) images. The unabsorbed 1–8 keV flux was determined as $F_X = (5.77 \pm 0.04) \times 10^{-11}$ ergs cm^{-2} s^{-1} with the data from the whole pn field of view assuming an absorbed power-law emission. Dodson et al. (2003) measured the proper motion of the Vela pulsar using radio observation. The transverse velocity measured was 61 ± 2 km s^{-1} and the moving direction was just along the spin axis indicated in figure 4.24.

4.5.2 Observations

Because Vela PWN has a large angular extension in the VHE γ-ray band, X-ray observations also need to cover the whole extension. In addition, high quantum efficiency in the hard X-ray energy band is required to study the non-thermal X-ray emission. ASCA GIS satisfies these criteria and in fact archive data of mapping observations are available. We used ASCA GIS archive with sequence numbers of 50021000, 50021010, 50021020, 50021030, 23043000, 23043010, and 25038000. The data were acquired from 1993 through 1997. After the standard data screening[11], net exposures of these observations were $\sim$15 ks on average.

4.5.3 Analysis & Results

X-ray Image

Figure 4.25 (right) shows the exposure corrected, Gaussian smoothed ASCA GIS image in the 2–8 keV band[12]. Largely extended hard tail is seen in the direction similar to that of the HESS excess. The shape of this image is different from that of the ROSAT image shown as white contours in figure 4.23. This is because the difference of the energy band; ROSAT covered softer X-ray band (0.9–2.0 keV) than than that of ASCA shown here. We calculated a linear profile of the surface brightness using the data encircled by the green rectangle shown in figure 4.25 (top). The result is shown in figure 4.25 (bottom). The horizontal scale represents a distance from the Vela pulsar. We fitted the profile with a model of a Gaussian plus a constant. A constant was fixed to the brightness of the south edge, while a Gaussian center was set free. ASCA image was widely contaminated by the stray light from the bright source. In order to exclude this effect, we ignored bins in the region of $12'$ wide including the pulsar, which was larger than that of other observations in this thesis, from the fit (inner region between the two vertical dashed lines in figure 4.25). The best-fit rms width of the Gaussian profile was found to be $\sigma = 23'.5 \pm 2'.6$.

[11] see http://adfwww.gsfc.nasa.gov/asca/processing_doc/proc/rev2/latest/screen.html
[12] Provided by Koji Mori

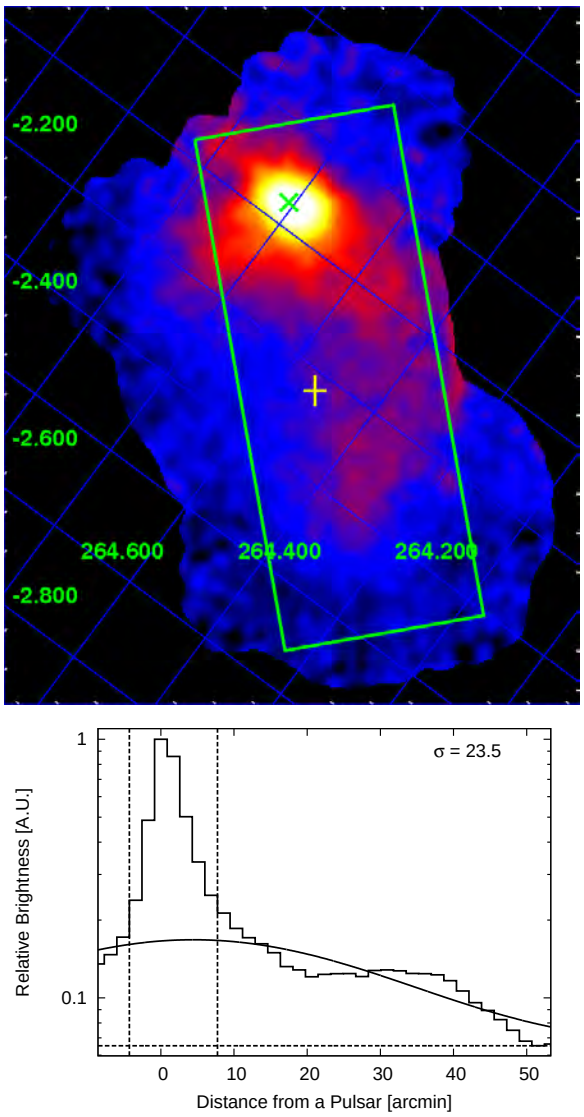

Figure 4.25: Top: Exposure corrected, Gaussian smoothed ASCA GIS image in the 2–8 keV band in the Galactic coordinate. Green and yellow crosses indicate the position of the Vela pulsar and the best-fit center of the VHE γ-ray emission. respectively. The size of the latter represents the fitting error. This image was supplied by Koji Mori at the University of Miyazaki by his courtesy. Bottom: A 1-dimensional profile (bin size $1'.7$) of the surface brightness along the direction from north to south calculated using the data enclosed by the green rectangle in the top figure. Solid line represents the best-fit model of a Gaussian plus a constant; the constant was fixed to the brightness of the south edge (indicated with a dashed line). Bright part near the pulsar was ignored in this fit ($12'$ wide, inner part between the two vertical dashed lines).

4.6 MSH 15–52

4.6.1 Previous Observations

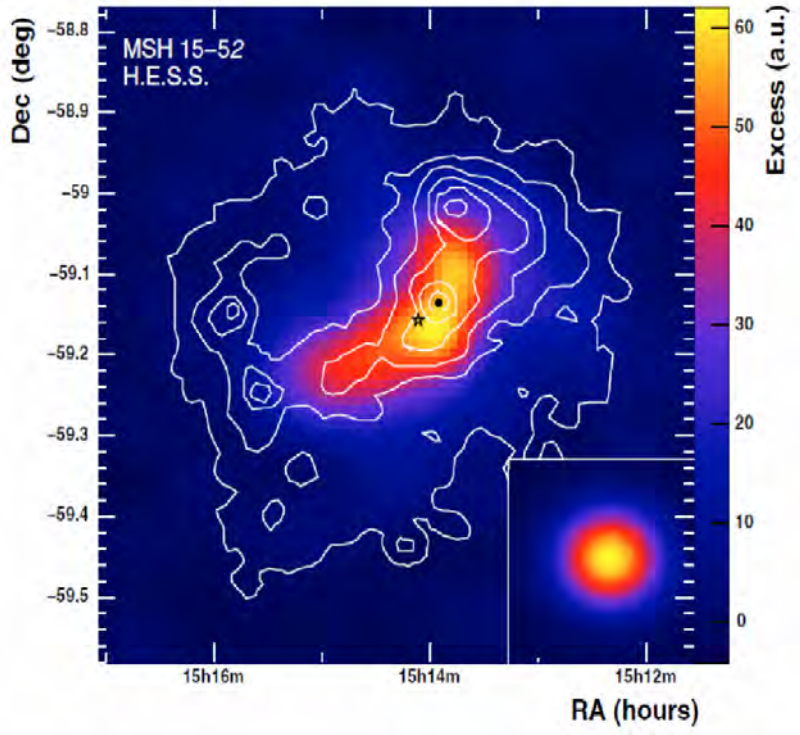

Figure 4.26: HESS excess map smoothed with a radius of 0°.04 around MSH 15–52 adopted from Aharonian et al. (2005c). The white contours denote the X-ray image measured by ROSAT. The black dot and black star indicate the pulsar position and the excess center, respectively. The right-bottom inset shows the PSF smoothed in the same way as the excess map.

The MSH 15–52 is a composite SNR, containing a 150 ms pulsar (PSR B1509–58) with a period derivative of $\dot{P} = 1.54 \times 10^{-12}$ s s^{-1}. The pulsar is located at the position of (RA, Dec) = ($15^{\rm h}13^{\rm m}55^{\rm s}.6$, $-59°08'09''$). The distance to the pulsar was estimated as $d = 4.2$ kpc from its dispersion measure based on the NE2001 Galactic electron-density model (Cordes & Lazio, 2002). The characteristic age and the spin-down luminosity of the pulsar are $\tau = 1.6$ kyr and $\dot{E} = 1.8 \times 10^{37}$, respectively. The surface magnetic field is estimated as $B_{\rm s} = 1.6 \times 10^{13}$ Gauss.

The existence of PWN is confirmed by ASCA (Tamura et al., 1996) and ROSAT (Trussoni et al., 1996) as an extended emission region surrounding the pulsar with a power-law photon index of $\sim$ 2.0. Trussoni et al. (1996) observed MSH 15–52 and revealed an elongated structure centered on the pulsar with two arms extending

Table 4.12: Journal of the Chandra observations of MSH 15–52.

Observation ID	5534
Start time (UT)[1]	2004/12/28 10:27
End time (UT)[1]	2004/12/29 01:00
Aim point R.A. (J2000.0)	$15^{\rm h}13^{\rm m}55^{\rm s}.6$
Aim point Decl. (J2000.0)	$-59°08'09''$
Net exposure (ks)	49.5

[1] Time form of yyyy/mm/dd hh:mm

several arcminutes along the NW and SE directions. Chandra resolved its complicated structures (Gaensler et al., 2002; DeLaney et al., 2006). Diffuse X-ray emission was observed around PSR B1509–58, which was consistent with that seen by ASCA and ROSAT. Jet-like feature was found to the southeast of the pulsar, and two arcs were resolved to be located approximately $17''$ and $40''$ from the pulsar. Gaensler et al. (2002) found the spectrum of the diffuse PWN was well fitted with an absorbed power-law model. The best-fit spectral parameters were as follows: an absorbing column was $N_{\rm H} = (9.5 \pm 0.3) \times 10^{21}$ cm^{-2} and a photon index $\Gamma = 2.05 \pm 0.04$. The total flux of the PWN, corrected for absorption, including the pulsar, jet and arcs was $(37 \pm 2) \times 10^{-12}$ ergs cm^{-2} s^{-1} in 2–10 keV band.

HESS observed MSH 15–52 and detected significant signal from this source centered at the position of (RA, Dec) = ($15^{\rm h}14^{\rm m}7^{\rm s}$, $-59°9'27''$) Aharonian et al. (2005c). The smoothed excess map is shown in figure 4.26. An extended emission is seen along the jet of the pulsar in the NW-SE direction. Assuming an elongated 2-D Gaussian brightness profile, the best-fit intrinsic widths along the major and minor axis were determined as $6'.4 \pm 0'.7$ and $2'.3 \pm 0'.5$, respectively. The spectrum extracted from the data within a radius of $0°.3$ around the image center (i.e. center of the best-fit Gaussian) was found to show a power-law shape with a photon index of $\Gamma = 2.3$. The flux in the 1–10 TeV band was 16×10^{-12} ergs cm^{-2} s^{-1}.

4.6.2 Observations

We analyzed the Chandra archival data, which covered the sky region including the PSR B1509–58. This was the longest observation available now. We used the standard processed and filtered event data. The journal of observation is summarized in table 4.12.

4.6.3 Analysis & Results

X-ray Image

Figure 4.27 (top) shows the entire image covered by the 4 CCD of ACIS-I in the 2.0–7.0 keV band smoothed with a Gaussian of $\sigma = 3''$. Green and yellow crosses indicate the position of PSR B1509–58 and the center of the HESS excess, respectively. The size of the latter cross represents fitting error. A complex structure is seen around the pulsar in the figure, including long elongated jet to the south. Few PWNe in our samples show such a complex structure. When we analyze the extension of the non-thermal diffuse emission, it is necessary to avoid such a complex structure. Even under such circumstance, it is possible to adopt a consistent method as that used for other sources, i.e. 1-dimensional projection of the surface brightness. We carefully selected the positional angle of the rectangle region, which was used to calculate 1-dimensional brightness distribution. The rectangle region is shown in the figure in green. We chosen the box along the NE to SW direction, which is perpendicular to the jet. Figure 4.27 (bottom) shows the 1-dimensional profile of the surface brightness distribution calculated from the data in the red rectangle. We fitted the profile with model of a Gaussian plus a constant. The constant value was set free, while the Gaussian center was fixed at the pulsar's position. We ignored bins near the pulsar in the fit ($2'.1$ wide, inner region between the two vertical dashed lines in figure 4.27). The best-fit Gaussian width was found to be $\sigma = 1'.6 \pm 0'.1$.

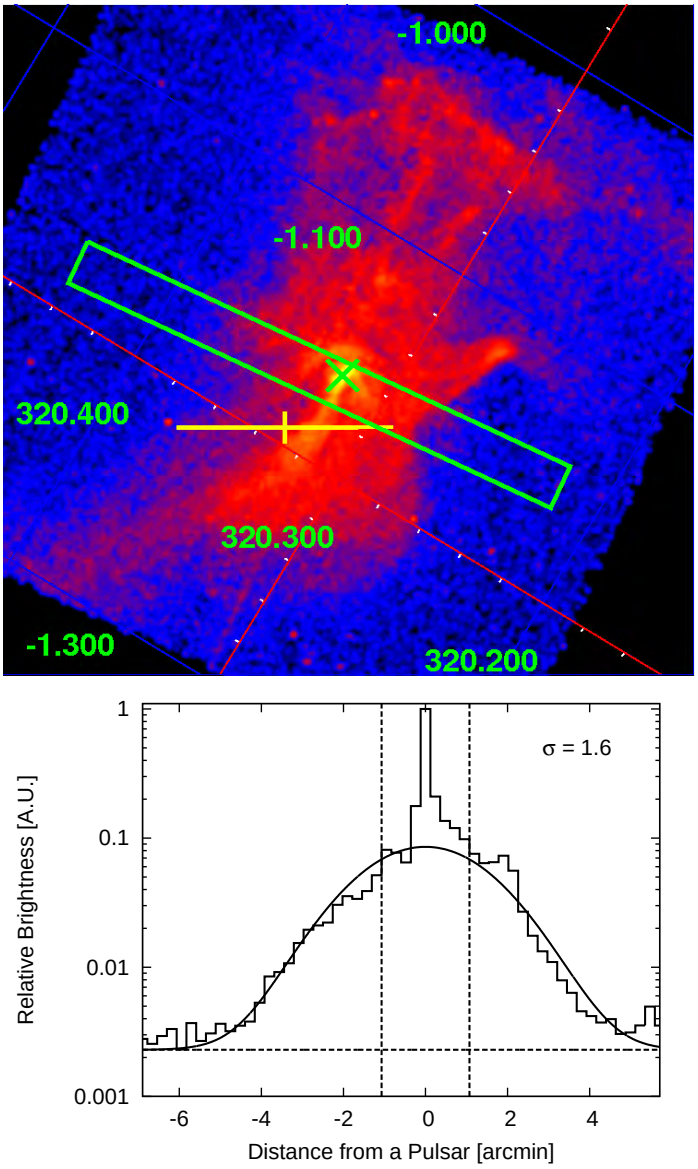

Figure 4.27: Top: Chandra ACIS-I image (2.0–7.0 keV) around MSH 15–52 in Galactic coordinate. The image is smoothed with a Gaussian of $\sigma = 3''$. The pseudo-color represents exposure corrected, log-scaled intensity levels. Green and yellow crosses indicate the pulsar position and the best-fit position of the VHE γ-ray emission. The size of the latter cross represents the fitting error. Bottom: A 1-dimensional profile (bin size of $14''$) of the surface brightness calculated from the data in the green rectangle in the top panel. Solid and dashed lines show the best-fit Gaussian and a constant, respectively. Bright region near the pulsar was ignored in the fit ($2'.1$ wide, inner region between the two vertical dashed lines).

4.7 G21.5–0.9 & Kes 75

4.7.1 Previous Observations

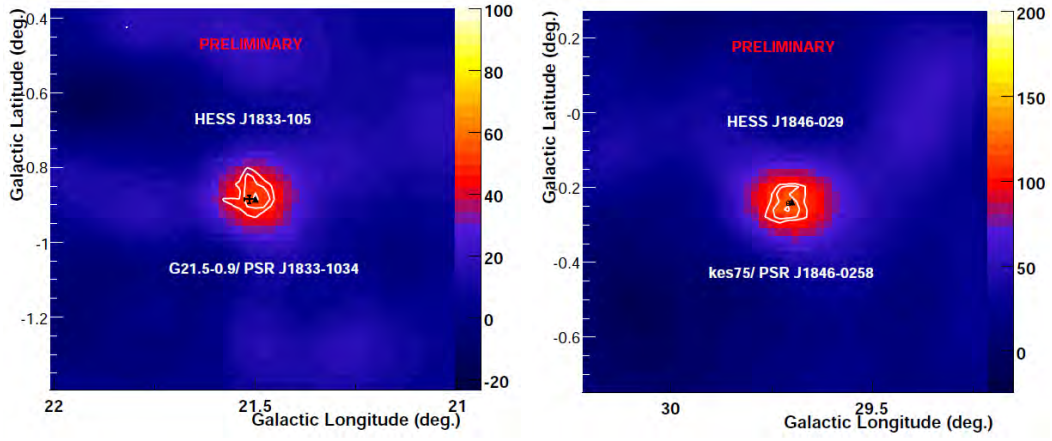

Figure 4.28: HESS excess maps (smoothed with a circle of 0°.08) for the 0.5° × 0.5° fields around HESS J1833–105 (or G21.0–0.9; left) and HESS J1846–029 (or Kes 75; right), adapted from H. E. S. S. Collaboration: A. Djannati-Atai et al. (2007). The white contours show the pre-trials significance levels of 4, 5, 6σ and 7, 8, 9σ, respectively, for the left and right panels. The black triangle marks the position of the pulsars. The best-fit positions of the two sources are marked as crosses.

G21.5–0.9 and Kes 75 are the PWNe which contain Crab-like young and energetic pulsars. HESS Galactic plane survey during 2005–2007 has revealed point-like sources, HESS J1833–105 and HESS J1846–029, at the position of (RA, Dec) = ($18^{\rm h}33^{\rm m}32^{\rm s}.5$, $-10°33'19''$) and ($18^{\rm h}46^{\rm m}24^{\rm s}.1$, $-02°58'53''$) with the extensions compatible with a point-like sources, which are positionally coincident to G21.5–0.9 and Kes 75, respectively. The excess map of HESS is shown in figure 4.28 (H. E. S. S. Collaboration: A. Djannati-Atai et al., 2007). The energy spectra of the two sources were reproduced with a power-law model of a photon indices of $2.08 \pm 0.22_{\rm stat} \pm 0.1_{\rm sys}$ and $2.26 \pm 0.15_{\rm stat} \pm 0.1_{\rm sys}$ for HESS J1833–105 and HESS J1846–029, respectively. The fluxes in the 1–10 TeV are 1.5×10^{-12} ergs cm^{-2} s^{-1} and 1.7×10^{-12} ergs cm^{-2} s^{-1} for HESS J1833–105 and HESS J1846–029, respectively (Gallant et al., 2008).

G21.5–0.9, discovered during the survey in the radio band (Altenhoff et al., 1970), is a composite SNR consisting of a centrally peaked PWN and a shell. The structure was revealed by the Chandra observation reported by Slane et al. (2000). The spectrum of the PWN was reproduced with a power-law model of a column density of $N_{\rm H} = (2.24 \pm 0.04) \times 10^{22}$ cm^{-2} and a photon index of $\Gamma = 1.91 \pm 0.04$. The unabsorbed flux in the 2–10 keV band was $F_X = 4.6 \times 10^{-11}$ ergs cm^{-2} s^{-1}. PSR J1833–1034 was

discovered at the center of the PWN (Gupta et al., 2005; Camilo et al., 2006). It is a 61.9 ms radio pulsar with a period derivative of $\dot{P} = 2.02 \times 10^{-13}$ s s^{-1}. The distance to the pulsar was determined as $d = 4.3$ kpc from its dispersion measure based the NE2001 Galactic electron-density model (Cordes & Lazio, 2002). The characteristic age is $\tau = 4.9$ kyr and the spin-down luminosity is $\dot{E} = 3.4 \times 10^{37}$ ergs s^{-1}, which is the second most energetic pulsar known in Galaxy. The surface magnetic field was estimated as $B_{\rm s} = 4.0 \times 10^{12}$ Gauss.

Kes 75 is also a composite SNR with a central core. At the center of the PWN is located a 326 ms pulsar PSR J1846–0258 with the period derivative of $\dot{P} = 7.1 \times 10^{-12}$ s s^{-1}. The distance to the pulsar was estimated as $d = 5.2$ kpc from its dispersion measure based on the NE2001 Galactic electron-density model (Cordes & Lazio, 2002). The pulsar is very young with the characteristic age of only 723 yr, which is the youngest pulsar yet discovered, and has a very large surface magnetic field of 4.9×10^{13} Gauss with the spin-down luminosity of $\dot{E} = 8.1 \times 10^{36}$ ergs s^{-1}. ASCA revealed the presence of thermal and nonthermal spectral components of Kes 75 (Blanton & Helfand, 1996). Helfand et al. (2003) resolved the shell structure and discovered a neutron star embedded in an axisymmetric PWN with complex morphology with Chandra. They extracted the spectrum of the PWN and fitted with a power-law, yielding the absorption column of $N_{\rm H} = (3.96 \pm 0.08) \times 10^{22}$ cm^{-2} and a photon index of $\Gamma = 1.92 \pm 0.04$. The unabsorbed flux including the emission from the central pulsar in the 2–10 keV band was $F_X = 2.8 \times 10^{-11}$ ergs cm^{-2} s^{-1}.

4.7.2 Observations

G21.5–0.9 is a calibration target of Chandra, and relatively large number of observations is available. We used six sets of observations with the target placed within $10'$ of the optical axis of the telescope and falling on ACIS S3. We used the standard processed and filtered event data. Combining all six sets of data, the total net exposure was 60 ks after the filtering. For Kes 75, we analyzed the Chandra archival data observed in 2006, which is the longest observation available at this time. We used the standard processed and filtered event data. After the filtering, the total net exposure was 54 ks. The journal of these observations are summarized in table 4.13.

4.7.3 Analysis & Results

X-ray Image around G21.0–0.9

We generated G21.0–0.9 image in the 2.0–7.0 keV band. Figure 4.29 (top) shows the vignetting-corrected, log-scaled image around G21.0–0.9 smoothed with a Gaussian function of $\sigma = 3''$. Green and yellow crosses show the pulsar position and the best-fit position of the VHE γ-ray emission, respectively. Size of the latter cross

Table 4.13: Journal of the Chandra observations of G21.5–0.9 and Kes 75.

Obs. ID	Start time (UT)[1]	End time (UT) [1]	Aim point (R.A., Decl.) J2000.0	Net exp. ks
G21.5–0.9				
1433	1999/11/15 22:32	1999/11/16 03:12	($18^h33^m34^s.4$, $-10°35'24''$)	15.0
1553	2001/03/18 09:40	2001/03/18 12:57	($18^h33^m33^s.8$, $-10°32'51''$)	9.7
1554	2001/07/21 18:31	2001/07/21 21:37	($18^h33^m30^s.8$, $-10°35'11''$)	9.1
1717	2000/05/23 09:25	2000/05/23 11:47	($18^h33^m32^s.1$, $-10°32'53''$)	7.5
2873	2002/09/14 01:10	2002/09/14 04:34	($18^h33^m33^s.0$, $-10°35'21''$)	9.8
3474	2002/05/16 08:13	2002/05/16 11:24	($18^h33^m45^s.7$, $-10°27'45''$)	9.3
Kes 75				
6686	2006/06/07 20:28	2006/06/08 12:09	($18^h46^m24^s.9$, $-02°58'30''$)	54.1

[1] Time form of yyyy/mm/dd hh:mm

represents the fitting error. Figure 4.29 (bottom) shows the linear profile of the surface brightness calculated from the data enclosed by the green rectangle indicated in the top panel. The position angle of the rectangle was determined to avoid the northern bright spot (the "North Spur", designated by Bocchino et al. (2005)) and the eastern bright limb (Matheson & Safi-Harb, 2005), both of which are originated from the SNR surrounding the PWN. We fitted the profile with a model of a Gaussian plus a constant. We ignored bins near the pulsar for $\sim 2'$ wide in the fit. The best-fit Gaussian width was found to be $\sigma = 0'.72 \pm 0'.04$.

X-ray Image around Kes 75

Similarly, we generated the image around Kes 75 in the 2.0–7.0 keV band as shown in figure 4.30 (top). The image was vignetting-corrected, log-scaled and smoothed with a Gaussian of $\sigma = 1''.5$. Meaning of the marks is same as that in figure 4.29. Linear profile of the surface brightness distribution calculated with the data enclosed by the green rectangle in the top panel is shown in figure 4.30 (bottom). The position angle of the rectangle was selected to avoid the bright shell seen in the SE and SW of the PWN. We fitted the profile with a model of a Gaussian plus a constant. We ignored bins near the pulsar for $\sim 2'$ wide in the fit with a Gaussian profile. The best-fit Gaussian width was found to be $\sigma = 0'.63 \pm 0'.05$.

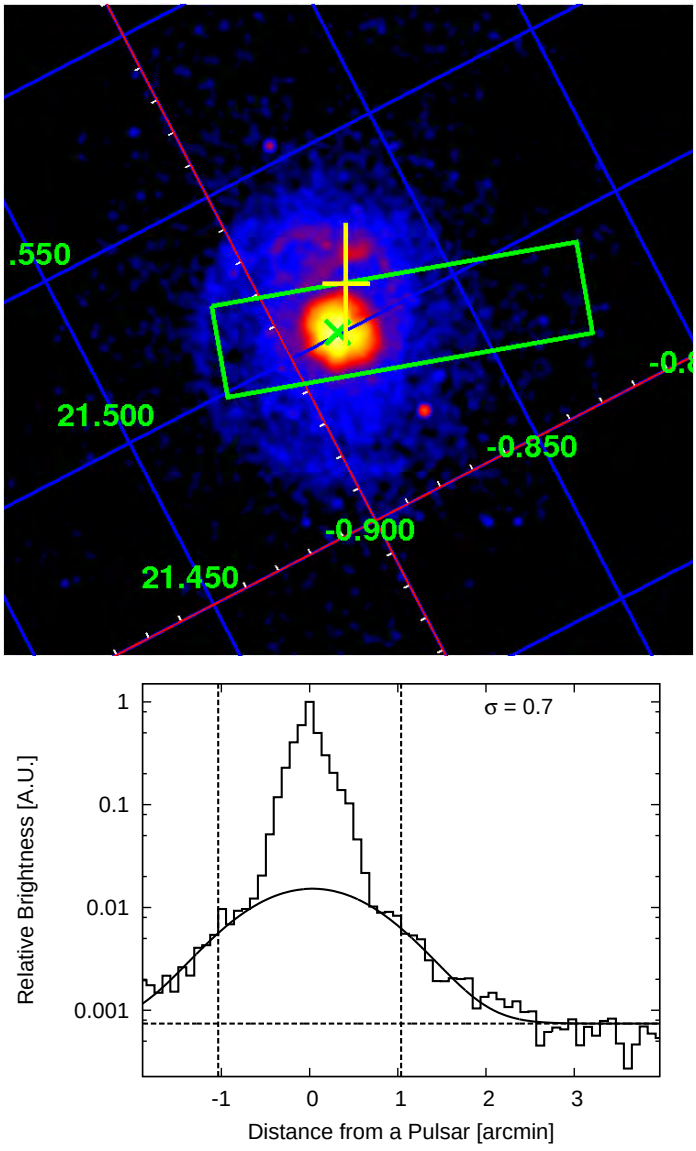

Figure 4.29: Top: Chandra ACIS-S3 image around G21.5–0.9 in Galactic coordinate in the 2.0–7.0 keV band. The image is smoothed with a Gaussian function of $\sigma = 3''$. The pseudo-color represents vignetting corrected, log-scaled intensity levels. Green and yellow crosses indicate the pulsar position and the center of the VHE γ-ray emission, respectively. Size of the latter cross represent the pointing error. Bottom: A 1-dimensional profile (bin size of $5''.4$) of the surface brightness calculated from the data enclosed by the green box in the top panel. Solid and dashed lines show the best-fit Gaussian profile and a constant, respectively. The central core near the pulsar was ignored in this fit ($2'.1$ wide, inner part between the two vertical dashed lines).

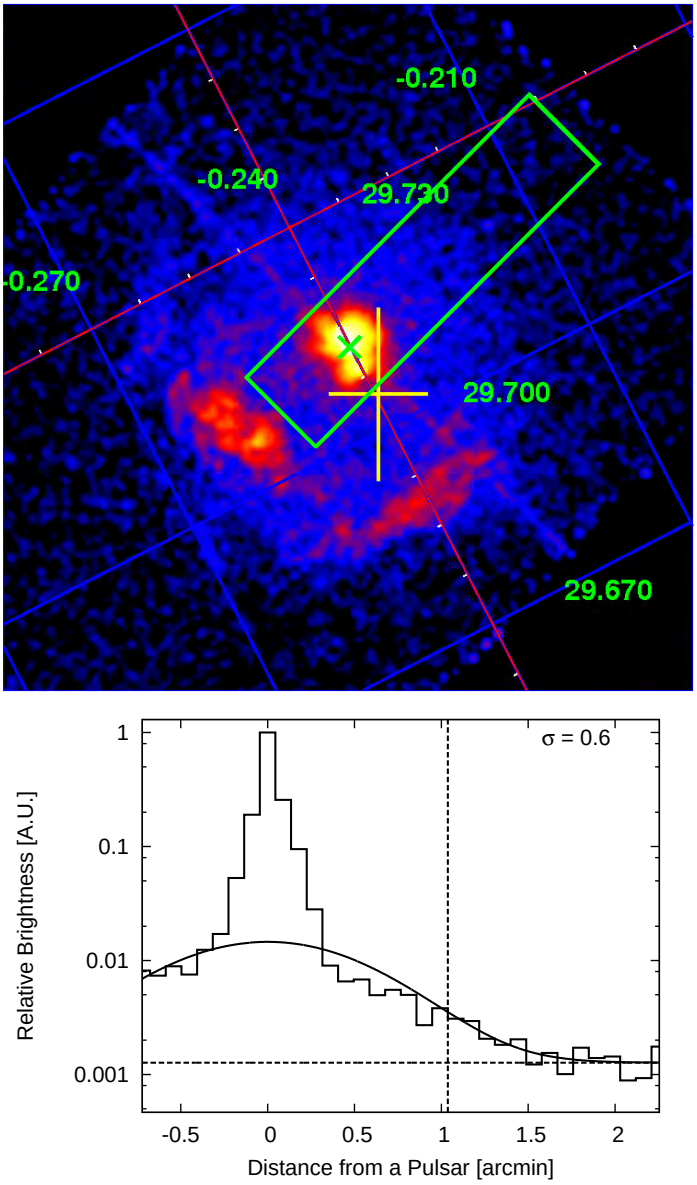

Figure 4.30: Top: Chandra ACIS image around Kes 75 in Galactic coordinate in the 2.0–7.0 keV band. The image is smoothed with a Gaussian function of $\sigma = 1''.5$. The pseudo-color represents vignetting corrected, log-scaled intensity levels. Green and yellow crosses indicate the pulsar position and the center of the VHE γ-ray emission, respectively. Size of the latter cross represents the statistical error of position. Bottom: A 1-dimensional profile (bin size of $5''.4$) of the surface brightness calculated from the data enclosed in the green rectangle in the top panel. Solid and dashed lines show the best-fit Gaussian and a constant, respectively. The central core near the pulsar was ignored in the fit ($2'.1$ wide, inner part of the vertical dashed line).

4.8 HESS J1718–385

4.8.1 Previous Observations

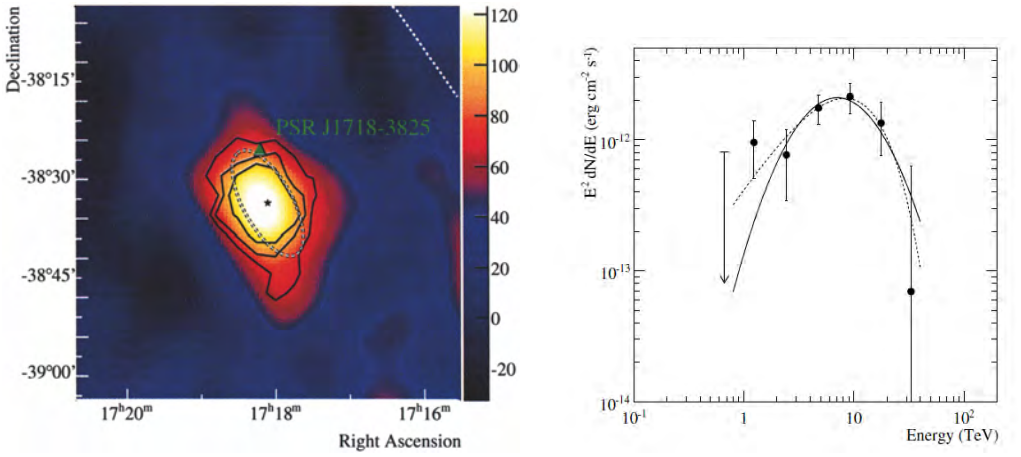

Figure 4.31: Left: smoothed excess map (smoothing radius 3′.8) measured by HESS around HESS J1718–385. The position of the pulsar PSR J1718–3825 is marked with a green triangle, and the Galactic plane is shown as a white dotted line. The best-fit position of the γ-ray source is marked with a black star and the fit ellipse with a dashed line. Right: An energy spectrum of HESS J1718–385, fitted by a curved profile (solid line) and a power-law with an exponentially cut-off (dashed line). The softest data point in the spectrum lacks statistics due to lower exposure at small zenith angle and is plotted as a 2σ upper limit. These figures are adapted from Aharonian et al. (2007).

HESS J1718–385 was discovered in the deep observations of the supernova remnant RX J1713.7–3946 using HESS in 2004–2005 (Aharonian et al., 2007). The excess map is shown in figure 4.31 (left). Assuming a two-dimensional Gaussian brightness profile, the best-fit position of the excess center was determined as (RA, Dec) = ($17^{\rm h}18^{\rm m}7^{\rm s}$, $-38°33'$). The intrinsic widths of the extent were found to be $9' \pm 2'$ for the major axis and $4' \pm 1'$ for the minor axis, respectively. The energy spectrum is shown in figure 4.31 (right). As shown in this figure, the spectrum has a low energy cut-off below 10 TeV. The spectrum is fitted by a curved profile and a power-law with an exponentially cut-off, both of which indicate the peak energy of $\sim$7 TeV. The flux in the 1–10 TeV band was $(2.9 \pm 1.3) \times 10^{-12}$ ergs cm^{-2} s^{-1}. PSR J1718–3825 is a radio pulsar located at (RA, Dec) = ($17^{\rm h}18^{\rm m}13^{\rm s}.6$, $-38°25'18''$), which is offset by $8'$ from the center of HESS J1718–385. Because there is no other possible counterparts to HESS J1718–385, PSR J1718–3825 is believed to be the most plausible counterpart. PSR J1718–3825 is a 74.7 ms radio pulsar with a period derivative of $\dot{P} = 1.32 \times 10^{-14}$ s s^{-1}. The distance to the pulsar was estimated to be $d = 3.6$ kpc from the dispersion mea-

Table 4.14: Journal of the Suzaku observation of HESS J1718–385.

Sequence ID	501105010
Start time (UT)[1]	2007/02/23 08:36
End time (UT)[1]	2007/02/23 18:39
Aim point R.A. (J2000.0)	$17^{\rm h}18^{\rm m}13^{\rm s}.0$
Aim point Decl. (J2000.0)	$-38°36'23''$
Net exposure (ks)	20.7

[1] Time form of yyyy/mm/dd hh:mm

sure of the pulsar based on the NE2001 Galactic electron-density model (Cordes & Lazio, 2002). The characteristic age and the spin-down luminosity of the pulsar are $\tau_c = 90$ kyr and $\dot{E} = 1.3 \times 10^{36}$ ergs s^{-1}, respectively. XMM-Newton observation discovered an X-ray nebula around a point-source positionally coincident with PSR J1718–3825 (Hinton et al., 2007a). For a point-source within a radius of 19″, the spectrum was well fitted with an absorbed power-law model with a photon index of $\Gamma = 1.47 \pm 0.21$, an absorbing column of $N_{\rm H} = 2.9^{+1.4}_{-1.0} \times 10^{21}$ cm^{-2}, and an unabsorbed flux of $F_{\rm X} \sim 1.4 \times 10^{-13}$ ergs cm^{-2} s^{-1} in the 2–10 keV band. The energy spectrum of the diffuse emission in the annulus between the outer radius 60″ and inner radius 19″ could be fit with an absorbed power-law of a photon index of $\Gamma = 1.84^{+0.22}_{-0.13}$ and the column density of $N_{\rm H} = 7.2^{+3.0}_{-0.8} \times 10^{21}$ cm^{-2}. The an unabsorbed flux is estimated as $F_{\rm X} \sim 1.3 \times 10^{-13}$ ergs cm^{-2} s^{-1} in the 2–10 keV band.

4.8.2 Observation

Suzaku observed HESS J1718–385 in Feb, 2007. Three XISs (XIS 0, 1, 3) were operated in the normal clocking mode without the Spaced-row Charge Injection (SCI) (Nakajima et al., 2008). We analyzed the data prepared by the version 2.0 pipeline. We concentrated on the analysis of the XIS data because we were interested in the spatial distribution of the emission. We applied the standard screening criteria to the XIS[13] data to obtain cleaned event lists. After the data screening, the net exposures was 20.7 ks. The net exposure and journal of observations are summarized in table 4.14. We used HEADAS version 6.5 software package for the data analysis of HESS J1718–385.

[13]http://www.astro.isas.jaxa.jp/suzaku/process/v2changes/criteria_xis.html

4.8.3 Analysis & Results

X-ray Image

We extracted the XIS image in 2.0–10.0 keV for each sensor. The data between 5.73–6.67 keV were removed from the image to exclude the calibration sources. We corrected the vignetting effect by dividing the image with that of the flat sky simulated at 4.0 keV using the XRT+XIS simulator `xissim` (Ishisaki et al., 2007). The image was binned by 8×8 pixels and was smoothed with a Gaussian function of $\sigma = 0'.42$. Combined Suzaku XIS (0+1+3) image is shown in figure 4.32.

Figure 4.32 (top) shows the linear profile of the surface brightness calculated from the data in the green rectangle shown in figure 4.32 (bottom). The horizontal scale represents a distance from PSR J1718–3825. We fitted the profile with a model of a Gaussian plus a constant. The constant was set free and the Gaussian center was fixed at the pulsar's position. The best-fit rms width of the Gaussian profile was found to be $\sigma = 4'.2 \pm 0'.5$.

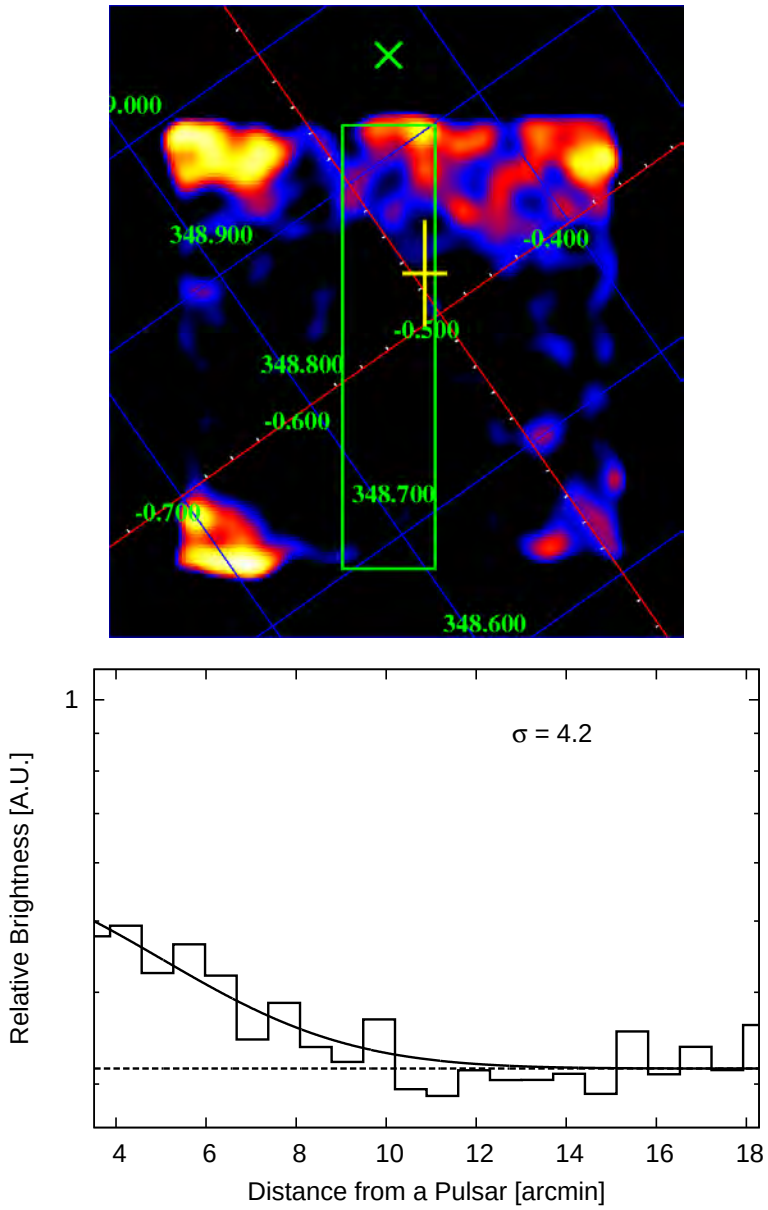

Figure 4.32: Top: Suzaku XIS (0+1+3) image around HESS J1718–385. The data between 5.73–6.67 keV were filtered out to remove the calibration sources. The pseudo-color represents vignetting-corrected, log-scaled intensity levels in the 2.0–10.0 keV band. Green oblique cross indicates the pulsar position. Center of HESS J1718–385 is indicated by a yellow cross, whose size represents the statistical uncertainty of the center. Bottom: A 1-dimensional profile (bin size of 1′) of the surface brightness calculated from the data enclosed by the green rectangle. As shown in the upper panel, position angle of the rectangle was selected to align from north to south. Solid line shows the best-fit Gaussian function, whose center was fixed to 0 (pulsar position) in the fit, and the dashed line the constant model.

4.9 HESS J1616–508

4.9.1 Previous Observations

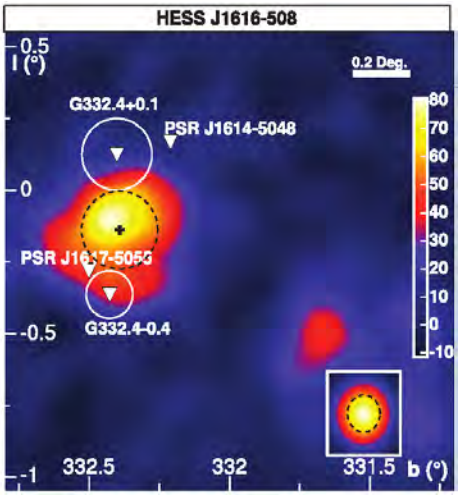

Figure 4.33: Smoothed excess map (smoothing radius 0°.06) of the region surrounding HESS J1616–508. This figure is adapted from Aharonian et al. (2006a).

HESS J1616–508 is a bright VHE γ-ray source as shown in figure 4.33. Assumed a two-dimensional Gaussian brightness profile, the best fit position for the center of the excess was determined as (RA, Dec) = ($16^{\rm h}16^{\rm m}24^{\rm s}$, $-50°53'50''$). The intrinsic width for the fit is $0°.136 \pm 0°.008$. The spectrum is fit with a power-law with a photon index of $\Gamma = 2.1 \pm 0.2_{\rm stat} \pm 0.2_{\rm sys}$. The flux in the 1–10 TeV band is $(4.7 \pm 1.1) \times 10^{-12}$ ergs cm^{-2} s^{-1}. The central region of HESS J1616–508 was observed with Suzaku, but no X-ray counterpart was found (Matsumoto et al., 2007). An energetic pulsar PSR J1617–5055 with a period of 69 ms is located at the edge of the source. The pulsar was firstly identified through its X-ray pulsation with ASCA (Torii et al., 1998) with the radio pulsations found afterwards (Kaspi et al., 1998). Since the ASCA observation, the pulsar has been observed with X-ray satellites. Landi et al. (2007) reported a joined spectral fit to the XMM-Newton, BeppoSAX, and Integral data with a power-law model and obtained the fitting parameters of $\Gamma = 1.4 \pm 0.1$, $N_{\rm H} = (3.9 \pm 0.3) \times 10^{22}$ cm^{-2}, and unabsorbed flux of 4.2×10^{-12} ergs cm^{-2} s^{-1} in the 2–10 keV band, which is close to the other X-ray observations. Recently, Chandra observation revealed the existence of a bright compact pulsar with a faint PWN surrounding the pulsar (Kargaltsev et al., 2008b).

Table 4.15: Journal of the XMM-Newton observation of HESS J1616–508.

Sequence ID	0302390101
Start time (UT)[1]	2005/08/23 07:29
End time (UT)[1]	2005/08/24 07:51
Aim point R.A. (J2000.0)	$16^{\rm h}17^{\rm m}36^{\rm s}.2$
Aim point Decl. (J2000.0)	$-51°02'25''$
Net exposure (ks)	30.5^2 / 25.7^3

[1] time form of yyyy/mm/dd hh:mm
[2] MOS 1
[3] MOS 2

4.9.2 Observation

We analyzed the XMM-Newton archival data around PSR J1617–5055. We used the standard processed and filtered event data of MOS 1 and 2. After the filtering, the net exposure was $\sim$30 ks in average.

4.9.3 Analysis & Results

X-ray Image

Figure 4.34 (top) shows the combined image of entire MOS 1 and MOS 2 field around PSR J1617–5055 in the 2.0–12.0 keV band smoothed with a Gaussian function of $\sigma = 12''$. Vignetting is not corrected. A green cross in this image indicates the position of PSR J1617–5055. Figure 4.34 (bottom) shows the profile of the surface brightness distribution along the Galactic SE to NW direction, which is the major-axis of the X-ray emission, extracted from the enclosed region with a green box in figure 4.34 (top). We fitted the profile with a Gaussian function plus a constant model. Constant was set free and the Gaussian center was fixed at the pulsar's position. We ignored bins near the pulsar for the fit with a Gaussian profile. The best-fit Gaussian width was found to be $\sigma = 1'.8 \pm 0'.5$.

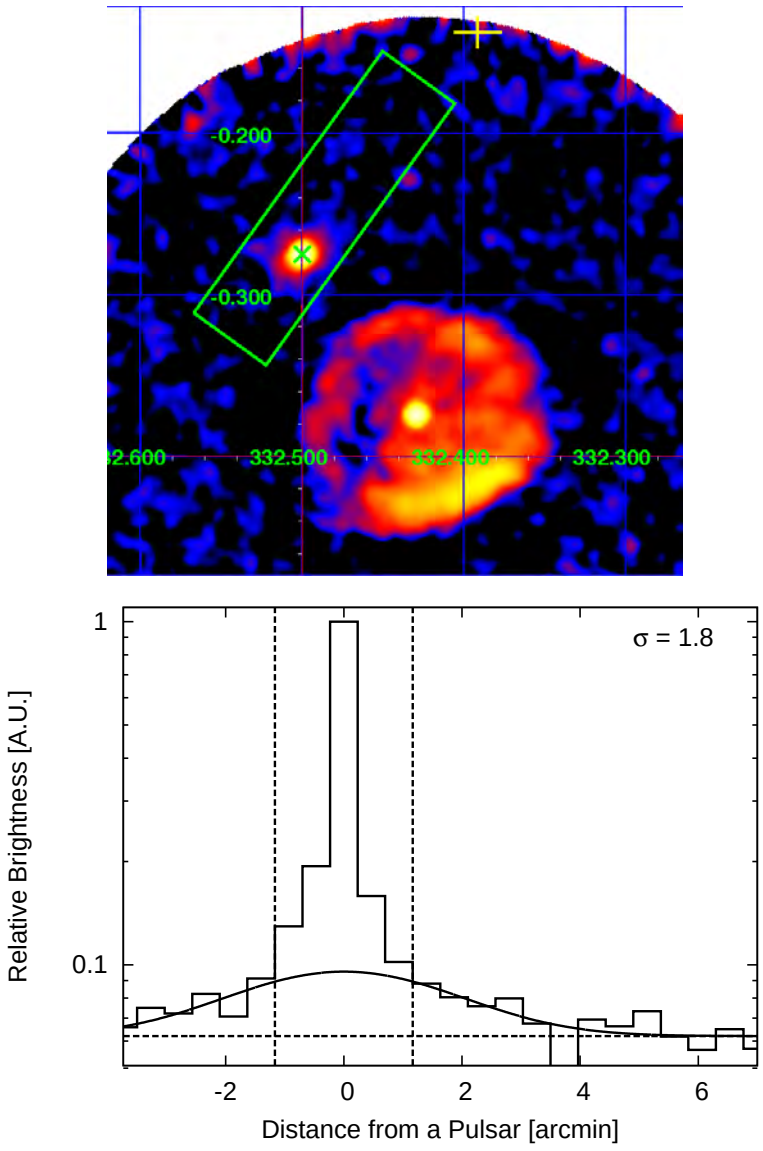

Figure 4.34: Top: XMM-Newton MOS (1+2) image around HESS J1616–508. The pseudo-color represents log-scaled intensity levels in the 2.0–12.0 keV band. Vignetting was not corrected. Green and yellow crosses indicate the pulsar position and the best-fit position of VHE γ-ray emission with the fitting error. SNR G332.4–0.4 is seen at the south. Bottom: A 1-dimensional profile (bin size of 28″) of the surface brightness calculated along the direction from SE to NW from the data in the green rectangle indicated in the top panel. Solid and dashed lines show the best-fit Gaussian and a constant, respectively. Bright region near the pulsar was ignored in this fit (2′.3 wide, inner region between the two vertical dashed lines).

4.10 G0.9+0.1

4.10.1 Previous Observations

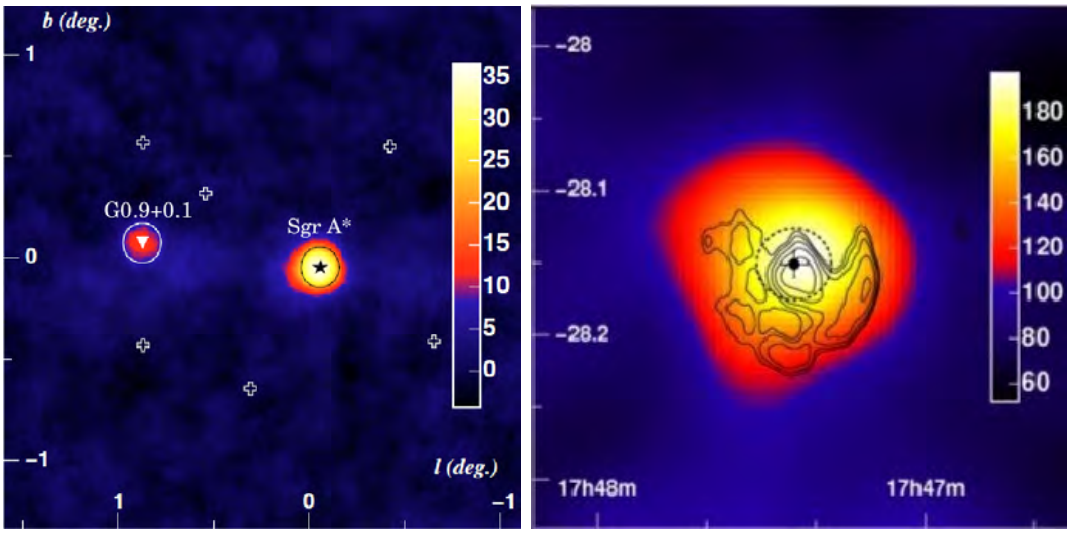

Figure 4.35: Left: HESS significance map for the region around the Galactic center, adapted from Aharonian et al. (2005b). The position of G0.9+0.1 is marked with a triangle and Sgr A* is marked with a star. Right: HESS smoothed excess map of G0.9+0.1 (Color scale), with radio contours superimposed. The cross indicates the best estimate for the location of the TeV source, the dashed circle the limit on the (rms) source size (assuming a Gaussian source distribution). This figure is taken from the web site of the H.E.S.S. collaboration[15].

G0.9+0.1 is a composite supernova remnant. It is known to have a bright compact core ($\sim 2'$ across) surrounded by an $8'$ diameter shell from the radio observation (Helfand & Becker, 1987). Deep HESS observation of the Galactic center region was performed in 2004 and detected significant signals from the core G0.9+0.1. A significance map is shown in figure 4.35. Within the angular resolution of HESS, the source is point-like, with an emission region smaller than $1'.3$ (rms). Because the position of the HESS source is positionally coincident with the central core, rather than the shell, of G0.9+0.1, the VHE γ-ray emission is believed to originate from the PWN The spectrum is fit with a Gaussian function with a photon index of $\Gamma = 2.40 \pm 0.11_{\rm stat} \pm 0.20_{\rm sys}$. The flux in the 1–10 TeV band is $(2.0 \pm 0.5) \times 10^{-12}$ ergs cm^{-2} s^{-1} (Aharonian et al., 2005b).

X-ray observations such as Chandra (Gaensler et al., 2001) and XMM-Newton (Porquet et al. (2003); see figure 4.36) identified the core region as a PWN. However,

[15]http://www.mpi-hd.mpg.de/hfm/HESS/pages/home/som/2005/02/

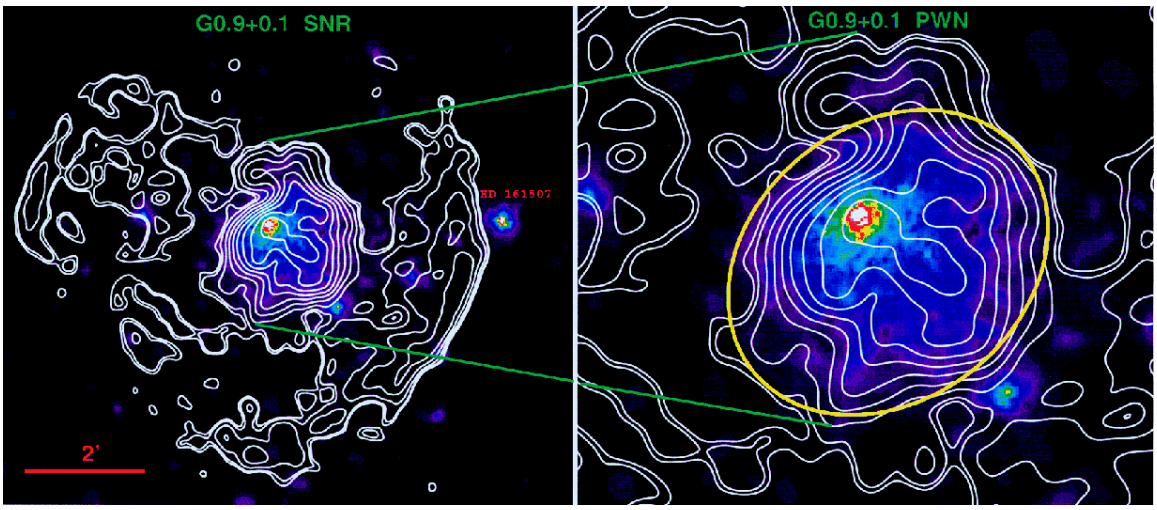

Figure 4.36: XMM-Newton EPIC image of SNR G0.9+0.1 and its PWN in the energy band 1.5-12 keV with Gaussian smooth of 10″. The VLA radio contours at 1.5 GHz (20 cm) are superimposed in white. Left: overall remnant. Right panel: Pulsar Wind Nebula (PWN). The yellow ellipse represents the region taken for spectra analysis of the overall PWN. This figure is adapted from Porquet et al. (2003).

no X-ray pulsation has been detected. Porquet et al. (2003) extracted a spectrum from the region enclosed by the yellow ellipse in figure 4.36 and fitted the spectrum with an absorbed power-law model. The spectrum was well fitted with the absorption column of $N_{\rm H} = 1.47^{+0.14}_{-0.13} \times 10^{23}$ cm^{-2}, the photon index of $\Gamma = 1.99^{+0.19}_{-0.18}$, and the unabsorbed flux (2–10 keV) of $F_X = 5.78 \times 10^{-12}$ ergs cm^{-2} s^{-1}.

4.11 Other VHE PWN Candidates

4.11.1 Previous Observations

The other VHE PWN candidates are HESS J1303-631, HESS J1702–420 and HESS J1804–216. HESS J1303-631 is the first unidentified source found in the HESS Galactic plane survey in 2004 (Aharonian et al., 2005d). The others are unidentified sources found in the survey subsequently (Aharonian et al., 2006a).

HESS J1303-631 was serendipitously found in a dataset which was initially taken on the binary system PSR B1259–63/SS 2883 which was also discovered in the TeV γ-ray band as shown in figure 4.37 (top). Assumed a two-dimensional Gaussian brightness profile, the best fit position for the center of the excess was determined as (RA, Dec) = ($13^{\rm h}03^{\rm m}04^{\rm s}$, $-63°11'55''$). HESS J1303-631 is larger then that expected for a point source. The intrinsic width for the fit is $0°.16 \pm 0°.02$. The spectrum is fit with a power-law with a photon index of $\Gamma = 2.44 \pm 0.05_{\rm stat} \pm 0.2_{\rm sys}$. The flux in the 1–10 TeV band is $(9.9 \pm 2.6) \times 10^{-12}$ ergs cm^{-2} s^{-1}. The only plausible counterpart is PSR J1301–6305, which has enough energy to power the whole of the VHE emission. However, no PWN has been detected from this pulsar (Aharonian et al., 2005d).

HESS J1702–420 is significantly extended compared with the PSF of the HESS telescope as shown in figure 4.37 (middle). Assumed an elongated two-dimensional Gaussian brightness profile, the best fit position for the center of the excess was determined as (RA, Dec) = ($17^{\rm h}02^{\rm m}44^{\rm s}$, $-42°00'57''$). The intrinsic widths for the fit ellipse are $0°.30 \pm 0°.02$ for the major axis and $0°.15 \pm 0°.01$ for the minor axis, respectively. The spectrum is fit with a power-law with a photon index of $\Gamma = 2.1 \pm 0.1_{\rm stat} \pm 0.2_{\rm sys}$. The flux in the 1–10 TeV band is $(4.7 \pm 1.1) \times 10^{-12}$ ergs cm^{-2} s^{-1}. Although the nearby pulsar PSR J1702–4128 is energetic enough to account for the observed VHE γ-ray emission, no PWN has been detected from this pulsar. The nearby SNR G344.7–0.1 is too small and not positionally coincident with HESS J1702–420. Three X-ray binaries are also located nearby the source, but are outside the significant emission region (Aharonian et al., 2006a, 2008a).

HESS J1804–216 is the largest VHE γ-ray source. The excess map is shown in figure 4.37 (bottom). Assumed a two-dimensional Gaussian brightness profile, the best fit position for the center of the excess was determined as (RA, Dec) = ($18^{\rm h}04^{\rm m}33^{\rm s}$, $-21°42'06''$). The intrinsic width for the fit is $0°.200 \pm 0°.010$. The spectrum is fit with a power-law with a photon index of $\Gamma = 2.72 \pm 0.06_{\rm stat} \pm 0.2_{\rm sys}$. The flux in the 1–10 TeV band is $(10.3 \pm 3.1) \times 10^{-12}$ ergs cm^{-2} s^{-1}. Suzaku deep observations discovered two X-ray sources, Suzaku J1804–2142 and Suzaku J1804–2140, positionally coincident with HESS J1804–216. These two sources, however, are too faint in the X-ray band compared with the TeV γ-ray flux to explain by the traditional scenario that the VHE γ-rays are inverse Compton origin, thus associations

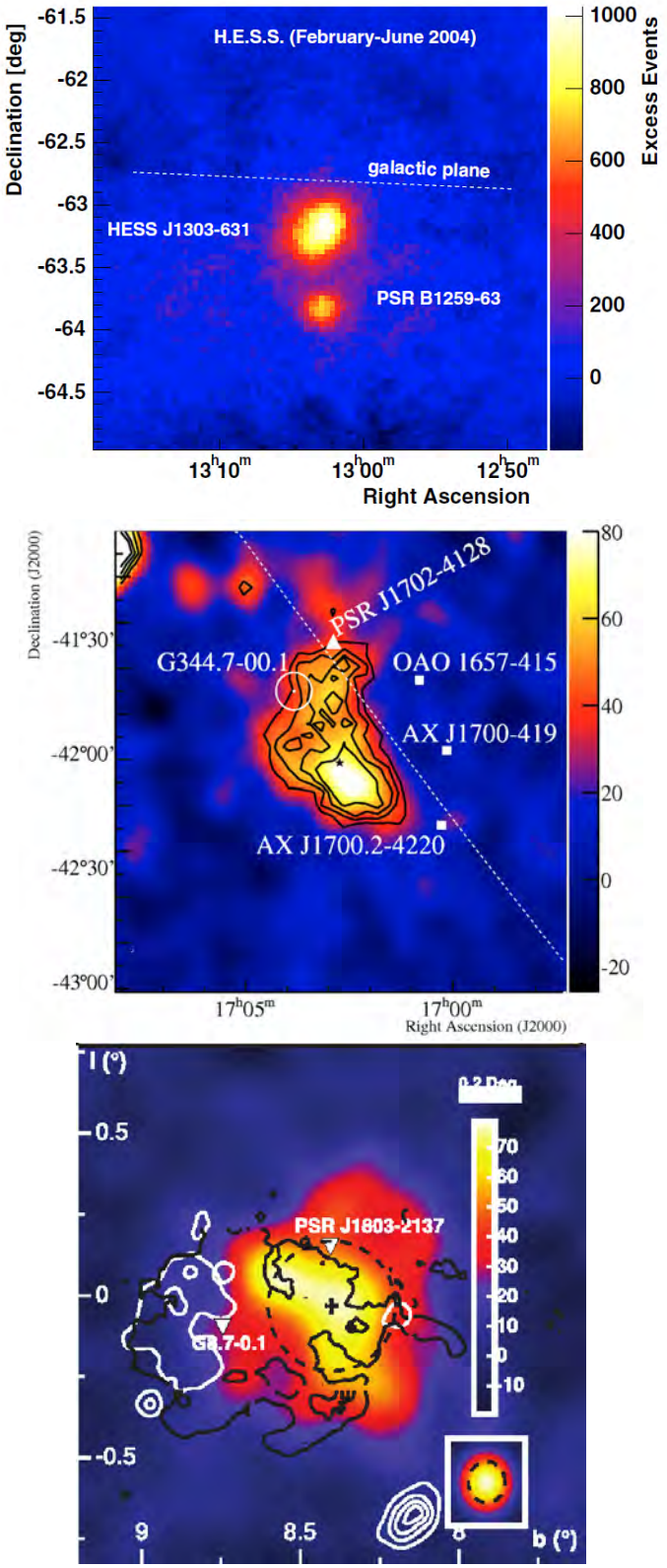

Figure 4.37: HESS excess maps around HESS J1303-631 (top; adapted from Aharonian et al. (2005d)), HESS 1702–420 (middle; adapted from Aharonian et al. (2008a)) and HESS J1804–216 (bottom; adapted from Aharonian et al. (2006a)). In the top panel, the binary system PSR B1259–63/SS2883 is seen at the south of HESS J1303-631.

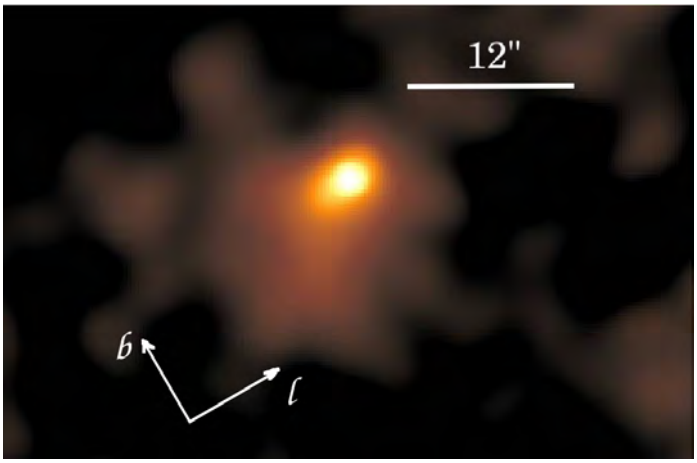

Figure 4.38: Smoothed 0.3–8 keV ACIS-S3 image of PSR J1803–2137 and its PWN. The brightness and smoothing scales are chosen to show the fainter, more extended emission from the PWN This figure is adapted from Kargaltsev et al. (2007).

of these sources remain unclear(Bamba et al., 2007). An energetic radio pulsar, PSR J1803–2137, is offset from the centroid of the VHE γ-ray emission by $\sim 10'$, but still within its extension. It is a 134 ms pulsar with a period derivative of $\dot{P} = 1.34 \times 10^{-13}$ s s^{-1}. The distance determined from the pulsar's dispersion measure is $d = 3.9$ kpc estimated based on the NE2001 Galactic electron-density model (Cordes & Lazio, 2002). The characteristic age and the spin-down luminosity are $\tau_c = 16$ kyr and $\dot{E} = 2.2 \times 10^{36}$ ergs s^{-1}, respectively. Chandra observation found an indication of a dim, asymmetric PWN component surrounding the pulsar extended toward HESS J1804–216 (see figure 4.38). The spectrum of the entire PWN is fit with an absorbed power-law with an absorption column of $N_{\rm H} = 1.38 \times 10^{22}$ cm^{-2} (best fit value) and a photon index of $\Gamma = 1.58 \pm 0.25$. The flux in the 2–10 keV band is $(5.0 \pm 0.5) \times 10^{-14}$ ergs cm^{-2} s^{-1}. However, the sensitivity of the Chandra observation was possibly insufficient to detect the PWN beyond 15″–20″ from the pulsar (Kargaltsev et al., 2007).

Chapter 5

Discussion

5.1 Summary of the VHE PWNe

Here we summarize the results obtained from our analysis of the X-ray data together with those from the literature for the convenience of discussion. The summaries are arranged in tables, which are divided into plural ones to fit in the pages.

In table 5.1, we list up the identified VHE γ-ray PWNe, which are selected according to Gallant et al. (2008) and are described in §4. Related references to the PWNe are also summarized in the table.

In table 5.2, we summarize the parameters of the pulsars associated to the PWNe listed in table 5.1. The entries are left blank when no associated pulsar is known as the case of G0.9+0.1 (#9). The parameters are put in parenthesis in the case of the Rabbit nebula, because the detection of pulsation is highly marginal and are not reliable as explained in §4.4. These two sources are not included in the following discussion when the pulsar parameters are concerned. Most of the pulse periods and the period derivatives in the table were taken from the ATNF pulsar catalog (Manchester et al., 2005). The magnetic field strength at the termination shock $B_{\rm TS}$ was calculated using the radius of the termination shock determined by Kargaltsev & Pavlov (2008a) from the balance of the ram pressure and the circumstellar pressure.

In table 5.3, we list the spectral parameters in both VHE γ-ray and X-ray bands. The γ-ray fluxes were taken from literature and were converted in the 1–10 TeV band. The unabsorbed X-ray fluxes, which were normalized to 2–10 keV band, were also taken from literature except for HESS J1837–069 and HESS J1809–197, which were observed and analyzed in this thesis with Suzaku. The X-ray fluxes were determined using relatively large extraction region to include both the emission from the pulsar and the nebulae.

In table 5.4, we list the morphological parameters of the emission regions in both VHE γ-ray and X-ray bands. The sizes of VHE γ-ray emission regions were derived from literature, in which they were determined by fitting the excess map with a two-

dimensional Gaussian function. When the sources are asymmetric, we list the sizes of both major and minor axes of the elongated Gaussian function. The sizes of X-ray emission regions were determined in this thesis by creating the profile of non-thermal X-ray emission around the pulsar and fitting them with a Gaussian function. When we fitted a Gaussian, we ignored the central $1'$ region from the pulsar to exclude the contamination from the bright pulsar to the diffuse emission. Offset is defined as the distance between the best-fit position of the two-dimensional Gaussian function in the VHE γ-ray band and the associated pulsar position.

Table 5.1: Identification of the VHE γ-ray PWNe and the references.

#	HESS name	PWN/Pulsar name	References
1	HESS J0534+220	Crab	1 2 3
2	HESS J0835–455	Vela X	4 5 6
3	HESS J1418–609	Rabbit	7 8
4	HESS J1420–607	K3/PSR J1420–6049	9 10 11
5	HESS J1514–591	MSH 15-52	12 13 14
6	HESS J1825–137	G18.0–0.7/PSR B1823–13	15 16 17
7	HESS J1833–105	G21.5-0.9	18 19 20 21
8	HESS J1846–029	Kes 75	22 23 24 25 26
9	HESS J1747–281	G0.9+0.1	27 28
10	HESS J1837–069	AX J1838.0–0655	29 30 31
11	HESS J1809–193	PSR J1809–1917	32 33 34 35
12	HESS J1718–385	PSR J1718–3825	36 37 38
13	HESS J1616–508	PSR J1617–5055	39 40 41
14	HESS J1804–216	PSR J1803–2137	42 43 44
15	HESS J1702–420	PSR J1702–4128	45 46 47
16	HESS J1303–631	PSR J1301–6305	48 49

References. — (1) Aharonian et al. (2006d), (2) Kirsch et al. (2005), (3) Trimble (1973) (4) Aharonian et al. (2006b), (5) Dodson et al. (2003), (6) Manzali et al. (2007) (7) Aharonian et al. (2006c), (8) Ng et al. (2005) (9) Aharonian et al. (2006c), (10) Ng et al. (2005), (11) Manchester et al. (2005) (12) Aharonian et al. (2005c), (13) Gaensler et al. (2002), (14) Manchester et al. (2005) (15) Aharonian et al. (2006e), (16) Uchiyama et al. (2008b), (17) Manchester et al. (2005) (18) H. E. S. S. Collaboration: A. Djannati-Atai et al. (2007), (19) Gallant et al. (2008), (20) Slane et al. (2000), (21) Manchester et al. (2005) (22) H. E. S. S. Collaboration: A. Djannati-Atai et al. (2007), (23) Gallant et al. (2008) (24) Helfand et al. (2003), (25) Gotthelf et al. (2000), (26) Manchester et al. (2005) (27) Aharonian et al. (2005b), (28) Porquet et al. (2003) (29) Aharonian et al. (2006a), (30) Anada et al. (2008), (31) Gotthelf & Halpern (2008) (32) Aharonian et al. (2007), (33) Renaud et al. (2008), (34) Manchester et al. (2005), (35) This work (36) Aharonian et al. (2007), (37) Hinton et al. (2007a), (38) Manchester et al. (2005) (39) Aharonian et al. (2006a), (40) Landi et al. (2007), (41) Manchester et al. (2005) (42) Aharonian et al. (2006a), (43) Kargaltsev et al. (2007), (44) Manchester et al. (2005) (45) Aharonian et al. (2006a), (46) Manchester et al. (2005), (47) Aharonian et al. (2008a) (48) Aharonian et al. (2005d), (49) Manchester et al. (2005)

Table 5.2: Parameters of pulsars associated with the PWNe identification by HESS.

#	d^{*}	P	$\dot{P}$	$\tau_c^{\dagger}$	$\log \dot{E}^{**}$	$\log(\dot{E}/d^2)$	$\log B_{\rm S}^{\ddagger}$	$\log B_{\rm LC}^{\S}$	$B_{\rm TS}^{\|}$
	kpc	ms	s s^{-1}	kyr	ergs s^{-1}	ergs s^{-1} kpc^{-2}	Gauss	Gauss	μG
1	2.0 ± 0.1	34	4.16×10^{-13}	1.3	38.6	38.0	12.6	6.0	350
2	0.29 ± 0.02	89	1.25×10^{-13}	11	36.8	37.9	12.5	4.6	390
3$^{\#}$	(5.0)	(108)	(1.06×10^{-12})	(1.6)	(37.5)	(36.1)	(13.0)	(4.9)	—
4	$5.6 \pm 1.1^{\S\S}$	68	8.32×10^{-14}	13	37.0	35.5	12.4	4.8	76
5	$4.2 \pm 0.8^{\S\S}$	151	1.54×10^{-12}	1.6	37.3	36.0	13.2	4.6	25
6	$3.9 \pm 0.8^{\S\S}$	102	7.51×10^{-14}	21	36.4	35.3	12.4	4.4	99
7	$4.3 \pm 0.9^{\S\S}$	62	2.02×10^{-13}	4.9	37.5	36.3	12.6	5.1	270
8	$5.2 \pm 1.0^{\S\S}$	326	7.08×10^{-12}	0.7	36.9	35.5	13.7	4.1	74
9	$(8.5)^{\#\#}$	—	—	—	—	—	—	—	—
10	$6.6 \pm 0.9^{\|\|\|}$	70	4.92×10^{-14}	23	36.7	35.1	12.3	4.7	—
11	$3.5 \pm 0.7^{\S\S}$	83	2.55×10^{-14}	51	36.3	35.1	12.2	4.4	63
12	$3.6 \pm 0.7^{\S\S}$	75	1.32×10^{-14}	90	36.1	35.0	12.0	4.3	—
13	$4.8 \pm 0.9^{\S\S}$	69	1.35×10^{-13}	8.1	37.2	35.8	12.5	4.9	190
14	$3.9 \pm 0.8^{\S\S}$	134	1.34×10^{-13}	16	36.3	35.2	12.6	4.2	180
15	$6.8 \pm 1.4^{\S\S}$	182	5.23×10^{-14}	55	35.5	33.9	12.5	3.7	—
16	$6.7 \pm 1.3^{\S\S}$	184	2.67×10^{-13}	11	36.2	34.6	12.9	4.0	—

* Distance to the pulsar.
† Characteristic age.
** Logarithm of the spin-down luminosity.
‡ Logarithm of the surface magnetic field.
§ Logarithm of the magnetic field at the light cylinder.
$^{\|}$ Magnetic field at the termination shock, which was calculated using the distance of the termination shock listed in Kargaltsev & Pavlov (2008a).
$^{\#}$ Detection of the X-ray pulsation was highly marginal and the parameters were not reliable (Ng et al., 2005).
§§ Estimated from the dispersion measure for the pulsar and the Galactic electron-density model according to Cordes & Lazio (2002). Errors are conservatively estimated at 20%.
$^{\|\|\|}$ Determined from the radial velocity of the nearby cluster of red supergiants by Davies et al. (2008).
$^{\#\#}$ The source is assumed to be located at the Galactic center.

Table 5.3: Spectral parameters of the PWNe in the VHE γ-ray and X-ray bands.

#	$\Gamma_{\rm TeV}$	$F^{*}_{\rm TeV}$ 10^{-12} ergs cm^{-2} s^{-1}	$\log L^{\dagger}_{\rm TeV}$ ergs s^{-1}	$N_{\rm H}$ 10^{22} cm^{-2}	$\Gamma_{\rm X}$	$F^{**}_{\rm X}$ 10^{-12} ergs cm^{-2} s^{-1}	$\log L^{\ddagger}_{\rm X}$ ergs s^{-1}
1	$2.39 \pm 0.12^{\#}$	76 ± 15	34.5	0.4 ± 0.003	2.12 ± 0.005	19000 ± 43	36.9
2	$1.4 \pm 0.29^{\#}$	55 ± 18	32.7	0.0259 ± 0.0001	1.61 ± 0.02	52.8 ± 0.4	32.7
3	2.22 ± 0.18	7.7 ± 1.6	(34.3)	1.4 ± 0.2	1.50 ± 0.14	7.3 ± 0.2	(34.3)
4	2.17 ± 0.16	11 ± 2	34.6	$5.4^{+1.7}_{-2.2}$	$2.3^{+0.8}_{-0.9}$	1.3 ± 0.14	33.7
5	2.27 ± 0.23	16 ± 4	34.5	0.95 ± 0.03	2.05 ± 0.04	37 ± 2	34.9
6	2.38 ± 0.17	49 ± 10	34.9	$0.93^{+0.09}_{-0.06}$	$1.98^{+0.06}_{-0.05}$	$5 \pm 1^{\|}$	33.9
7	2.08 ± 0.32	1.5 ± 0.5	33.5	2.24 ± 0.04	1.91 ± 0.04	$46 \pm 9^{\|}$	35.0
8	2.26 ± 0.25	1.7 ± 0.5	33.7	3.96 ± 0.08	1.92 ± 0.04	$28 \pm 5^{\|}$	34.9
9	2.40 ± 0.23	2.0 ± 0.5	(34.2)	$14.7^{+1.3}_{-1.4}$	$1.99^{+0.18}_{-0.19}$	$5.8 \pm 1.2^{\|}$	(34.7)
10	2.27 ± 0.21	14 ± 4	34.8	5.4 ± 0.5	1.27 ± 0.11	10.7 ± 0.3	34.7
11	2.23 ± 0.2	18 ± 9	34.4	0.7 ± 0.1	1.5 ± 0.1	$5 \pm 1^{\|}$	33.9
12	$0.7 \pm 0.63^{\S}$	2.9 ± 1.3	33.6	$0.72^{+0.08}_{-0.3}$	$1.86^{+0.13}_{-0.22}$	$0.13 \pm 0.03^{\|}$	32.3
13	2.35 ± 0.21	16.8 ± 5.1	34.6	$3.87^{+0.28}_{-0.36}$	$1.42^{+0.10}_{-0.12}$	$4.2 \pm 0.8^{\|}$	34.0
14	2.72 ± 0.21	10.3 ± 3.1	34.3	1.38	1.58 ± 0.25	0.05 ± 0.005	31.9
15	2.1 ± 0.2	4.7 ± 1.1	34.4	—	—	—	—
16	2.44 ± 0.21	9.9 ± 2.6	34.7	—	—	—	—

* Flux in the 1–10 TeV band.
† Logarithm of the Luminosity in the 1–10 TeV band.
** Flux in the 2–10 keV band.
‡ Logarithm of the Luminosity in the 2–10 keV band.
$^{\#}$ Exponential cutoff at ~ 14 TeV.
§ Exponential cutoff at ~ 6 TeV.
$^{\|}$ Errors are conservatively estimated at 20%.

Table 5.4: Morphological parameters of the PWNe in the VHE γ-ray and X-ray bands.

#	$\sigma^{*}_{\rm TeV}$ arcmin	$\sigma'_{\rm TeV}{}^{\dagger}$ arcmin	$R^{**}_{\rm TeV}$ pc	$R'_{\rm TeV}{}^{\dagger}$ pc	$\sigma^{\S}_{\rm X}$ arcmin	$R^{\|}_{\rm X}$ pc	Offset$^{\#}$ arcmin	Offset$^{\#}$ pc
1	—	—	—	—	—	—	—	—
2	28.8	21.6	7.3	5.4	23.5	5.9	25	2.1
3	4.9	2.7	—	—	1.8	—	9.0	—
4	3.3	3.3	16.1	16.1	1.4	6.8	2.9	4.7
5	6.4	2.3	23.6	8.5	1.5	5.8	3.1	3.8
6	15.6	13.8	53.5	47.3	3.5	12.0	18	20.0
7	—	—	—	—	0.73	2.7	—	—
8	—	—	—	—	0.63	2.9	—	—
9	—	—	—	—	—	—	—	—
10	7.2	3	41.4	17.3	1.3	7.2	6.4	12.4
11	15	15	46.4	46.4	6.8	21.1	6.5	6.7
12	9	4	28.3	12.6	4.2	13.2	7.9	8.2
13	8.2	8.2	33.8	33.8	1.8	7.5	11	14.8
14	12	12	40.6	40.6	—	—	11	12.4
15	18	9	107	54	—	—	35	70.0
16	9.6	9.6	55.7	55.7	—	—	20	38.1

* RMS size of the VHE γ-ray emission region (major-axis).
† RMS size of the VHE γ-ray emission region (minor-axis).
** 3σ radius of the VHE γ-ray emission region (major- axis).
‡ 3σ radius of the VHE γ-ray emission region (minor- axis).
§ RMS size of the X-ray emission region.
$^{\|}$ 3σ radius of the X-ray emission region.
$^{\#}$ Distance from of the pulsar to the best-fit position of the VHE γ-ray emission region.

5.2 Properties of the PWNe Detected by HESS

In this section, we examine the properties of the PWNe detected by HESS in comparison with the PWNe in general. One may suspect that the VHE γ-ray emitting PWNe could be exceptional ones having some extreme parameters. However, as we explain below, they share common properties with other PWNe dim in the VHE γ-ray band.

5.2.1 Association of a Pulsar with the VHE Gamma-Ray Sources

Although pulsars are found in the vicinity of the VHE γ-ray sources, this does not necessarily mean that they are physically associated. Because pulsars are preferentially located along the Galactic plane, where the VHE γ-ray sources are also found, they could be located close in the sky by chance. Therefore, we need to evaluate chance probability of finding two sources nearby to verify their physical association. Instead of the chance probability itself, we evaluate the expected number of pulsars to be found in the vicinity of the unidentified VHE PWNe. If the expected number is small enough, the nearby pulsar is considered to be physically associated to the VHE γ-ray source. A total of $\sim$1600 pulsars is listed in the ATNF catalog (Manchester et al., 2005). We screened the catalog in two steps to calculate the surface density of the pulsars. First is the location of the pulsars. Because the pulsars tend to locate along the Galactic plane, we selected only those located in the Galactic plane survey region by HESS ($-85^\circ < l < 60^\circ, -2.5^\circ < b < 2.5^\circ$). Second is the spin-down flux ($\dot{E}/d^2$: spin-down luminosity normalized by the distance) of the pulsar. Because the VHE γ-ray associated pulsars tend to have large spin-down luminosities, we need to select only those with high spin-down flux to evaluate the surface density of pulsars. The lowest spin-down flux in our sample is $\dot{E}/d^2 = 7.3 \times 10^{33}$ ergs s^{-1} kpc^{-2} of PSR J1702–4128. After the screening of these two steps, it remained 51 pulsars in the catalog. This means an average surface density of the pulsars is 0.070 deg^{-2}. The largest angular distance between the suspected pulsar and the VHE γ-ray source is also found for PSR J1702–4128 (HESS J1702–4128) and is $35'$. Hence, we calculate the expected number of pulsars for the circular region of a radius of $35'$ centered at the VHE γ-ray source; the result was 0.075. Although this number is not very small, it becomes much smaller for other pulsars with smaller angular separation and larger spin-down flux. Furthermore, if we consider the association of pulsars for the 16 VHE γ-ray sources simultaneously, it is highly unlikely that all the association happen by chance. Therefore, we conclude that the pulsar found in the vicinity of VHE γ-ray sources are in fact physically associated.

The chance probability to find a pulsar near the VHE γ-ray source was previously

studied by Carrigan et al. (2007) in a different context. They searched for the VHE γ-ray emission in the HESS data at the position of the known pulsars. The HESS data sets they used covered the Galactic plane of $-60^\circ < l < 30^\circ, -2^\circ < b < 2^\circ$. A total of 435 pulsars was located in the region, and significant γ-ray emission was detected from 30 pulsars. However, this does not necessarily mean that all the association is genuine. Therefore, they examined the probability of the chance coincidences between VHE γ-ray sources and radio pulsars taking into account the spin-down luminosities of the pulsars. The rate of chance coincidence is estimated by generating 10^6 realizations of random pulsar samples following the distribution in longitude and latitude of the pulsars in the ATNF pulsar catalog taking into account the narrowing of the distribution in latitude with increasing spin-down flux. The results are shown in figure 5.1 (left) as a function of the spin-down flux ($\dot{E}/d^2$) in ergs s^{-1} kpc^{-2}. The figure shows the distribution of radio pulsars (histogram in light gray), that of chance coincidences (histogram in dark gray), and of pulsars detected with a significant γ-ray excess in black line. Chance coincidence is negligible for pulsars with high spin-down luminosities. Figure 5.1 (right) shows the fraction of pulsars with significant γ-ray emission. The expected fraction of chance coincidences is shown as dark shaded areas in figure 5.1 (right). According to their estimation, the probability that the detection of VHE sources coincident with 9 or more of the total of 23 pulsars above $\dot{E}/d^2 > 10^{34}$ ergs s^{-1} kpc^{-2} by chance is $\sim 3.4 \times 10^{-4}$. It is difficult to compare this estimation directly to ours because of the different assumptions. However, the conclusion is same in a sense that the chance probability to find of the high-luminosity pulsars near the VHE γ-ray sources is very low. This result supports our conclusion that the associations in our sample are basically genuine.

5.2.2 Spin-Down Luminosities of the Associated Pulsars

Figure 5.2 (left) compares the distribution of the spin-down luminosities of pulsars in PWNe detected and not detected by HESS. The spin-down luminosities of PWNe which was not detected by HESS were adapted from Kargaltsev & Pavlov (2008a). Mean spin-down luminosity $\dot{E}$ (in ergs s^{-1}) of the PWNe detected by HESS is $\log \dot{E} = 36.8$ with a standard deviation of 0.7, while that not detected is $\log \dot{E} = 36.4$ with a standard deviation of 0.5. Thus the mean spin-down luminosities are same within the statistical error for these two groups of the PWNe.

It is expected that the distribution of the spin-down fluxes (luminosities normalized at 1 kpc) of the HESS detected pulsars has a sharp cut-off at the detection limit of HESS. Figure 5.2 (right) compares the distributions of the spin-down fluxes of the PWNe detected and not detected by HESS. Logarithm of the mean spin-down flux (ergs s^{-1} kpc^{-2}) of the PWNe detected by HESS is 36.2 with the standard deviation of 0.9. On the other hand, that not detected by HESS is 35.8 with the standard

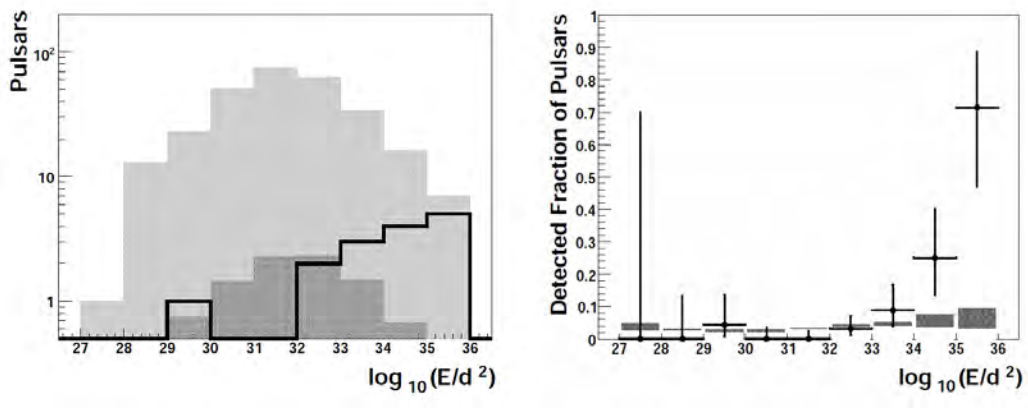

Figure 5.1: Distribution of radio pulsars in $\log_{10}(\dot{E}/d^2)$ (taken from Carrigan et al. (2007)). Here, $\dot{E}/d^2$ is measured in ergs s^{-1} kpc^{-2}. Left: Distribution of the radio pulsars in the HESS scan range (shaded in light gray), of chance coincidences (shaded in dark gray) and of detected a significant γ-ray excess (black line). Right: the fraction of radio pulsars which appear to have associated TeV γ-ray PWN.

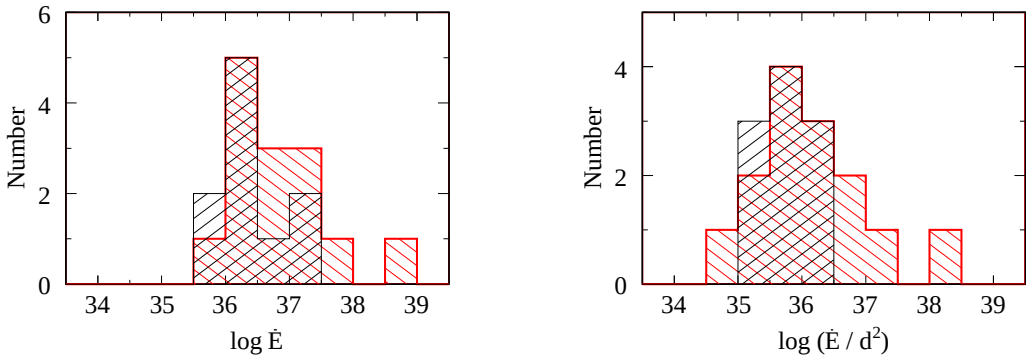

Figure 5.2: Left: Distribution of the spin-down luminosities of the PWNe is compared between those detected by HESS (black hatch) and not detected (red hatch). Right: Distribution of the spin-down fluxes ($\dot{E}/d^2$) in ergs s^{-1} kpc^{-2} are compared between the PWNe detected by HESS (red hatch) and those not detected (black hatch).

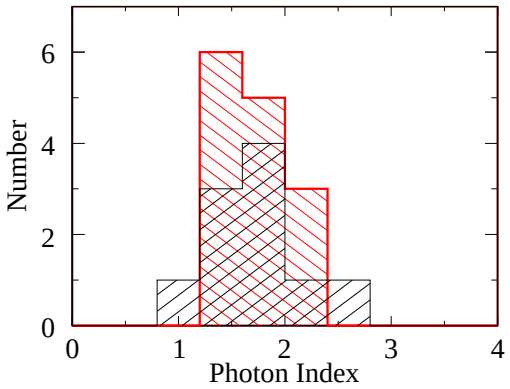

Figure 5.3: Distribution of the photon indices of PWNe in the X-ray band. Histograms with red and black hatch indicate those of the PWNe detected and not detected by HESS, respectively.

deviation of 0.4. Contrary to the expectation, there is no significant difference on the spin-down fluxes between the pulsars detected and not detected by HESS. Implication of this result is discussed in §5.2.4.

5.2.3 X-ray Photon Indices

Figure 5.3 compares the distributions of the X-ray photon indices of PWNe detected and not detected by HESS. Photon indices of PWNe which were not detected by HESS were adapted from Kargaltsev & Pavlov (2008a). Mean photon index of the PWNe detected by HESS is 1.79 with the standard deviation of 0.30, while that not detected by HESS is 1.76 with the standard deviation of 0.39. These values are same within the statistical error. This result supports our conclusion that the nature of the PWNe detected by HESS are not different from that of ordinal PWNe.

5.2.4 Luminosities in the VHE Gamma-Ray and X-Ray Bands

Here we study correlations between the luminosities (in the VHE γ-ray and X-ray bands) of the PWNe detected by HESS and the characteristic ages of the associated pulsars using the compilation in the tables in §5.1. The TeV γ-ray luminosities of the PWNe are shown in figure 5.4, and those in X-ray band are in the top panels of figure 5.5. As shown in the left panel of figure 5.4, γ-ray luminosities L_γ in the 1–10 TeV band show little correlation with the characteristic ages (τ_c kyr), while X-ray luminosities L_X in the 2–10 keV band are negatively correlated with them as shown in the top left panel in figure 5.5. In these plots, the Rabbit nebula is ignored from the reason described in §5.1.

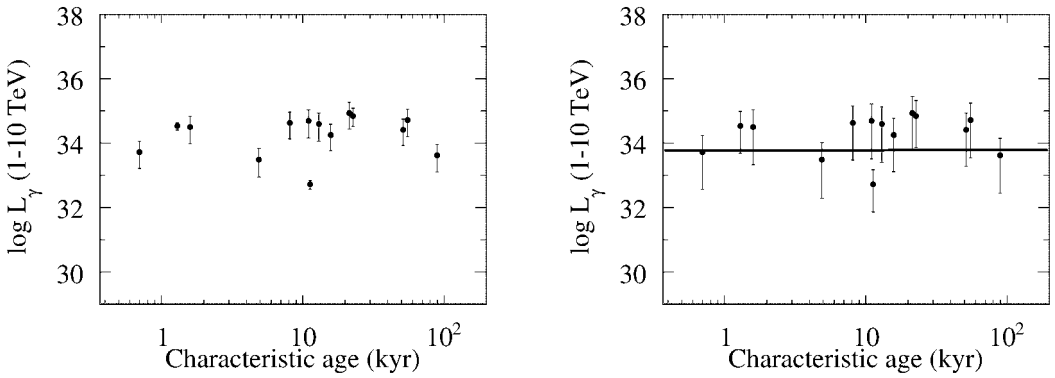

Figure 5.4: VHE γ-ray luminosities of the PWNe as a function of the characteristic age of the associated pulsars. Systematic errors are added to the luminosities when we fit the data (right panel). Solid line in the right panel shows the best-fit power-law function on the whole data set.

In order to quantify the correlation, we fitted a power-law function (i.e. line function in a log-log plot) to the data. In the fit, we added systematic error until χ^2_ν became $\sim$1 from two reasons. One is to deal with the heterogeneous set of data; some have good statistics, while some do not. Unless systematic error is added, fit result would be strongly biased by a small number of data points with very good statistics. This is not appropriate to evaluate the general trend of data. The other is to estimate the errors of the best-fit parameters correctly. Statistical errors of the parameters are usually determined from the condition that $\Delta\chi^2 \sim 1$. This method does not work when χ^2_ν is significantly larger than unity. Thus we need to add systematic error until χ^2_ν reaches unity. It is noteworthy that the systematic error we add is not related to the instrumentation or observations, rather to the lack of our knowledge on the PWNe. X-ray and VHE γ-ray luminosities are not determined solely by the characteristic age of the pulsar. They might depend on the evolutional history and ambient environment of the PWNe, surface magnetic field of the pulsar, and so on. However, it is practically impossible to construct a detailed model considering all these dependences. Such a detailed model is also not required for the current purpose. Therefore we adopt a simple power-law model and add systematic error to cope with our lack of knowledge.

The best-fit power-law function we obtained for the γ-ray luminosity and the characteristic age is (figure 5.4 right panel):

$$\log_{10} L_\gamma = (33.8 \pm 0.4) - (0.0 \pm 0.3) \log_{10} \tau_c. \tag{5.1}$$

Similarly, the best-fit function for the X-ray luminosity and the characteristic age is

(figure 5.5 top right panel):

$$\log_{10} L_X = (34.7 \pm 0.5) - (1.5 \pm 0.5) \log_{10} \tau_c. \quad (5.2)$$

Someone may think that the Crab Nebula cannot be dealt with on the same plot because it may seem to be an unusual case. Even if we treat it as an exception, the X-ray luminosity is still correlated with the characteristic age. the best-fit function ignoring the Crab Nebula is

$$\log_{10} L_X = (34.4 \pm 0.8) - (1.3 \pm 0.7) \log_{10} \tau_c, \quad (5.3)$$

where the spope still declines with the significanse of $\sim 2\sigma$.

It is noteworthy that the detection limit of HESS does not introduce a bias in the correlation between the VHE γ-ray luminosity and the characteristic age of the pulsar. Even if the detection limit of HESS were much lower, it would increase the number of dim sources in luminosity both for the younger and older pulsars, because there is no correlation between the characteristic age of the pulsar and its distance from the Earth. Therefore, absence of correlation between the VHE γ-ray luminosity and the characteristic age is not due to the detection limit of HESS.

We also fitted the relation between the X-ray luminosities of the PWNe not detected by HESS and the characteristic ages of the associated pulsars. The luminosities were adapted from Kargaltsev & Pavlov (2008a), and were converted to those in 2–10 keV band. Figure 5.5 shows the correlation (bottom left panel) and the best-fit function (bottom right panel). The best-fit function is:

$$\log_{10} L_X = (33.6 \pm 0.6) - (0.9 \pm 0.5) \log_{10} \tau_c. \quad (5.4)$$

Although marginal, the relation is consistent with that of the PWNe from which the VHE γ-ray emissions were detected, as described in equation (5.2). This result support those of the previous sebsections that the properties of the VHE γ-ray emitting PWNe are not different from those not emitting VHE γ-rays.

Equation 5.1 shows that the VHE γ-ray luminosity is independent of the characteristic age of the pulsar. On the other hand, the X-ray luminosity is inversely correlated with the characteristic age as described by equation 5.2. As suggested by Mattana et al. (2008), the difference of correlations can be explained by the difference of the cooling time of the electrons which emit TeV γ-rays and X-rays. We showed in §2.7.2 that electrons emitting X-rays have higher energies than those emitting TeV γ-rays. Because the life time of electrons are inversely proportional to their energies, this means that the TeV γ-ray emitting electrons have much longer life time than that of X-ray emitting electrons. According to the quantitative evaluation in §2.7.2, the characteristic age of pulsars falls in between these two life times in most cases. Based on the above consideration, difference of the correlation of the VHE γ-ray and X-ray luminosities with the characteristic age of the pulsars is interpreted as follows.

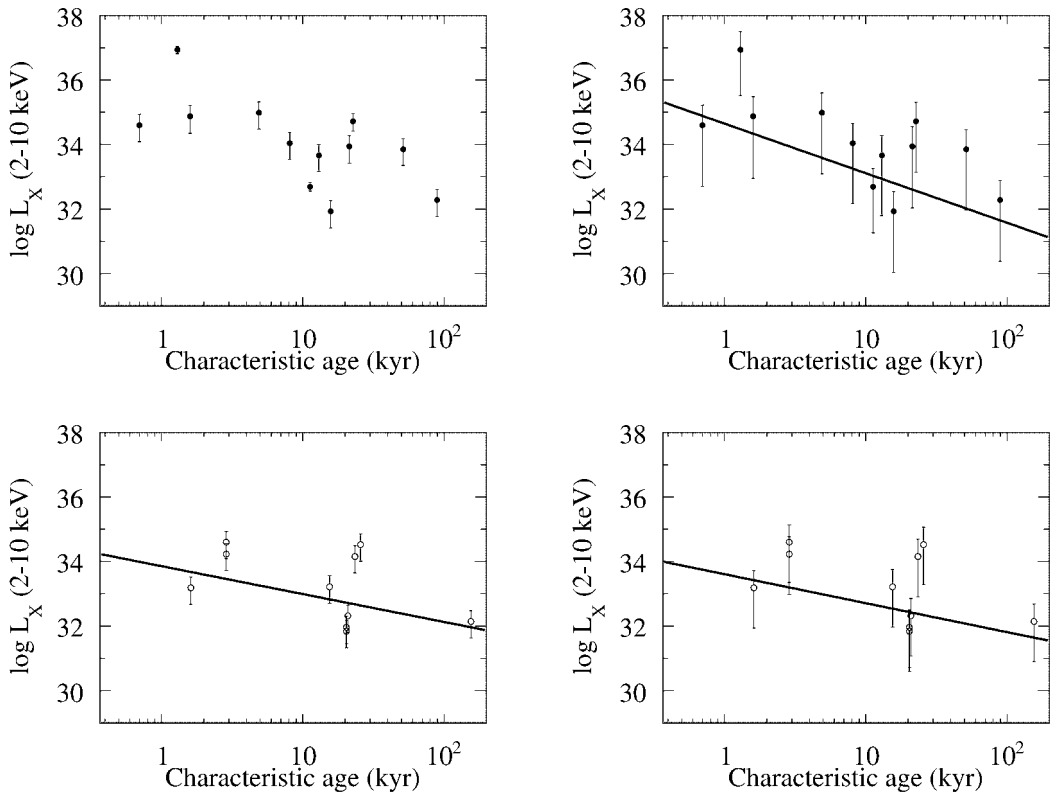

Figure 5.5: X-ray luminosities of the PWNe as a function of the characteristic age of the associated pulsars. Top panels show the correlations of X-ray luminosities of the HESS detected PWNe with the characteristic ages, while the bottom panels those not detected by HESS. Systematic errors are added to the luminosities when we fit the data (right panels). Solid lines in the right panels show the best-fit power-law functions on the whole data set.

- Most of the electrons emitting TeV γ-rays were accelerated a long time ago, mostly at the birth of the pulsar, and have been radiating till now with a negligible loss of the energy.

- Electrons emitting X-rays are accelerated only recently and lose their energies quickly.

Above interpretation may be rephrased that the TeV γ-ray emission reflects an integrated history of the pulsar's activity since its birth, whereas the X-ray emission reflects the instantaneous activity of the pulsar. This also explains why there is no significant difference on the spin-down fluxes between the PWNe detected and not detected by HESS. Because the TeV γ-ray emission reflects the integrated pulsar's activity since its birth, it may be natural to have no direct correlation with the current spin-down luminosity. Therefore, the current spin-down flux is not a good indicator to describe the TeV γ-ray flux.

Taking the results in this section into consideration, we discuss the morphological properties of PWNe in the following sections.

5.3 Morphology of the VHE Gamma-Ray and X-Ray Emission regions

In this section, we study the morphological properties of the VHE γ-ray and X-ray emission regions. We first discuss the spatial offset between the VHE γ-ray emission region and the associated pulsar, which is seen in many of the VHE γ-ray emitting PWNe. We then study the spatial extent of the γ-ray and X-ray emission regions and their dependence on the pulsar age. We discuss possible origin of the extension of the emission regions as a function of the pulsar age.

5.3.1 Spatial Offsets of the Pulsars

In many of the VHE γ-ray PWNe, the associated pulsar is seen offset from the center of the γ-ray emission region. The offset is as large as $35'$ as listed in table 5.4. Because the offset is seen in many of the γ-ray PWNe, it is considered to be a common property of them. We discuss here whether the offset can be explained by the proper motion (i.e. kick velocity) of the pulsar.

We discussed in the previous section that the VHE γ-ray emitting electrons have been accumulated since the birth of the pulsar. A larger number of electrons tend to be accelerated at a birth of the pulsar when the pulsar was most active. This means that the major fraction of the VHE γ-ray emitting electrons were produced just after the birth of the pulsar. Thus, the center of the VHE γ-ray emission region

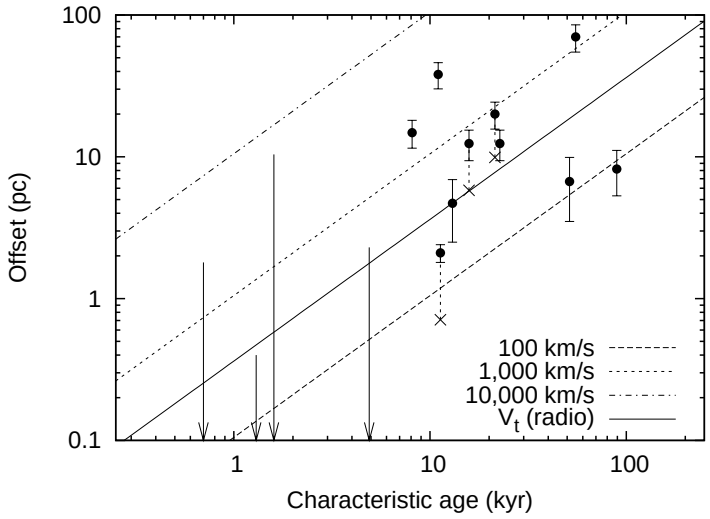

Figure 5.6: Relation between the characteristic age and the offset of the pulsar from the center of the VHE γ-ray emission region. Dashed, dotted and dot-dash lines indicate transverse velocities of 100 km/s, 1000 km/s and 10000 km/s, respectively. Solid line shows the mean transverse velocity V_t (= 345 km/s) observed in the radio band (Lyne & Lorimer, 1994). Cross marks show the transverse velocities listed in table 5.5.

is considered as a birth place of a pulsar. On the other hand, the current position of the pulsar could be significantly offset from its birth place due to the kick velocity of the pulsar.

A kick velocity is a reaction to the pulsar from the asymmetric explosion of the supernova. Although it is difficult to measure the kick velocity itself, we can measure its transverse component as a proper motion of the pulsar. Because the radio interferometry has very high angular resolution, the proper motion was measured for many pulsars and was cataloged as a transverse component of the kick velocity. We show in figure 5.7 the transverse velocities of the pulsars in the ATNF catalog as a function of the characteristic age. The transverse velocities are on average a few hundreds km/sec and are mostly < 1000 km/sec. However, some have a very large velocity reaching $\sim$4000 km/sec.

According to this interpretation, the offset between the center of the VHE γ-ray emission region and the pulsar represents the distance traveled by the pulsar with the kick velocity since its birth. Figure 5.6 shows a relation between the offset and the characteristic age of the pulsar; transverse velocities are also indicated in the figure. Most of the data points are scattered around the mean transverse velocity of the pulsars V_t (= 345 km/sec) observed in the radio band (Lyne & Lorimer, 1994). The largest velocity we obtained, $\sim$ 3000 km/sec for HESS J1303–631 with PSR

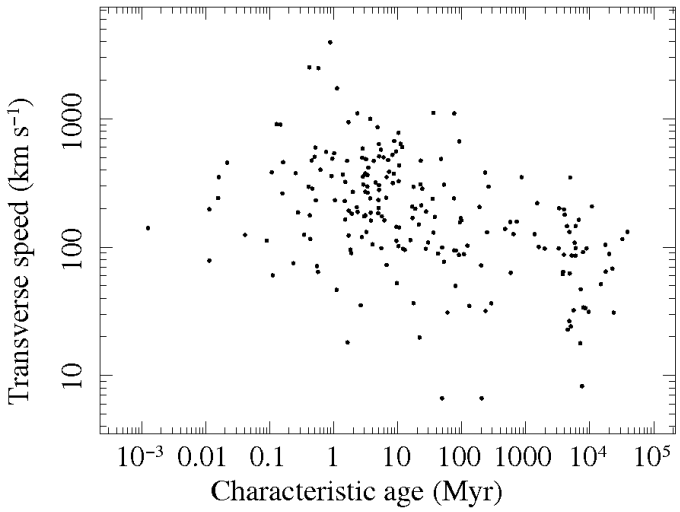

Figure 5.7: Transverse velocities of the pulsars in the ATNF catalog as a function of their characteristic ages.

1301–6305, is still conceivable as a kick velocity.

Some of our sample PWNe have measured transverse velocities by the radio observations; they are Crab, Vela, PSR B1823–13, and PSR J1803–2137. The transverse velocities and their position angles are listed in table 5.5 with those estimated from the offset. The velocities estimated here are systematically overestimated from those determined by the radio observations by a factor of two or three. In addition, the position angles of the transverse velocities are different from those determined from the offset. These differences may be due to the displacement of the center of the VHE γ-ray emission from the birth place of the pulsar. The hydrodynamic simulations for Vela X performed by Blondin et al. (2001) showed that SNR expansion into an inhomogeneous medium would result in a reverse shock returning first from the region of higher density. Because the termination shock is created when the bulk wind pressure equals the ambient pressure, it may develop first in the direction of higher density. Furthermore, for the middle-aged pulsars such as Vela pulsar, the spherically assymmetric reverse shock wave can push the PWN off-center from the explosion site. Thus the center of gravity of the VHE γ-ray emission region is considered to be offset from the pulsar's birth place. This can be also applicable to the PSR B1823–13 and PSR J1803–2137. This scenario can explain the differences shown in table 5.5. In figure 5.6, we superimposed the transverse velocities measured by the radio observations with cross marks. Although our scenario overestimates the transverse velocities by a factor of two or three, we can still conclude that the pulsars associated with the PWNe detected by HESS have ordinal transverse velocities.

Table 5.5: Transverse velocities and their position angles.

	Crab	Vela	PSR B1823–13	PSR J1803–2137
Estimated by the positional offset (A)				
V_t^* (km/sec)	—	180	930	780
position angle θ^{**} (degree)	—	11	27	296
Measured by the radio observations (B)				
$V_t^\dagger$ (km/sec)	140	60[1]	440[2]	350[3]
position angle $\theta^\ddagger$ (degree)	—	301[1]	100[2]	38[3]
Differences				
Ratio of V_t (A/B)	—	3.0	2.1	2.2
$\Delta\theta$ (degree)	—	70	73	102

References: [1] Dodson et al. (2003) [2] Pavlov et al. (2008) [3] Brisken et al. (2006)
* Transverse velocity estimated by the offset between the center of the VHE emission and the pulsar.
** Angular offset of the pulsar to the center of the VHE emission (east of north).
† Transverse velocity determined by the radio observations.
‡ Position angle of the transverse velocity (east of north).

5.3.2 Extension of the Emission Regions

We discuss here the extensions of the VHE γ-ray and X-ray emission regions. Figure 5.8 compares the angular sizes of the X-ray and the VHE γ-ray emission regions. The angular sizes of VHE γ-ray emission regions were determined by fitting the excess map with a 2-D Gaussian function, while those of X-ray emission region were determined by fitting the profile of the intensity map with a Gaussian function ignoring the bright part near the pulsar with a radius of $1'$. In the plot, the extensions are represented by 1σ of the fit results. In the case of the VHE γ-ray PWNe with an elongated shape, angular sizes were determined for the major and minor axes and are plotted with upward and downward triangles in the figure. It is clear from the figure that the angular sizes of the VHE γ-ray emission region are always larger than those of the X-ray emission regions. This result is consistent with the discussion in the previous section that the TeV emitting electrons has much longer life time than that of the X-ray emitting electrons. The life time of the X-ray emitting electrons is even shorter than the characteristics age of the pulsars. Therefore, the X-ray emitting electrons cannot extend very much before they loose significant energy, whereas the TeV emitting electrons can extend all through their life since the generation at the birth of the pulsars.

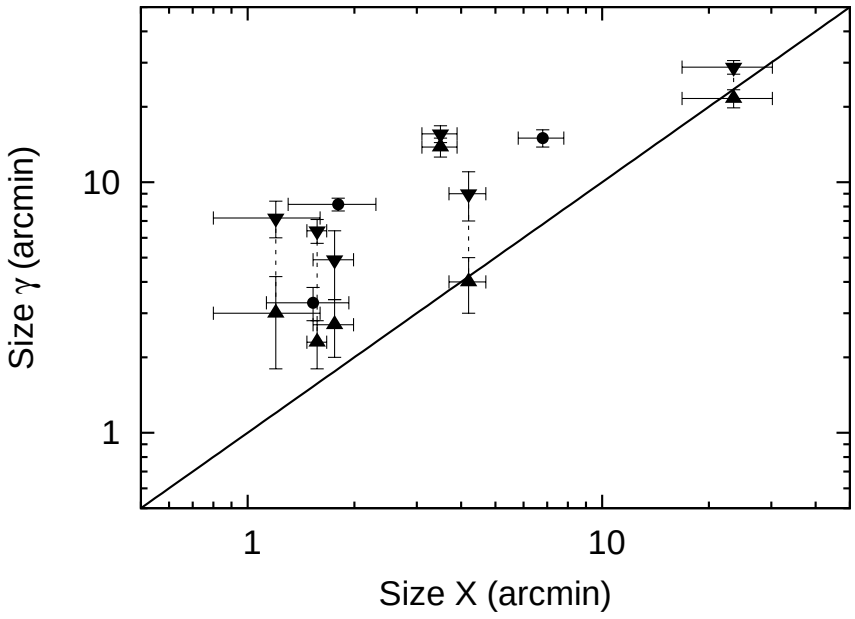

Figure 5.8: Comparison of the angular sizes of the X-ray and the VHE γ-ray emission regions. Circle shows the PWNe with symmetric shape in VHE γ-ray band. Downward and upward triangles show the angular sizes of major and minor axes of the VHE γ-ray emission regions, respectively.

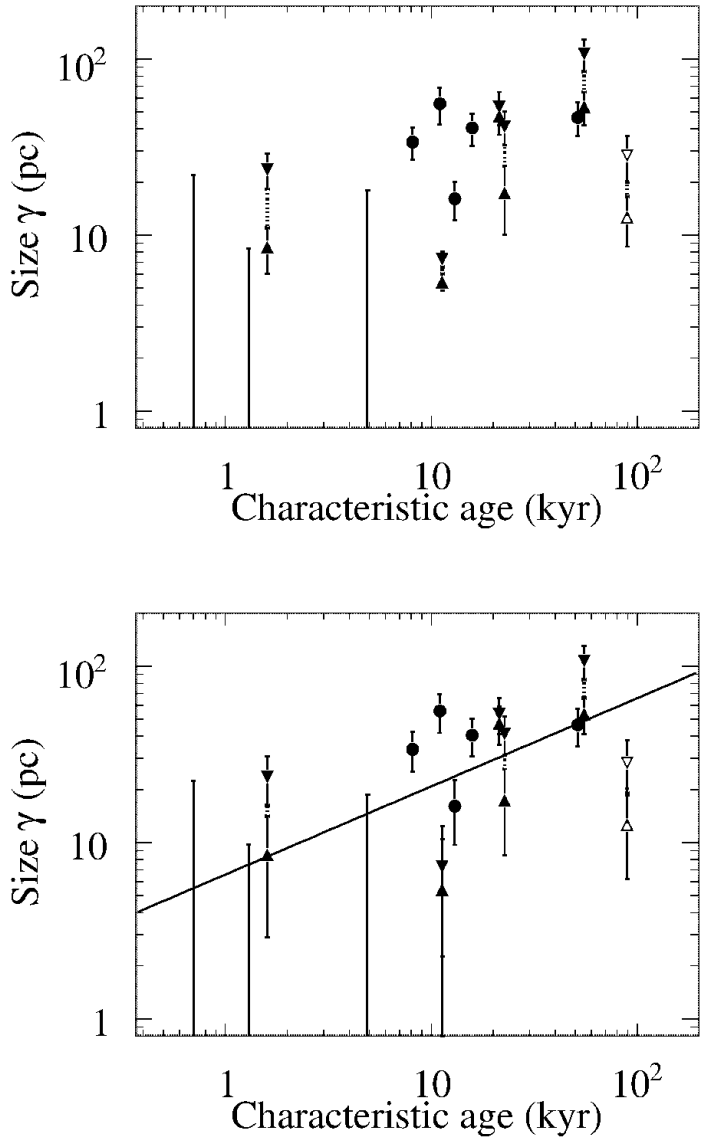

Figure 5.9: Top: Sizes of the TeV emission regions, which are defined as the 3σ of the fitted 2-D Gaussian function to the excess map of the source, as a function of the characteristic ages of the pulsars. The size of the major and minor axes are represented by downward and upward triangles with fit errors, respectively. Bottom: Systematic error of 5 pc is added to each size of the TeV emission region. Solid line indicates the best-fit diffusion model.

Size of the VHE Gamma-Ray Emission Region

Now we discuss the correlation between the size of the VHE γ-ray emission region and the characteristic age of the pulsar. Figure 5.9 shows the correlation; the extension is defined as 3σ of the best-fit Gaussian and the distance is assumed to be same as the associated pulsar. According to the discussion in the previous section, the extension of the γ-ray emission region should result from the diffusion of the electrons accelerated at the birth of the pulsar. In order to verify this interpretation, we estimate approximately the diffusion distance of high energy electrons.

Hereafter, we represent the energy of an electron by E_e, the energy of the Compton up-scattered photon by $\epsilon_{\rm IC}$, and the photon energy of the synchrotron radiation by $\epsilon_{\rm syn}$, respectively. Basically the high energy electrons obey the gyromotion, and the diffusion may be caused by the perturbation or scattering to the gyro-motion. If we assume the scattering occurs along the direction of the magnetic field, the diffusion coefficient can be written from equation (2.9) as

$$K = \frac{1}{3}\xi c\frac{E_e}{eB} \sim 3.3\times10^{24}\xi\left(\frac{B}{10\ \mu\mathrm{G}}\right)^{-1}\left(\frac{E_e}{1\ \mathrm{TeV}}\right)\ \mathrm{cm}^2\ \mathrm{s}^{-1}, \tag{5.5}$$

where ξ is a gyrofactor, $\xi \sim (B/\delta B)^2$. Considering equation (2.42),

$$K_\gamma = 7\times10^{25}\xi\left(\frac{B}{10\ \mu\mathrm{G}}\right)^{-1}\left(\frac{\epsilon_{\rm IC}}{1\ \mathrm{TeV}}\right)^{\frac{1}{2}}\ \mathrm{cm}^2\ \mathrm{s}^{-1}, \tag{5.6}$$

From equation (2.8), the diffusion distance Δ of the relativistic electrons is represented as

$$\Delta = \sqrt{K_\gamma t}, \tag{5.7}$$

where t is an elapsed time from the start of the diffusion, which corresponds to the characteristic age of the pulsar. We fitted the size of VHE γ-ray emission region shown in figure 5.9 with the equation (5.7). We ignored 3 of the 16 sources in the fit: Rabbit, G09+0.1, and HESS J1718−385. The reasons are as follows. The pulsation was so marginal for Rabbit that it is difficult to determine the characteristic age reliably. No pulsation was detected from G09+0.1. In the case of HESS J1718−385, associated pulsar is so old that energy loss of the accelerated electrons is not negligible. If we assume a magnetic field of $B \sim 3\ \mu$G, the synchrotron lifetime of electrons which produce 1 TeV γ-rays via inverse Compton scattering of CMBR is $\tau_{\rm loss} \sim 30$ kyr from equation (2.43). In fact, the VHE γ-ray spectrum has a break at $\sim$7 TeV as shown in §4.11.1. This is the evidence of significant energy loss of the Comptonizing electrons. Because the electron cooling reduces the size of the γ-ray emission region, we ignored this source in the fit.

When we fit the data, we added systematic errors of 5 pc to the size of the VHE γ-ray emission regions. This is because the size of the emission region, which was

determined by fitting the 2-D Gaussian, indicates not the accurate source extent but only the representative value. The model of 2-D Gaussian was selected from the simplicity, and the true morphology may be different from the Gaussian. Furthermore, characteristics of individual sources, such as local structures caused by the inhomogeneity of the circumstellar matter or the magnetic field, were ignored in the analysis. All these should be reflected to the systematic errors. However, it is difficult to determine the systematic error accurately, because it depends on the detailed morphology of the source [50]. Therefore, the magnitude of the systematic error, 5 pc, was selected so that the source size varied smoothly as a function of interested parameters, e.g. characteristic age of the pulsar. The fit result is shown in figure 5.9 bottom panel. The best-fit diffusion coefficient was found to be $K_\gamma = (1.2 \pm 0.3) \times 10^{28}$ cm^{-2} s^{-1} with $\chi^2_\nu = 2.0$ (12 degree of freedom). Substituting this into equation (5.6) yields,

$$\xi \sim (50 \pm 10) \left(\frac{B}{3\ \mu\mathrm{G}} \right) \left(\frac{\epsilon_{\mathrm{IC}}}{1\ \mathrm{TeV}} \right)^{-\frac{1}{2}}. \tag{5.8}$$

Büsching et al. (2007) estimated the diffusion coefficient of cosmic ray protons for the Galactic center region of $K \sim (1-5)$ kpc^2 Myr^{-1} $= (3-15) \times 10^{29}$ cm^2 s^{-1} for a mean proton energy of ~ 3 TeV. In an ultrarelativistic situation, the gyro radius for a proton is equal to that for an electron. Thus we can use equation (5.6) and obtain $\xi \sim 10^4 (B/10\ \mu\mathrm{G})(\epsilon_{\mathrm{IC}}/1\ \mathrm{TeV})^{-1/2}$. This value is larger than our estimation. However, ξ estimated from the cosmic ray diffusion may reflect the global environment of the interstellar space. On the other hand, electron diffusion around the PWNe may be strongly affected by the local environment perturbed by the presence of PWNe. In fact, a strong turbulence is suggested at the downstream of the shell of the SN 1006 (Bamba, 2003b) or at the torus of the Crab nebula (Shibata et al., 2003), even up to the Bohm limit ($\xi \sim 1$). Therefore, the diffusion coefficient derived from the size of the VHE γ-ray emission is considered to be reasonable and appropriate for the PWNe.

Size of the X-Ray Emission Region

Here we discuss the correlation of the size of the X-ray emission region and the characteristic age of the associated pulsar as shown in figure 5.10. The size of the X-ray emission region was determined by fitting the profile of the X-ray intensity map of the non-thermal emission with a Gaussian function, ignoring the photons from the bright pulsar. The size is defined here as the 3σ width of the Gaussian function.

As shown in figure 5.10, the size of the X-ray emission region continue to increase with the increase of the characteristic age of the pulsar, even up to $\sim$ 100 kyr.

[50] Stefan Funk, private communication.

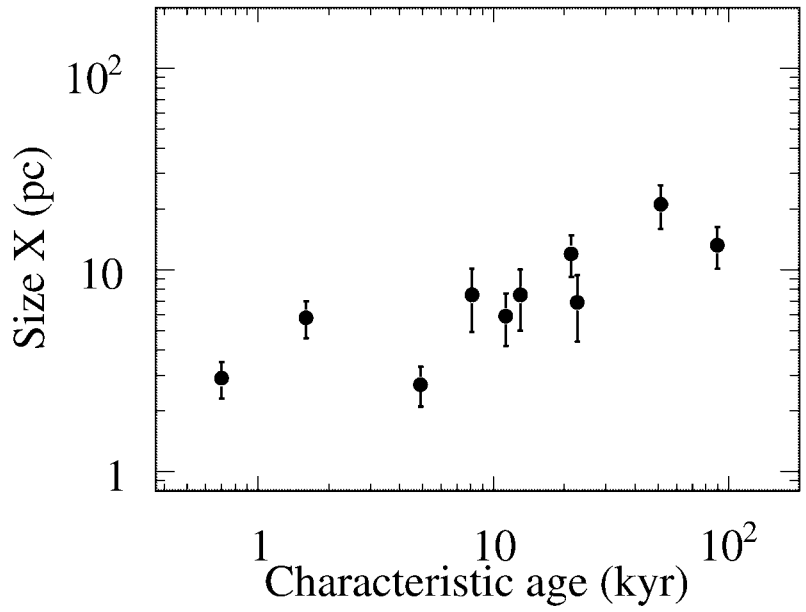

Figure 5.10: Correlation between the size of the X-ray emission region and the characteristic age of the associated pulsar.

However, this is in contradiction with naive interpretation, because the synchrotron lifetime of electrons is

$$\tau_{\rm syn} = 3.1 \times 10^5 \times \left(\frac{E_e}{1\ {\rm TeV}}\right)^{-1} \left(\frac{U_0}{1\ {\rm eV\ cm^{-3}}}\right)^{-1}\ {\rm yr}$$

$$= 1.8 \times \left(\frac{B}{10\ \mu{\rm G}}\right)^{-\frac{3}{2}} \left(\frac{\epsilon_{\rm syn}}{1\ {\rm keV}}\right)^{-\frac{1}{2}}\ {\rm kyr}, \tag{5.9}$$

which is much shorter than ~ 100 kyr. This means that a simple diffusion cannot explain the correlation between the size of the X-ray emission region and the characteristic age of the pulsar.

To explain the result, we need to assume that the diffusion coefficient is variable either spatially or temporally. However, spatial variation of the diffusion coefficient does not explain the continuous expansion of the emission region up to ~ 100 kyr, because the electron diffusion reach a steady state anyway after the expected life time described in the above equation. This means that we need to incorporate the time variation of the diffusion coefficient; electrons become much easier to diffuse when the PWNe gets old. It is noteworthy that similar effect can be realized even if the advection speed $V_{\rm adv}$ of electrons increases with time. Therefore, we consider two

scenarios here to explain the correlation between the size of X-ray emission region and the characteristic age of the pulsar:

1. Diffusion dominant scenario
2. Advection dominant scenario

Note that these two scenarios are not exclusive but can happen simultaneously.

1. Diffusion dominant scenario In this scenario, ξ is assumed to increase with the age of the pulsar. Because ξ is determined by the turbulence of the magnetic field, this means that turbulence of the magnetic field decreases with the age of the pulsar. We assume that $\xi(t)$ is unity when the pulsar was born and increases according to the following equation:

$$\xi(t) = 1 + \alpha \left(\frac{t}{1 \text{ kyr}} \right)^{\beta}. \tag{5.10}$$

Then, the diffusion coefficient becomes

$$K_X = 2.3 \times 10^{26} \, \xi(t) \left(\frac{B}{10 \, \mu\text{G}} \right)^{-\frac{3}{2}} \left(\frac{\epsilon_{\text{syn}}}{1 \text{ keV}} \right)^{\frac{1}{2}} \text{ cm}^2 \text{ s}^{-1} \tag{5.11}$$

$$= 0.8 \, \xi(t) \left(\frac{B}{10 \, \mu\text{G}} \right)^{-\frac{3}{2}} \left(\frac{\epsilon_{\text{syn}}}{1 \text{ keV}} \right)^{\frac{1}{2}} \text{ pc}^2 \text{ kyr}^{-1}. \tag{5.12}$$

Now we consider the size of the X-ray emission region after t kyr. The size $\Delta(t)$ defined by the diffused electrons emitting 1 keV X-rays in the magnetic field of $B = 10$ μG for the diffusion duration of $T(t)$ is

$$\Delta(t) = \sqrt{K_X \cdot T(t)} = 0.9 \, \xi(t)^{\frac{1}{2}} \left(\frac{T(t)}{1 \text{ kyr}} \right)^{\frac{1}{2}} \text{ pc}, \tag{5.13}$$

Here, the duration of diffusion is limited by the lifetime of electrons, thus

$$T(t) = \begin{cases} t & (t < \tau_{\text{loss}}) \\ \tau_{\text{loss}} & (t > \tau_{\text{loss}}), \end{cases} \tag{5.14}$$

where $\tau_{\text{loss}} = 1.8$ kyr is the synchrotron lifetime of electrons in the magnetic field of 10 μG. Therefore,

$$\Delta(t) = \begin{cases} 0.9 \left(1 + \alpha \left(\frac{t}{1 \text{ kyr}} \right)^{\beta} \right)^{\frac{1}{2}} \left(\frac{t}{1 \text{ kyr}} \right)^{\frac{1}{2}} \text{ pc} & (t < \tau_{\text{loss}}) \\ 0.9 \left(1 + \alpha \left(\frac{t}{1 \text{ kyr}} \right)^{\beta} \right)^{\frac{1}{2}} \left(\frac{\tau_{\text{loss}}}{1 \text{ kyr}} \right)^{\frac{1}{2}} \text{ pc} & (t > \tau_{\text{loss}}), \end{cases} \tag{5.15}$$

We fitted the data in figure 5.10 with equation (5.15) for $t > \tau_{\rm loss}$. The fit yielded

$$\xi(t) = 1 + (1.2 \pm 0.7) \left(\frac{t}{1 \text{ kyr}} \right)^{(1.1 \pm 0.2)}. \tag{5.16}$$

Figure 5.11 shows the best-fit model. The model line in $t < \tau_{\rm loss}$ is not the best-fit one, but the model in equation (5.15) with substitution of the best-fit parameters. According to the best-fit parameters, ξ would be $\sim$200 when $\tau_c = 100$ kyr.

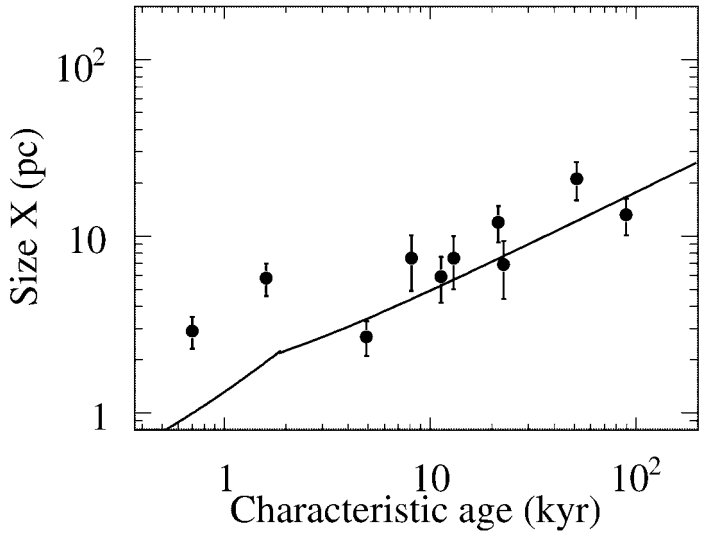

Figure 5.11: The fitting result with the diffusion model. The diffusion coefficient is assumed to be a function of time.

2. Advection dominant scenario Asymptotic solution of the advection speed $V_{\rm adv}$ when $r \to \infty$ was derived by Kennel & Coroniti (1984) as a function of σ. Here, σ is defined in the upstream of the shock as the ratio of the electromagnetic to particle energy flux:

$$\sigma = \frac{B_1^2}{4\pi n_1 u_1 \gamma_1 m c^2}, \tag{5.17}$$

where n_1 is the proper density, u_1 the radial four speed of the wind, $\gamma^2 = 1 + u_1^2$, m the electron rest mass, B_1 the shock frame magnetic field. When the shock is strong, $V_{\rm adv}$ can be expressed as

$$V_{\rm adv} \to \frac{\sigma}{1+\sigma} c \quad (r \to \infty). \tag{5.18}$$

We consider the case that the advection speed $V_{\rm adv}$ increase with the age of the pulsar. We assume that $\sigma(t)$ increases according to the following equation:

$$\sigma(t) = \alpha \left(\frac{t}{1 \text{ kyr}} \right)^{\beta}. \tag{5.19}$$

The size $\Delta(t)$ of the X-ray emission region after t kyr with the propagating duration of $T(t)$ is

$$\Delta(t) = V_{\rm adv}(t) \cdot T(t) = \frac{\sigma(t)}{1+\sigma(t)} cT(t) \sim \sigma(t) cT(t), \tag{5.20}$$

where $T(t)$ is defined in equation (5.15). Therefore,

$$\Delta(t) = \begin{cases} 315\ \alpha \left(\frac{t}{1 \text{ kyr}} \right)^{\beta} \left(\frac{t}{1 \text{ kyr}} \right) \text{ pc} & (t < \tau_{\rm loss}) \\ 315\ \alpha \left(\frac{t}{1 \text{ kyr}} \right)^{\beta} \left(\frac{\tau_{\rm loss}}{1 \text{ kyr}} \right) \text{ pc} & (t > \tau_{\rm loss}), \end{cases} \tag{5.21}$$

We fitted the data in figure 5.10 with equation (5.21) for $t > \tau_{\rm loss}$. The fit yielded

$$\sigma(t) = (2.4 \pm 0.6) \times 10^{-3} \left(\frac{t}{1 \text{ kyr}} \right)^{(0.55 \pm 0.08)}. \tag{5.22}$$

The best-fit model is shown in figure 5.12. The model in $t < \tau_{\rm loss}$ is not the fit result, but is simply equation (5.21) with substitution of the best-fit parameters. The result indicates σ would be as large as ~ 0.03 when $\tau_c = 100$ kyr. Equation (5.22) is consistent with the result of Kennel & Coroniti (1984) that $\sigma \sim 0.003$ for the Crab Nebula, whose age is 1.3 kyr.

Implications of the change of the diffusion coefficient and advection speed
We showed that the size of the X-ray emission region continues to extend up to $\sim$100 kyr. This cannot be explained unless we introduce the time variations of the diffusion coefficient and/or advection speed as the PWNe become old. These two scenario are illustrated in figure 5.13.

Increase of the diffusion coefficient means that the magnetic field becomes less turbulent with the pulsar's age. This can be interpreted that the termination shock of the pulsar wind becomes rather weak with the age of the pulsar. In this interpretation, we have assumed that electrons diffuse along the magnetic field. However, toroidal magnetic field may be dominant in the PWNe. In such a case, electrons need to diffuse perpendicular to the magnetic field. The diffusion coefficient is then given from equation (2.12) with $\theta = 90^{\circ}$. When $\xi \gg 1$, equation (2.12) becomes

$$K \sim \frac{r_g c}{3\xi} = \frac{1}{3} \eta r_g c, \tag{5.23}$$

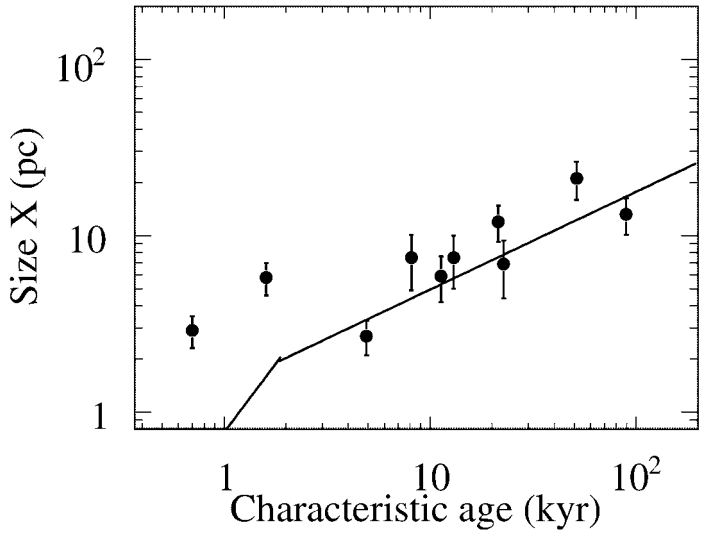

Figure 5.12: Fitting result with the advection dominant model. The ratio of the electromagnetic energy flux to the particle energy flux, σ, is assumed to be a function of time.

where $\eta = \xi^{-1} = (\delta B/B)^2$. This means that the electrons can diffuse more easily if the turbulence of the magnetic field is stronger. In this case, our result means $\eta \sim 200$ at ~ 100 kyr, which is interpreted that the toroidal magnetic field is not dominant any more. This result may be appropriate to the diffusion of the electrons in the supernova ejecta, rather than in the PWN.

In the case of the second scenario, increase of the advection speed suggests that the ratio of the electromagnetic energy flux to the particle energy flux becomes large as the pulsar becomes old. However, because it is poorly understood yet how the electromagnetic energy flux is converted to the particle energy flux in the shock, it is difficult to assess the feasibility of this scenario. It may be noteworthy that we need to consider the continuity condition between the shocked wind and the supernova ejecta to get more realistic solution in the advection dominant scenario.

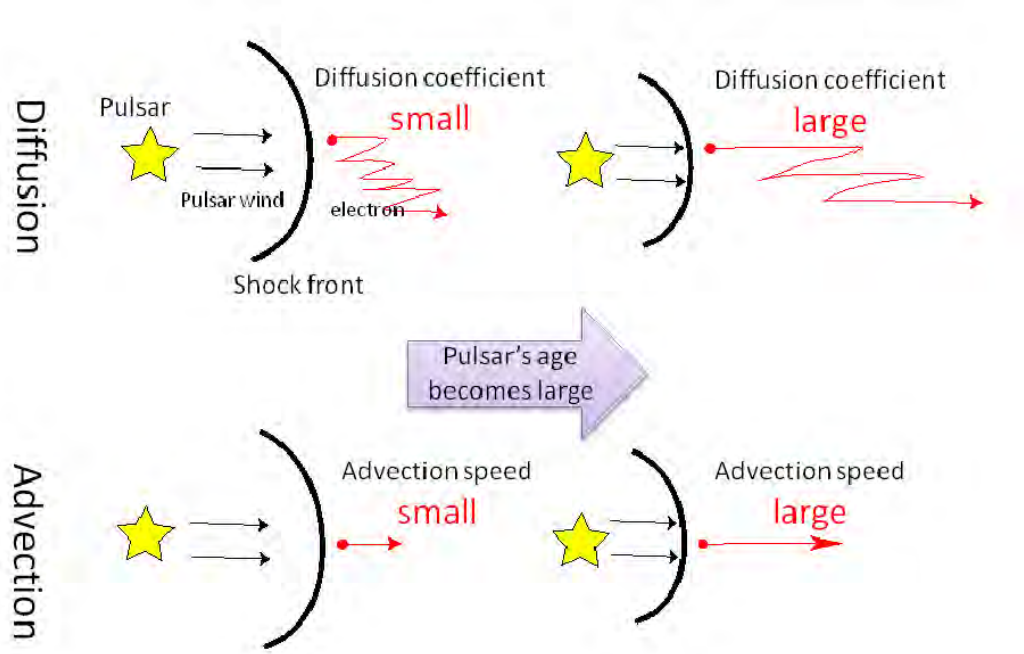

Figure 5.13: The scenario of the evolution of the PWN. Top and bottom figures show that the diffusion coefficient and the advection speed increase with the age of a pulsar, respectively. It is thought of as either or both of which are occurring in PWNe.

Chapter 6

Conclusion

We performed a systematic X-ray study of the PWNe discovered in the VHE γ-ray band. We studied all of the 16 PWNe which are candidate counterparts of the unidentified VHE γ-ray sources discovered by the H.E.S.S. Cherenkov telescopes on the Galactic plane. We analyzed X-ray data of individual sources to define their properties; two of them (HESS J1837–069 and HESS J1809–193) were studied in detail, for which we acquired new Suzaku data. Following results were obtained for the two sources:

HESS J1837–069 We showed for the first time that the suspected counterpart AX J1838.0–0655 was actually the source of 70.5 ms pulsation. We also showed that the X-ray emission (both the flux and spectral shape) and the spin-down of the source were very stable for the time interval of $\sim$7 yr. These results clearly identify the source as the PWN.

HESS J1809–193 Suzaku observation of this source was motivated by the spatial variation of the spectral slope in the VHE γ-ray band. Although non-thermal diffuse X-ray emission was noticed, no systematic variation in the X-ray spectral slope was detected in the diffuse emission. This result is consistent with the interpretation that we see different population of high energy electrons in VHE γ-ray band and X-ray band.

Through the systematic study of the 16 PWNe including above two sources, we obtained following results:

- The physical parameters characterizing the PWNe, i.e. spin-down luminosity, kick velocity of the pulsar, and the spectral slope in the X-ray band showed no systematic difference between those detected and not detected by HESS in the VHE γ-ray band. Furthermore, correlation between the age of the pulsar and the X-ray luminosity was also same for these two groups. This means that the PWNe detected by HESS are just the ordinary PWNe.

- The size of the non-thermal X-ray emission region increases with the age of the PWNe up to ~ 100 kyr. Because the synchrotron energy loss timescale of electrons is significantly shorter than the age of the PWNe, this means that the electrons can be extended much easier when the PWNe become old. Two mechanisms are conceivable to explain this finding: time evolution of the magnetic turbulence in the termination shock (diffusion dominant scenario) and that of the advection speed after the shock (advection dominant scenario). We showed that the ξ, which characterizes the degree of the magnetic turbulence, must increase from ~ 1 to ~ 200 by ~ 100 kyr in the diffusion dominated scenario. In the case of advection dominant scenario, the ratio of the electromagnetic to particle energy flux, σ, must increase from ~ 0.003 for the Crab Nebula (characteristic age ~ 1.3 kyr) to ~ 0.03 by ~ 100 kyr. Either or both of these processes are considered to work in the termination shocks of PWNe. Although both scenarios have some difficulties, this is the first observational evidence which shows a time evolution of the termination shock in the PWNe.

Appendix A

Multiband Spectrum for HESS J1837-069 and HESS J1809-193

In this appendix, we show the multiband spectrum for HESS J1837–069 and HESS J1809-193. Figure A.1 shows the spectral energy distribution (SED) in the X-ray and TeV γ-ray bands for HESS J1837–069. The thick blue line shows the power-law model obtained by fitting the X-ray spectrum of the Suzaku data extracted from the $3'$ circular region around AX J1838.0–0655 as described in §4.1.3. The thick red line represents the HESS spectrum, which was extracted from the $14'$ circular region centered at the HESS source.

We calculated a simple one-zone synchrotron+IC model using the calculation code developed by Kataoka (2000), in which a single population of relativistic electrons in TeV energy range emit both X-rays through synchrotron radiation and TeV γ-rays through Compton upscattering of CMB photons. The contribution of the synchrotron self-Compton radiation is negligible because the typical magnetic field in the PWN is relatively weak (~ 10 μG). The electron number index is fixed to $p = 2$. Free parameters of this model are the ambient magnetic field, the normalization of the incident electron and the maximum electron energy. First, the normalization of the electron injection is optimized so that the synchrotron spectrum model reproduce the flux of the XIS data. The maximum electron energy is assumed to be 400 TeV because of its very hard spectrum. Here the emission region is assumed to be 6 pc in radius. The models are shown in figure A.1 (top) with different ambient magnetic fields. As shown in this figure, the model can not reproduce the TeV flux for HESS J1837–069 unless we assume the magnetic field with the strength of ~ 1 μG, which is lower than that of the ISM magnetic field (~ 3 μG). Furthermore, spectral slope of the TeV data cannot be reproduced even if we adjust the magnetic field. Second, we optimized the normalization of the electron injection so that the IC spectrum model reproduce the flux of the TeV data. The maximum electron energy is assumed to be 20 TeV in order to adjust the spectral slope of the TeV data. The emission region

is assumed to be 27 pc in radius. The models are shown in figure A.1 (bottom) with different ambient magnetic fields. As shown in this figure, the model cannot reproduce the spectral slope of the X-ray data at all.

Figure A.2 shows the SED for HESS J1809–193. The thick blue line shows the power-law model obtained by fitting the X-ray spectrum of the Suzaku data extracted from the $7'$ circular region around PSR J1809–1917 as described in §4.2.3. The thick red line represents the HESS spectrum, which was extracted from the $\sim 36'$ circular region centered at the HESS source.

We calculated a simple one-zone synchrotron+IC model as described above. The electron number index is fixed to $p = 2$. First, the normalization of the electron injection is optimized so that the synchrotron spectrum model reproduce the flux of the XIS data. The maximum electron energy is assumed to be 400 TeV in order to adjust the spectral slope of the X-ray data. Here the emission region is assumed to be 7 pc in radius. The models are shown in figure A.2 (top) with different ambient magnetic fields. As shown in this figure, the model can not reproduce the TeV flux even if we assume the magnetic field with the strength of ~ 1 μG. Furthermore, spectral slope of the TeV data cannot be reproduced even if we adjust the magnetic field. Second, we optimized the normalization of the electron injection so that the IC spectrum model reproduce the flux of the TeV data. The maximum electron energy is assumed to be 20 TeV in order to adjust the spectral slope of the TeV data. The emission region is assumed to be 36 pc in radius. The models are shown in figure A.2 (bottom) with different ambient magnetic fields. As shown in this figure, the model cannot reproduce the spectral slope of the X-ray data at all.

These results are consistent with our scenario that

- The characteristic electron energy is different between the two components. (see §2.7.2)
- The spacial distribution of each component, i.e. the average magnetic field, is different. (see §5.3)

In our scenario, the simple one-zone synchrotron+IC model cannot be applied.

It is noteworthy that the X-ray spectrum of AX J1838.0–0655 shows very hard photon index ($\sim$1.3$\pm$0.1). Some PWNe also show such a hard spectrum (Kargaltsev & Pavlov, 2008a). This cannot be explained by the simple assumption that electrons accelerated through the first-order Fermi acceleration emit synchrotron radiation, because the X-ray spectrum should become a power-law with a photon index of ~ 1.5 under this assumption. In addition, X-ray spectra of other PWNe show various photon indices shown in §5.2.3. These may include important information on the acceleration mechanism, but is beyond the scope of this thesis.

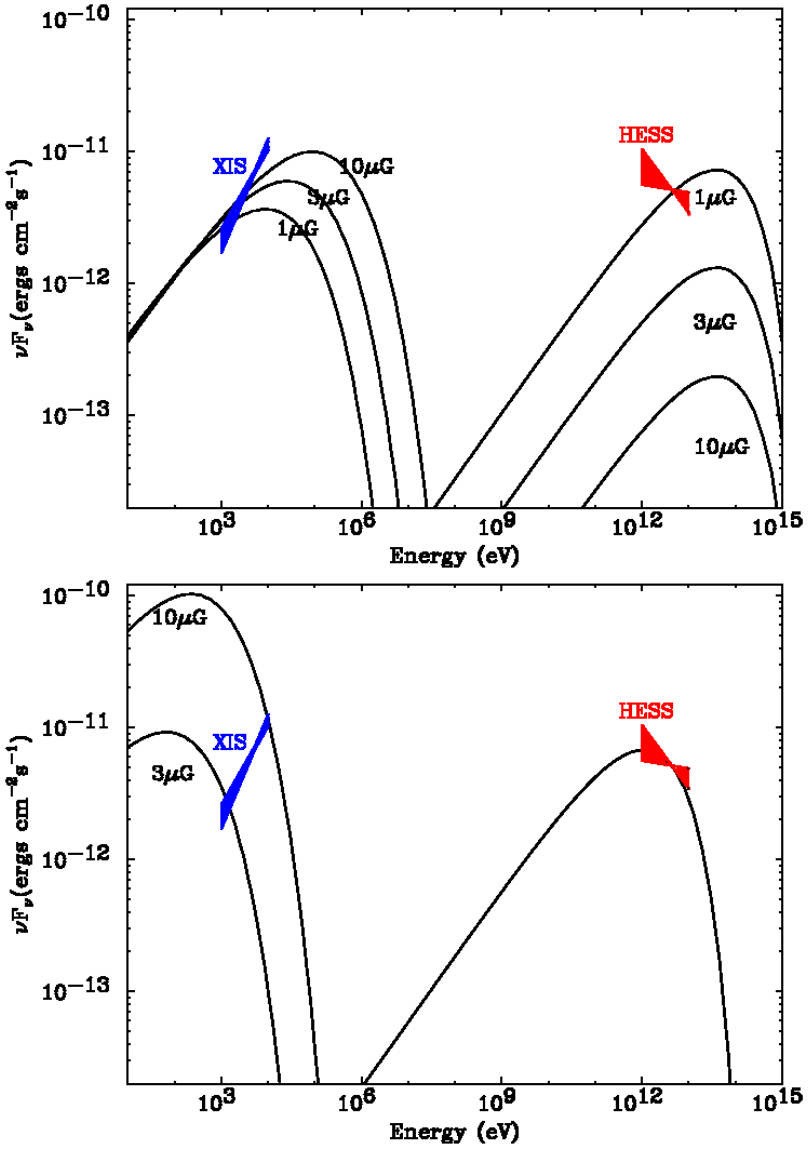

Figure A.1: Spectral energy distribution for the Suzaku and HESS (Aharonian et al., 2006a) measurements with synchrotron and inverse Compton models for HESS J1837–069. Electron number index is assumed to be $p = 2$. The normalization and the maximum energy of electrons are adjusted to reproduce approximately the X-ray data (top) and the TeV data (bottom). Black lines show the different ambient magnetic fields.

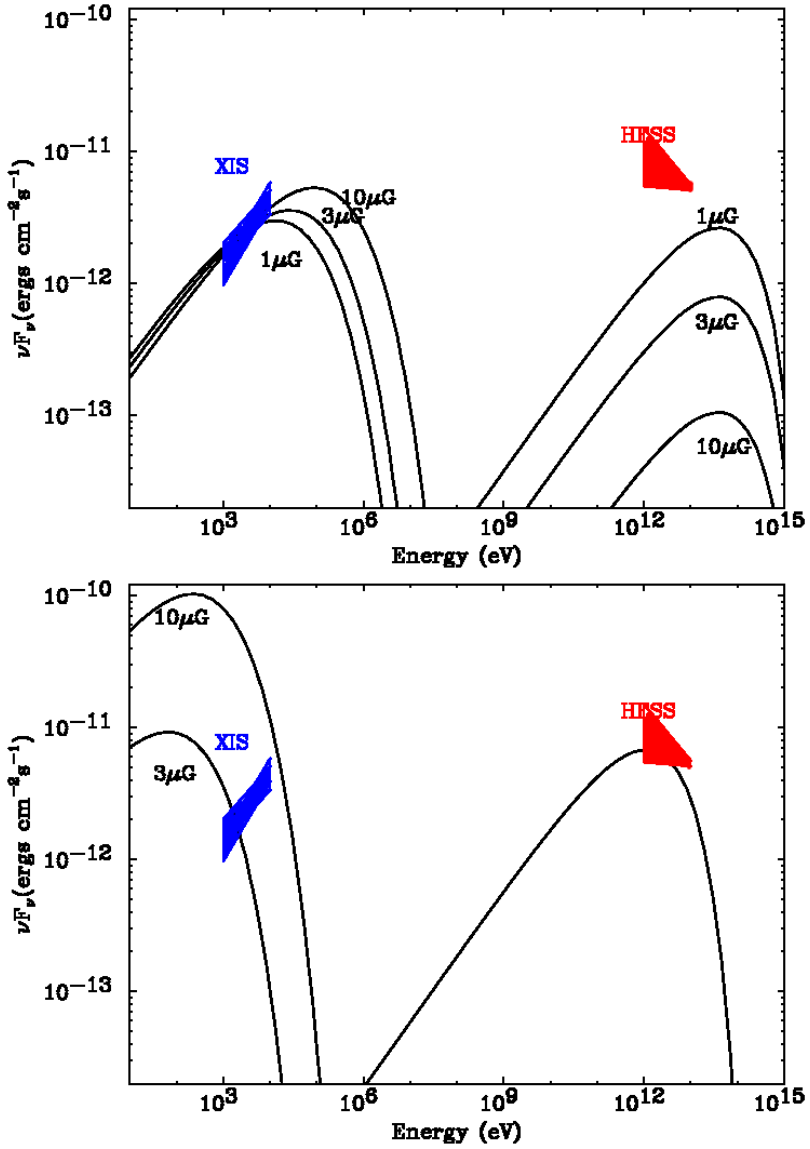

Figure A.2: Spectral energy distribution for the Suzaku and HESS (Renaud et al., 2008) measurements with synchrotron and inverse Compton models for HESS J1809–193. Electron number index is assumed to be $p = 2$. The normalization and the maximum energy of electrons are adjusted to reproduce the X-ray data (top) and the TeV data (bottom). Black lines show the different ambient magnetic fields.

Appendix B

Systematic Errors of the X-Ray Extension of the PWNe

We estimate the systematic errors in the determination of the extension of the PWNe in the X-ray band. Possible causes of the systematic errors are:

1. Point spread function of the Suzaku XRT

2. Intrinsic asymmetry of the X-ray morphology of the PWNe

We study these systematic errors in the following subsections separately.

B.1 Point Spread Function of the Suzaku XRT

In §4.1.3, we determined the extension of the PWN, AX J1838.0–0655, by fitting the 1-dimensional profile with a Gaussian function plus a constant model ignoring the central region ($1'$ radius) from the pulsar. However, since the Gaussian width of the source was comparable to the angular resolution of the Suzaku XRT ($\sim 1'$), we must take into account the effect of the point spread function of Suzaku XRT carefully.

First we simulated the XIS image for a point source using the XRT+XIS simulator `xissim`. The image is shown in figure B.1 (left). We created the profile assuming the same sky region where we calculated the surface brightness of the PWN. The profile is shown in figure B.1 (right). We fitted the profile with a double Gaussian function. The best-fit Gaussian widths were $\sigma_a = 0'.13$ for a narrow Gaussian and $\sigma_b = 0'.84$ for a broad one, and the normalization ratio was 0.70.

We fitted the 1-dimensional profile of the PWN with the model profile for the point-like pulsar, which is equivalent to the PSF model, and the model PWN, which is convolution of a Gaussian plus a constant and the PSF model. Figure B.2 (right) shows the fitted profile. The best-fit intrinsic Gaussian width after removing the

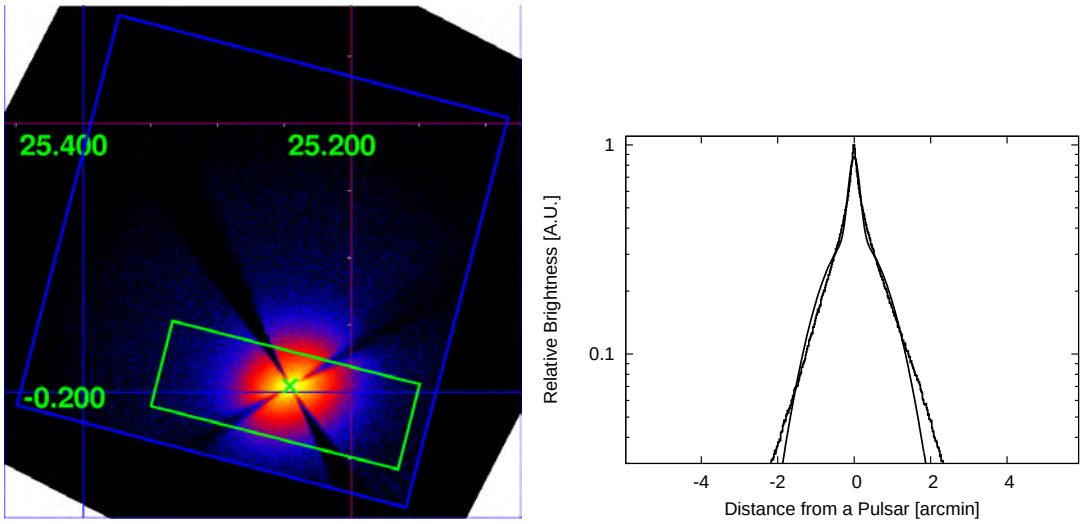

Figure B.1: Left: simulated XIS image of a point source located at the brightest position of AX J1838.0–0655. Right: 1-D profile with the fitted model of a double Gaussian.

broadening effect due to the PSF is $\sigma = 1'.7 \pm 0'.2$. This result is comparable to the width determined using the Chandra ACIS data in §4.1.3.

In §4.1.3, we determined the width of the PWN as $\sigma \sim 1'.2$. We suspect that the tail of the PSF due to the pulsar biased the best-fit extension to the smaller value. Because the PSF affects the estimation of the extension in a quadratic manner, the systematic error due to the point spread function of the Suzaku XRT is estimated as $\sqrt{1'.7^2 - 1'.2^2} \sim 1'.2$. This systematic error needs to be considered only for the positive sign.

B.2 Intrinsic asymmetry of the X-ray morphology of the PWNe

When we determined the size of the PWNe, we needed to define the position angle of the 1-dimensional profile. When we selected the position angle, we of course avoided local structures such as jets. However, intrinsic asymmetry of the X-ray morphology may affect the determination of the extension through the selection of the position angle. Here we estimate the systematic errors due to the selection of the position angle of the 1-D profile.

First we check the case of the PWN, AX J1838.0–0655. Avoiding the point-like source near the source, we created the surface brightness profile in the position angle shown in figure B.3 (left). We fitted the profile in the same way as the last subsection.

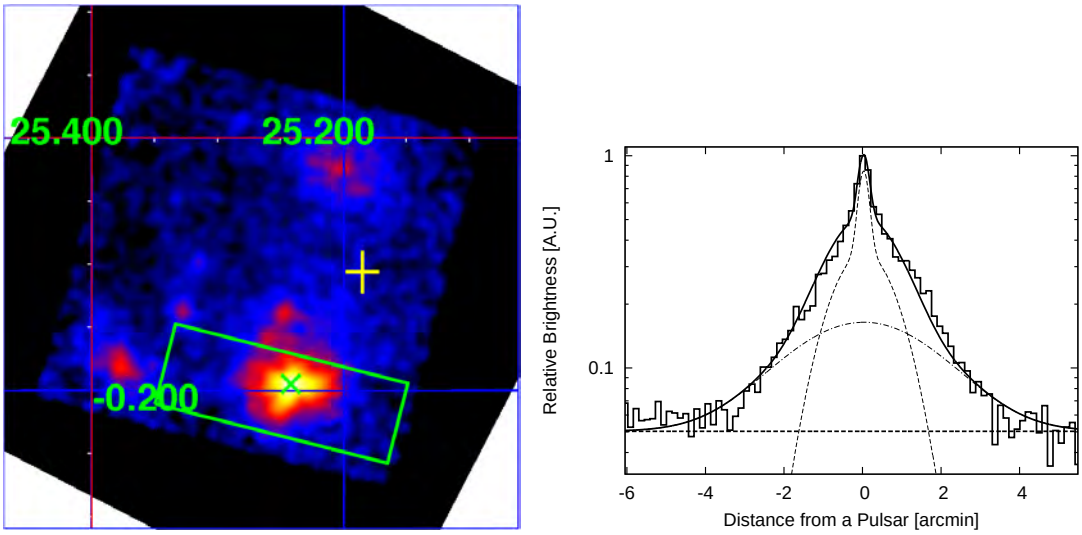

Figure B.2: Left: The same image as figure 4.4 (top). Right: normalized 1-dimensional profile of the surface brightness obtained from the enclosed region with a green box in the top panel with a spacial bin size of 8″.4. Solid curve shows the best-fit line of the total model. Dashed and dash-dot curve show the best-fit line of the pulsar and PWN component, respectively. Horizontal dashed line shows a constant.

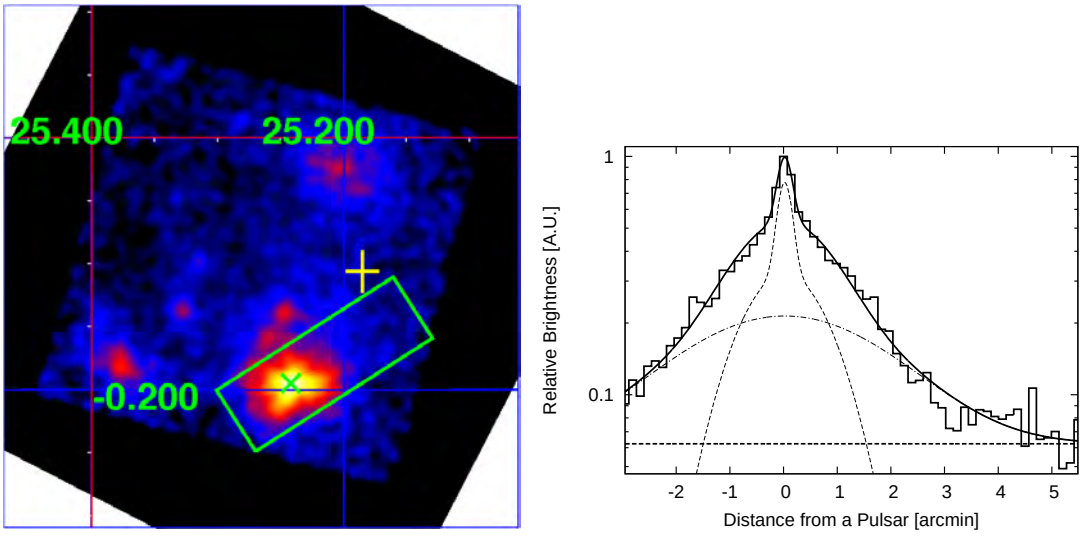

Figure B.3: Same as figure B.2 except for the direction of the green box from which we create a 1-D profile.

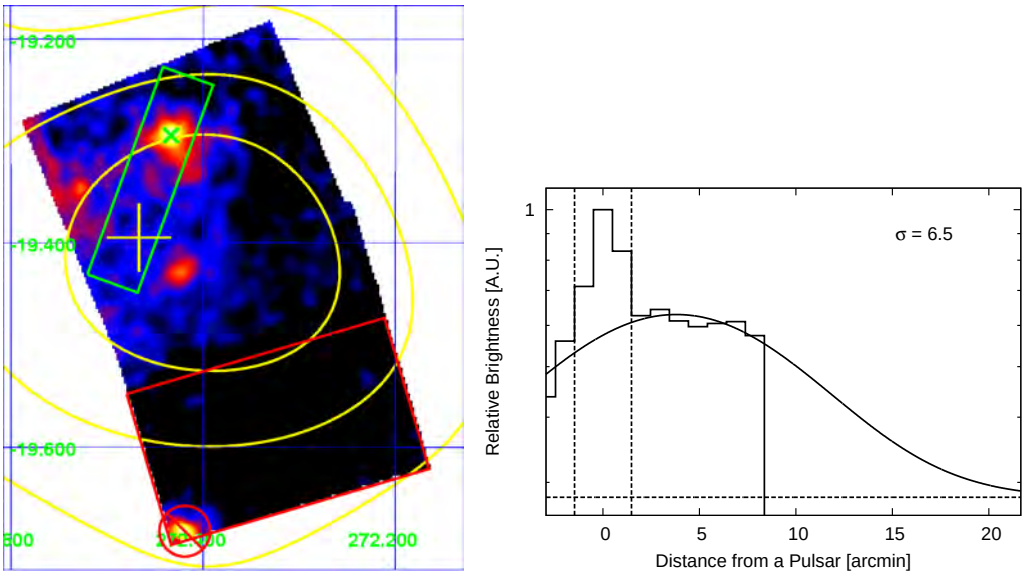

Figure B.4: Same as figure 4.11 except for the direction of the green box from which we create a 1-D profile.

Figure B.3 (right) shows the fitted profile. The best-fit intrinsic Gaussian width was $\sigma = 1'.7 \pm 0'.2$, which was statistically consistent to the extension determined for the other position angle in the last subsection.

When we determined the size of the PWN around the pulsar PSR J1809–1917, we selected the position angle which included the pulsar and the emission from GRXE. However, the non-thermal X-ray emission seems to be extended to the south-east direction. We created a 1-dimensional profile of the surface brightness using the data in the rectangle region shown in figure B.4 (left), which run from the pulsar position to south-east. The profile obtained is shown in figure B.4 (right). We fitted the profile with a Gaussian function plus a constant. We ignored the bright part of $2'.9$ wide including the pulsar in the fit rather than modeling the PSF shape for simplicity, because the extension of the X-ray emission is much larger than the width of the PSF of XRT. The constant was fixed to the GRXE level estimated in figure 4.11. The Gaussian center was found to be offset by $\sim 4'$ from the pulsar and the rms width to be $\sigma = 6'.5 \pm 0'.9$, which was statistically consistent to the extension determined for the other position angle in §4.2.3.

We also determined the typical systematic error in the extension of the X-ray PWN due to the selection of the position angle. For this purpose, we select Kes 75 because it has a simple structure, no contaminating source and largely different position angle can be tested. Here the error is determined as the 1-sigma scatter of the widths excluding the contribution of the statistical uncertainty. We created 1-D profiles along four different position angles avoiding the shell structure in the SE and

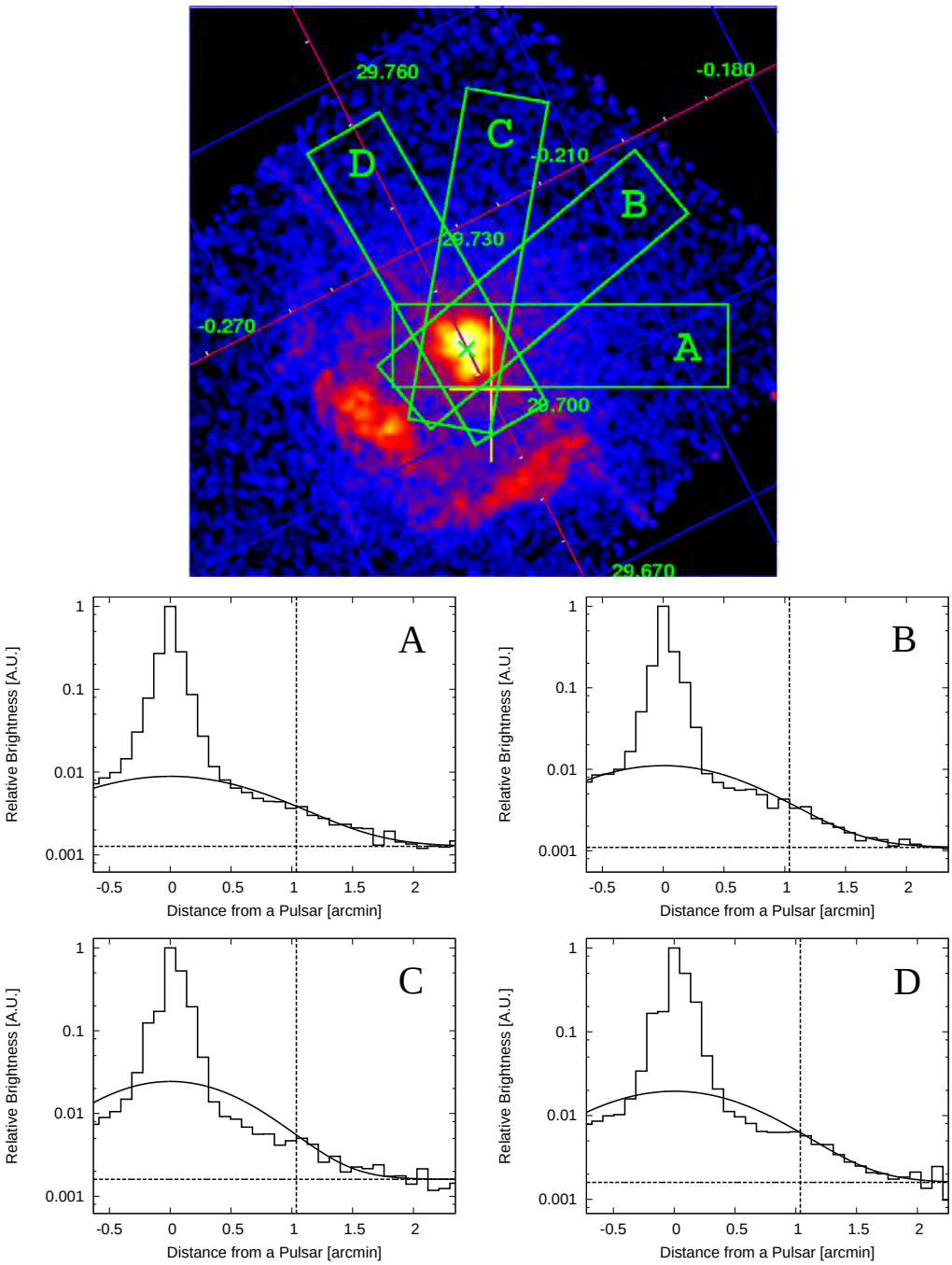

Figure B.5: Difference of the Gaussian width of the X-ray PWN due to the direction of the 1-D profile. Top: Chandra ACIS image around Kes 75 in the 2.0–7.0 keV band, which is the same image as figure 4.30. Bottom: A 1-D profiles (bin size of $5''.4$) of the surface brightness calculated from the data enclosed in the green rectangle in the top panel. Labels (A,B,C and D) in the top right corner of the figures represent from which region in the top panel the profile was obtained. Solid and dashed lines show the best-fit line of the Gaussian profile and a constant, respectively. The central core near the pulsar was ignored in the fit ($2'.1$ wide, inner part of the vertical dashed line).

Table B.1: Extension of the X-ray PWN of Kes 75 for the region labeled as A to D.

Region	Gaussian width
A	$0'.71 \pm 0'.07$
B	$0'.65 \pm 0'.05$
C	$0'.55 \pm 0'.07$
D	$0'.63 \pm 0'.07$

SW of the pulsar. The regions are labeled as "A", "B", "C" and "D" as indicated in figure B.5 (top). Figure B.5 (bottom) shows the 1-D profile created from each region. We fitted each profile with a Gaussian function plus a constant. We ignored bins near the pulsar for $\sim 2'$ wide in the fit with a Gaussian profile. The best-fit Gaussian widths are summarized in table B.1. The mean Gaussian width weighted by the fitting errors is $0'.64$ with an error of $0'.05$. This result means that the systematic error of the extension due to the selection of the position angle is $\sim 8\%$.

B.3 Summary

We estimated the systematic errors for the extension of the PWNe in the X-ray band due to the following two causes: a point spread function of the Suzaku XRT and a selection of the position angle of the 1-D profile. The systematic error due to the former is $1'.2$ for the positive sign and that due to the latter is 8% of the extension.

Taking these systematic errors into consideration, we re-created the plot of the correlation between the size of the X-ray PWN and the characteristic age of the associated pulsar. Figure B.6 shows the plot.

We fitted the plot with the models in both the diffusion and advection dominant scenario as we did in §5.3.2. The best-fit models are shown in figure B.7. In the diffusion dominant scenario, we obtained

$$\xi(t) = 1 + (0.9 \pm 0.6) \left(\frac{t}{1 \text{ kyr}} \right)^{(1.3 \pm 0.2)}, \tag{B.1}$$

and ξ would be ~ 300 when $\tau_c = 100$ kyr. On the other hand, in the advection dominant scenario, we obtained

$$\sigma(t) = (2.2 \pm 0.6) \times 10^{-3} \left(\frac{t}{1 \text{ kyr}} \right)^{(0.62 \pm 0.09)}. \tag{B.2}$$

The result indicates σ would be as large as ~ 0.04 when $\tau_c = 100$ kyr.

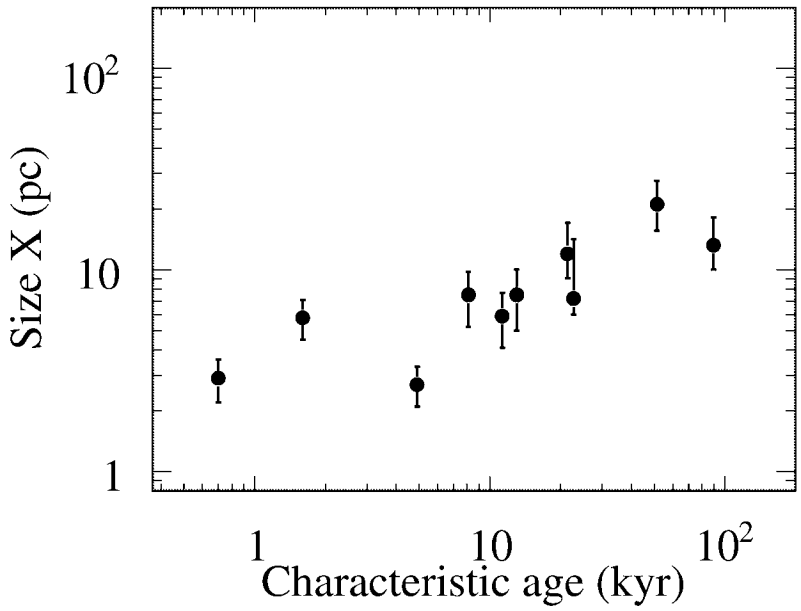

Figure B.6: Correlation between the size of the X-ray PWN and the characteristic age of the pulsar. Systematic errors due to the point spread function of Suzaku XRT and the direction of the 1-D profile are added to the plot shown in figure 5.10.

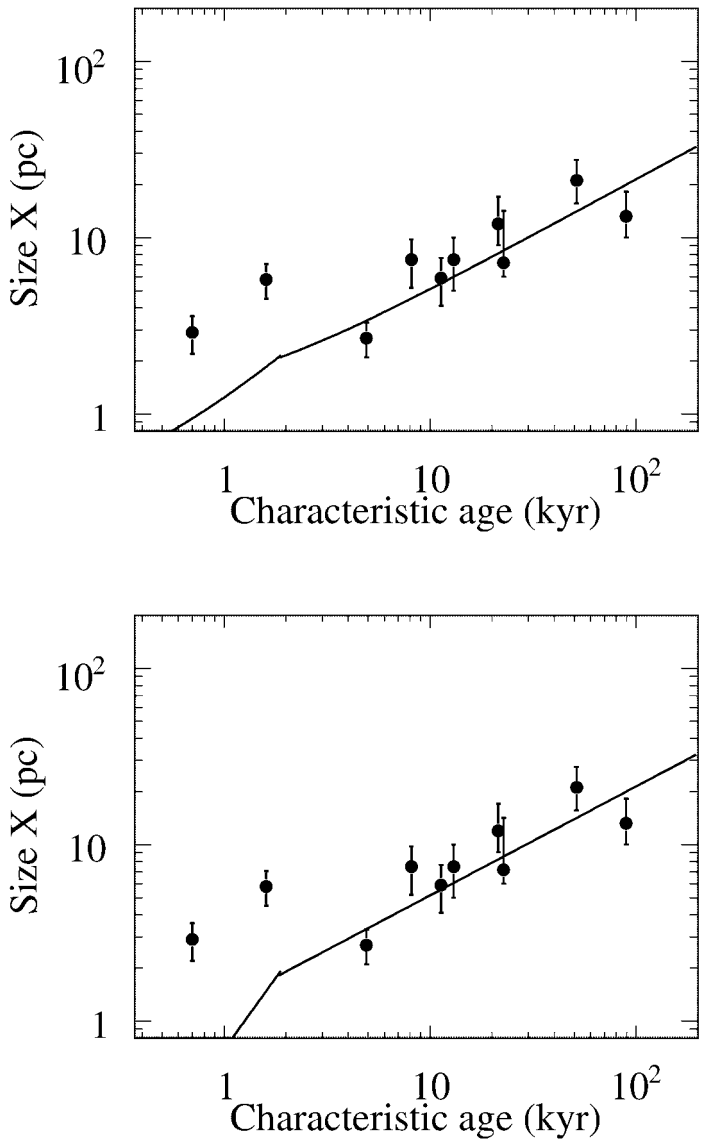

Figure B.7: The fitting results with the diffusion (top) and the advection (bottom) models. ξ and σ are assumed to be functions of time.

Bibliography

Aharonian, F. A., & Atoyan, A. M. 1998, Neutron Stars and Pulsars: Thirty Years after the Discovery, 439

Aharonian, F. A., et al. 2004, Nature, 432, 75

Aharonian, F., et al. 2005a, Science, 307, 1938

Aharonian, F., et al. 2005b, A&A, 432, L25

Aharonian, F., et al. 2005c, A&A, 435, L17

Aharonian, F., et al. 2005d, A&A, 439, 1013

Aharonian, F., et al. 2006a, ApJ, 636, 777

Aharonian, F., et al. 2006b, A&A, 448, L43

Aharonian, F., et al. 2006c, A&A, 456, 245

Aharonian, F., et al. 2006d, A&A, 457, 899

Aharonian, F., et al. 2006e, A&A, 460, 365

Aharonian, F., et al. 2007, A&A, 472, 489

Aharonian, F., et al. 2008a, A&A, 477, 353

Aharonian, F., et al. 2008b, A&A, 490, 685

Altenhoff, W. J., Downes, D., Goad, L., Maxwell, A., & Rinehart, R. 1970, A&AS, 1, 319

Anada, T., Ebisawa, K., Dotani, T., & Bamba, A. 2008, arXiv:0810.3745

Anders, E., & Ebihara, M. 1982, Geochim. Cosmochim. Acta, 46, 2363

Arons, J. 2004, Advances in Space Research, 33, 466

Atoyan, A. M., & Aharonian, F. A. 1996, MNRAS, 278, 525

Bamba, A., Ueno, M., Koyama, K., & Yamauchi, S. 2003a, ApJ, 589, 253

Bamba, A. PhD thesis, Kyoto University, 2003b

Bamba, A., et al. 2007, PASJ, 59, 209

Bell, A. R. 1978, MNRAS, 182, 147

Blanton, E. L., & Helfand, D. J. 1996, ApJ, 470, 961

Blondin, J. M., Chevalier, R. A., & Frierson, D. M. 2001, ApJ, 563, 806

Blandford, R., & Eichler, D. 1987, Phys. Rep., 154, 1

Blumenthal, G. R., & Gould, R. J. 1970, Reviews of Modern Physics, 42, 237

Brisken, W. F., Carrillo-Barragán, M., Kurtz, S., & Finley, J. P. 2006, ApJ, 652, 554

Bocchino, F., van der Swaluw, E., Chevalier, R., & Bandiera, R. 2005, A&A, 442, 539

Burke, B. E., Mountain, R. W., Daniels, P. J., Cooper, M. J., & Dolat, V. S. 1994, IEEE Transactions on Nuclear Science, 41, 375

Büsching, I., de Jager, O. C., & Snyman, J. 2007, ApJ, 656, 841

Camilo, F., Ransom, S. M., Gaensler, B. M., Slane, P. O., Lorimer, D. R., Reynolds, J., Manchester, R. N., & Murray, S. S. 2006, ApJ, 637, 456

Carrigan, S., Hinton, J. A., Hofmann, W., Kosack, K., Lohse, T., Reimer, O., & for the H. E. S. S. Collaboration 2007, arXiv:0709.4094

Cordes, J. M., & Lazio, T. J. W. 2002, arXiv:astro-ph/0207156

D'Amico, N., et al. 2001, ApJL, 552, L45

Davies, B., Figer, D. F., Law, C. J., Kudritzki, R.-P., Najarro, F., Herrero, A., & MacKenty, J. W. 2008, ApJ, 676, 1016

DeLaney, T., Gaensler, B. M., Arons, J., & Pivovaroff, M. J. 2006, ApJ, 640, 929

Dickey, J. M., & Lockman, F. J. 1990, ARA&A, 28, 215

Dodson, R., Legge, D., Reynolds, J. E., & McCulloch, P. M. 2003, ApJ, 596, 1137

Ebisawa, K., et al. 2008, PASJ, 60, 223

Figer, D. F., MacKenty, J. W., Robberto, M., Smith, K., Najarro, F., Kudritzki, R. P., & Herrero, A. 2006, ApJ, 643, 1166

Fukazawa, Y., et al. submitted to PASJ, 2009

Gaensler, B. M., Pivovaroff, M. J., & Garmire, G. P. 2001, ApJL, 556, L107

Gaensler, B. M., Arons, J., Kaspi, V. M., Pivovaroff, M. J., Kawai, N., & Tamura, K. 2002, ApJ, 569, 878

Gaensler, B. M., Schulz, N. S., Kaspi, V. M., Pivovaroff, M. J., & Becker, W. E. 2003, ApJ, 588, 441

Gallant, Y. A., et al. 2008, 40 Years of Pulsars: Millisecond Pulsars, Magnetars and More, 983, 195

Goldreich, P., & Julian, W. H. 1969, ApJ, 157, 869

Gotthelf, E. V., Vasisht, G., Boylan-Kolchin, M., & Torii, K. 2000, ApJL, 542, L37

Gotthelf, E. V., & Halpern, J. P. 2008, ApJ, 681, 515

Gupta, Y., Mitra, D., Green, D. A., & Acharyya, A. 2005, Current Science, 89, 853

Harnden, F. R., Jr., Grant, P. D., Seward, F. D., & Kahn, S. M. 1985, ApJ, 299, 828

Helfand, D. J., & Becker, R. H. 1987, ApJ, 314, 203

Helfand, D. J., Gotthelf, E. V., & Halpern, J. P. 2001, ApJ, 556, 380

Helfand, D. J., Collins, B. F., & Gotthelf, E. V. 2003, ApJ, 582, 783

Hess, V. F. 1912, Phys. Zeits., 13, 1084

H. E. S. S. Collaboration: A. Djannati-Atai, De Jager, O. C., Terrier, R., Gallant, Y. A., & Hoppe, S. 2007, arXiv:0710.2247

Hester, J. J. 2008, ARA&A, 46, 127

Hinton, J. A., Funk, S., Carrigan, S., Gallant, Y. A., de Jager, O. C., Kosack, K., Lemière, A., Pühlhofer, G. 2007a, A&A, 476, L25

Hinton, J. 2007b, ArXiv e-prints, 712, arXiv:0712.3352

Ishisaki, Y., et al. 2007, PASJ, 59, 113

Jokipii, J. R. 1987, ApJ, 313, 842

Kargaltsev, O., Pavlov, G. G., & Garmire, G. P. 2007, ApJ, 660, 1413

Kargaltsev, O., & Pavlov, G. G. 2007, ApJ, 670, 655

Kargaltsev, O., & Pavlov, G. G. 2008a, 40 Years of Pulsars: Millisecond Pulsars, Magnetars and More, 983, 171

Kargaltsev, O., Pavlov, G. G., & Wong, J. A. 2008b, arXiv:0805.1041

Kaspi, V. M., Crawford, F., Manchester, R. N., Lyne, A. G., Camilo, F., D'Amico, N., & Gaensler, B. M. 1998, ApJL, 503, L161

Kataoka, J. PhD thesis, University of Tokyo, 2000

Kennel, C. F., & Coroniti, F. V. 1984, ApJ, 283, 694

Kirsch, M. G., et al. 2005, Proc. SPIE, 5898, 22

Kokubun, M., et al. 2007, PASJ, 59, 53

Komin, N., Carrigan, S., Djannati-Ataï, A., Gallant, Y. A., Kosack, K., Puehlhofer, G., Schwemmer, S., & for the H. E. S. S. Collaboration 2007, arXiv:0709.2432

Koyama, K., Petre, R., Gotthelf, E. V., Hwang, U., Matsuura, M., Ozaki, M., & Holt, S. S. 1995, Nature, 378, 255

Koyama, K., et al. 2007, PASJ, 59, 23

Landi, R., de Rosa, A., Dean, A. J., Bassani, L., Ubertini, P., & Bird, A. J. 2007, MNRAS, 380, 926

Larsson, S. 1996, A&AS, 117, 197

Lyne, A. G., & Lorimer, D. R. 1994, Nature, 369, 127

Malizia, A., et al. 2005, ApJL, 630, L157

Manchester, R. N., Hobbs, G. B., Teoh, A., & Hobbs, M. 2005, AJ, 129, 1993

Manzali, A., De Luca, A., & Caraveo, P. A. 2007, ApJ, 669, 570

Matsumoto, H., et al. 2007, PASJ, 59, 199

Mattana, F., et al. 2008, arXiv:0811.0327

Markwardt, C. B., & Ogelman, H. 1995, Nature, 375, 40

Marsden, P. L., Gillett, F. C., Jennings, R. E., Emerson, J. P., de Jong, T., & Olnon, F. M. 1984, ApJL, 278, L29

Matheson, H., & Safi-Harb, S. 2005, Advances in Space Research, 35, 1099

Mewe, R., Gronenschild, E. H. B. M., & van den Oord, G. H. J. 1985, A&AS, 62, 197

Mitsuda, K., et al. 2007, PASJ, 59, 1

Morris, D. J., et al. 2002, MNRAS, 335, 275

Nakajima, H., et al. 2008, PASJ, 60, 1

Ng, C.-Y., Roberts, M. S. E., & Romani, R. W. 2005, ApJ, 627, 904

Oegelman, H., & Zimmermann, H.-U. 1989, A&A, 214, 179

Ohashi, T., et al. 1996, PASJ, 48, 157

Pavlov, G. G., Kargaltsev, O. Y., Sanwal, D., & Garmire, G. P. 2001, ApJL, 554, L189

Pavlov, G. G., Kargaltsev, O., & Brisken, W. F. 2008, ApJ, 675, 683

Porquet, D., Decourchelle, A., & Warwick, R. S. 2003, A&A, 401, 197

Renaud, M., Hoppe, S., Komin, N., Moulin, E., Marandon, V., Clapson, A. -., & for the H. E. S. S. Collaboration 2008, arXiv:0811.1559

Rishbeth, H. 1958, Australian Journal of Physics, 11, 550

Roberts, M. S. E., Romani, R. W., Johnston, S., & Green, A. J. 1999, ApJ, 515, 712

Rybicki, G. B., & Lightman, A. P. 1979, New York, Wiley-Interscience, 1979. 393 p.,

Serlemitsos, P. J., et al. 1995, PASJ, 47, 105

Serlemitsos, P. J., et al. 2007, PASJ, 59, 9

Shibata, S., Tomatsuri, H., Shimanuki, M., Saito, K., & Mori, K. 2003, MNRAS, 346, 841

Slane, P., Chen, Y., Schulz, N. S., Seward, F. D., Hughes, J. P., & Gaensler, B. M. 2000, ApJL, 533, L29

Sokolsky, P. 1989, Frontiers in Physics, 76,

Tanaka, Y., Inoue, H., & Holt, S. S. 1994, PASJ, 46, L37

Takahashi, T., et al. 2007, PASJ, 59, 35

Tamura, K., Kawai, N., Yoshida, A., & Brinkmann, W. 1996, PASJ, 48, L33

Tawa, N., et al. 2008, PASJ, 60, 11

Terada, Y., et al. 2008, PASJ, 60, 25

Torii, K., et al. 1998, ApJL, 494, L207

Trimble, V. 1973, PASP, 85, 579

Trussoni, E., Massaglia, S., Caucino, S., Brinkmann, W., & Aschenbach, B. 1996, A&A, 306, 581

Uchiyama, Y., et al. 2008a, PASJ, 60, 35

Uchiyama, H., Matsumoto, H., Tsuru, T. G., Koyama, K., & Bamba, A. 2008b, arXiv:0808.3436

Weekes, T. C., et al. 1989, ApJ, 342, 379

Acknowledgements

I express my most greatful appreciation to Professor Tadayasu Dotani in ISAS, who lead me through my graduate course. I have learned an attitude toward study and had a fruitful five years at ISAS. I could not have finished my thesis without his great assist and encouragement.

I greatfully appreciate to Dr. Aya Bamba in ISAS for giving me a first motivation to the study of the pulsar wind nebulae. She gave me a lot of advices and comments and taught me the way to analyze the data. I was relieved by her encouragement many times. I express my thanks to Professor Ken Ebisawa in ISAS for providing the Suzaku data of HESS J1837–069 and guiding me to the study the pulsar wind nebulae. I am deeply grateful to Dr. Koji Mori in the University of Miyazaki for a hot discussion on the pulsar wind nebulae. ASCA GIS image of Vela X is courtesy of him. My gratitude is also for Dr. Ryo Yamazaki in Hiroshima University for discussing the interpretation on the extension of the X-ray emission from pulsar wind nebulae from a theoretical viewpoint. I thank to Mr. Hideki Uchiyama in Kyoto University for providing the Suzaku XIS images of HESS J1825–137. I also express gratitude to Professor Stefan Funk for a beneficial comment on the size of the HESS sources.

I owe a great deal to Dr. Masanobu Ozaki in ISAS, who taught me techniques for both experiment and programming. The way of thinking learned from him often assisted for the progress of this work. I also appreciate to Dr. Hiroshi Murakami in Rikkyo University for teaching me how to analyze the Suzaku data from the basics. And I wish to thank to all the members of X-ray astrophysical group in ISAS. I had a wonderful time as a graduate student with them for five years in ISAS.

Finally, I would like to thank Professor Noriko Yamasaki for providing an oppotunity to study X-ray astrophysics at ISAS in the University of Tokyo. I do hope that an X-ray astrophysics continue great success in the future.